UNIVERSITY OF SOUTHAMPTON

UV Written Blazed Chirped Bragg Grating Spectrometers

by

James W. Field

A thesis submitted in partial fulfillment for the degree of Doctor of Philosophy

in the
Faculty of Engineering and Physical Sciences
Optoelectronics Research Centre

02/06/21

UNIVERSITY OF SOUTHAMPTON

ABSTRACT

FACULTY OF ENGINEERING AND PHYSICAL SCIENCES
OPTOELECTRONICS RESEARCH CENTRE

Doctor of Philosophy

by James W. Field

Monolithic integrated spectrometers are ideal for use in portable testing equipment, however current research tends to focus on high-resolution platforms at near-infrared wavelengths. This thesis investigates a dispersive spectrometer platform based on blazed chirped Bragg gratings which has high resolution, large bandwidth, and low cost. As such it is suitable for portable Raman spectroscopy and optical coherence tomography.

Blazed chirped Bragg gratings diffract and focus light, with the angle of diffraction dependent on the wavelength of the input light. As such, the detected intensity distribution along a detector array can be used to measure the light spectrum. This thesis shows flexible fabrication and characterisation of these devices using small-spot direct UV writing, as well as methods of efficiently modelling their output intensity distribution.

Focussing aberrations of blazed chirped Bragg gratings are investigated and an ideal chirp function is derived to eliminate such aberrations. This is experimentally verified, enabling a device which operates over the 1440 nm to 1640 nm wavelength range. The device exhibited a peak resolution of 1.8 nm at 1560 nm and a typical resolution of 2.6 nm across a 100 nm range.

Scalar diffraction modelling was used to investigate the bandwidth of devices, showing 3 dB bandwidths of greater than 210 nm for devices operating at 1550 nm using a novel 45° detector mounting scheme. This mounting scheme also flattens the resolution response with wavelength, resulting in greater spectral resolution further from the design wavelength.

Finally a blazed chirped Bragg grating with variable blaze angle was demonstrated to offset fabrication effects and further increase device resolution and sensitivity. To our knowledge this is the first example of Bragg gratings with varying blaze angle along their length. Devices operating at wavelengths close to 780 nm achieved measured resolutions of 0.4 nm to 0.5 nm, though it is suspected that this is limited by aberrations inside the characterisation system. Modelling shows that fully optimised devices operating at 780 nm should achieve resolutions of 0.3 nm, as well as bandwidths exceeding 100 nm.

Declaration of Authorship

I, James W. Field, declare that this thesis, 'UV Written Blazed Chirped Bragg Grating Spectrometers' and the work presented in it is my own and has been generated by me as the result of my own original research.

I confirm that:

- This work was done wholly or mainly while in candidature for a research degree at this University
- Where any part of this thesis has previously been submitted for a degree or any other qualification at this University or any other institution, this has been clearly stated
- Where I have consulted the published work of others, this is always clearly attributed
- Where I have quoted from the work of others, the source is always given. With the exception of such quotations, this thesis is entirely my own work;
- I have acknowledged all main sources of help. Where the thesis is based on work done by myself jointly with others, I have made clear exactly what was done by others and what I have contributed myself
- Parts of this work have been published, a publication list is provided in appendix C

Signed:

Date: 02/06/21

Acknowledgements

While this thesis has my name on the front, I owe many thanks to a large number of people.

To Peter Smith and Corin Gawith, for providing support when I needed it. To James Gates for helping me convert my ideas into coherent research (and for endlessly re-reading this thesis). To Rex Bannerman, Alan Gray, Devin Smith and Matthew Posner for providing friendship and scientific support (and listening to me moan (a lot)). To Paula Smith for always making my life easier. To group members past and present: Teresa Ferreiro, Sling Lynch, Miranda Turvey, Chloe Watson, Chris Holmes, Paolo Mennea, Paul Gow, Alex Jantzen, Senta Jantzen, Charlie Turner, Salman Ahmed, Delta Hung and Jack Pangbourne. I've thoroughly enjoyed working alongside you, learning from you and getting to know you all. To Lewis and Sam, for nurturing a wide eyed PhD student into your lab and being fantastic friends.

To the D&D/Warhammer group, Alex Dent, Mark Stanton, Andy Knighton and Simon Thomas for providing distractions when I needed it.

To Gemma, Steve, Andy and Jane for cheering me on and keeping me smiling.

To Katie, for keeping me sane. I never would have managed this without you and I'm lucky to have you in my life.

To my Mum and Dad for always being there. For all the love and support you've given me over the years, and for getting me interested in science in the first place (and for putting up with me when I was too interested!) This work is as much your achievement as it is mine.

Contents

List of acronyms

AWG arrayed waveguide grating

CAD computer aided design

CCD charge-coupled device

CMOS complimentary metal-oxide semiconductor

ECDL external-cavity diode laser

EOM electro-optic modulator

FDM finite-difference method

FDTD finite-difference time domain

FEM finite-element method

FHD flame hydrolysis deposition

FSR free spectral range

FWHM full-width half maximum

NA numerical aperture

NIR near infrared

OSA optical spectrum analyser

OCT optical coherence tomography

PM polarisation maintaining

PSO position-synchronised output

SLED super-luminescent diode

SOI silicon-on-insulator

SM single mode

ssDUW small-spot direct UV writing

SNR signal-to-noise ratio

SWAP size, weight and power

TE transverse electric

THOX thermal oxide

TM transverse magnetic

A note on naming conventions

Within the Bragg grating community there is no clear consensus of a naming convention for Bragg gratings with grating planes non-normal to the direction of propagation, with both 'blazed' and 'tilted' used. This thesis uses 'blazed' in all instances to highlight the physics of blazed diffraction gratings when considering Bragg gratings.

For something to exist, it has to be observed.

For something to exist, it has to have a position in time and space.

And this explains why nine-tenths of the mass of the universe is unaccounted for.

Nine-tenths of the universe is the knowledge of the position and direction of everything in the other tenth. Every atom has its biography, every star its file, every chemical change its equivalent of the inspector with a clipboard. It is unaccounted for because it is doing the accounting for the rest of it, and you cannot see the back of your own head.

Nine-tenths of the universe, in fact, is the paperwork.

–*Thief of Time, Terry Pratchett*

Chapter 1

Introduction

Science fiction commonly makes use of a 'multi-analyser': a single portable device which can characterise any substance, diagnose medical conditions and so on. Though such a device is unlikely to be realised in the near future, it would be of extreme commercial interest. As such there is a drive to make characterisation equipment more portable, and to try and add more functionality to existing characterisation equipment. With the continued development of integrated photonics there now exist platforms which can miniaturise many existing lab-based characterisation systems, such that a smartphone sized package may contain multiple different tools. The basis of many of these integrated photonics characterisation systems are integrated spectrometers.

Though much academic work has been undertaken to integrate spectrometers the commercial market still largely relies on bulk grating spectrometers. An integrated solution is likely to be cheaper to mass produce and integrate with other integrated technology to produce portable characterisation systems with a fraction of the size, weight and power (SWAP) requirements of their bulk counterparts.

This chapter introduces integrated spectrometers, starting with an overview of the current state of the art, including a discussion of the common features important in integrated spectrometers. A discussion of potential applications where integrated spectrometers could prove disruptive follows, focusing on Raman spectroscopy, OCT and hyperspectral imaging. A specification for a spectrometer to be of use for each of those applications is developed with reference to literature. The proposed blazed chirped Bragg grating scheme (which forms the basis for this thesis) is then discussed. Finally the structure of the rest of this thesis is summarised.

1.1 State of the art

To understand the current state of the art and the potential advantages and drawbacks of different spectrometer schemes a literature review was undertaken, the results of which are summarised in table 1.1 and discussed in the following section. The performance of integrated spectrometers can be compared using a number of characteristics, in this case these will be resolution, bandwidth, wavelength range, material and size. This section summarises how these are used in each case to ensure clarity.

The wavelength range, resolution and bandwidth are the most important parameters for a device; the wavelength range in particular dictates suitable applications for a spectrometer. Wherever possible the bandwidth will be discussed in terms of the full-width half maximum (FWHM), the wavelength range within which the signal from the device is within 3 dB of the peak signal ($\Delta\lambda_{\mathrm{FWHM}}$). This response takes the optical element and the detector into account. Some devices are free spectral range (FSR) limited; the response at one wavelength is indistinguishable from a higher-order response at a different wavelength. The term 'operation bandwidth' is used to describe the whole wavelength range over which the device operates.

Unless otherwise stated the spectral resolution refers to the two-peak resolution according to the Houston criteria [1]. Two spectral peaks are resolved provided the measured separation of the peaks on a detector is at least the FWHM of either of the peaks. This shall be referred to as the 'classical resolution'. Note that it has been shown that multiple peaks can be resolved beyond this limit [2], however a true general limit of resolution is difficult to define. In addition it has been shown that better classical resolution typically results in better actual resolution, with noise being the limiting factor on any potential enhancement [3].

The material used to fabricate devices typically dictates the operational wavelength range (through the transparency window of the material) and potential routes to fabrication. An etched device in silicon can potentially be mass produced using cleanroom processing, however it will typically suffer from high coupling loss to free space and optical fibre. A silica platform has better coupling to free space and is transparent in the visible band, however cleanroom fabrication techniques often struggle with the layer thicknesses required to make devices in silica; the end product is likely to be more expensive.

This thesis is restricted to passive devices, more specifically devices which record spectra instantaneously with no feedback or control mechanisms. Active control schemes add another degree of freedom by altering the characteristics of the device over time. Passive devices operate faster than active ones, and reduce the need for control electronics resulting in a lower SWAP requirement.

Source	Material	Scheme	Resolution	Bandwidth	Centre wavelength
[4]	SOI	Fourier	40 pm	0.75 nm	1550 nm
[5]	Optical fibre	Fourier	0.2 − 3 nm	76 nm	1547 nm
[6]	SOI	AWG	0.15 nm	5.6 nm	1545 nm
[7]	SiON	AWG	0.16 nm	20 nm	800 nm
[7]	SiON	AWG	0.4 nm	78 nm	1300 nm
[8]	SiON	AWG	0.2 nm	22 nm	901 nm
[9]	SiO_2	AWG	40 pm	160 nm	1540 nm
[10]	SiON	Echelle	0.49 nm	24 nm	850 nm
[11]	SiN	Hologram	0.15 nm	64,64 nm	662,798 nm
[12]	SiO_2	Hologram	15 pm	0.96 nm	660 nm
[13]	SOI	Optimisation	0.75 nm	25 nm	1513 nm
[14]	Optical fibre	Optimisation	1 nm	350 nm	575 nm
[15]	Optical fibre	Waveguide	0.12 nm	14 nm	1554 nm
[16]	SiO_2	Waveguide	0.15 nm	7.8 nm	1563 nm
[17]	SOI	Waveguide	15 nm	180 nm	1500 nm

TABLE 1.1: Summary of state-of-the-art integrated devices

1.1.1 Fourier transform schemes

Integrated Fourier transform spectrometers boast very high resolutions; Velasco et al. reported resolutions of 40 pm at a wavelength of 1550 nm using an array of 32 Mach-Zehnder interferometers and delay lines in a single chip [4]. The device operated over a relatively narrow free spectral range of 0.75 nm, limited by the number of interferometers. Increasing the operation bandwidth without worsening the resolution requires adding more interferometers with finer delay line distance increments. Fabrication tolerances on delay line length prevent bandwidth increasing past 10 nm. The authors also propose such a scheme could exhibit a potential throughput (étendue) advantage [4]. A multicore optical fibre could be used to deliver light into the device, with a single interferometer waveguide connected to each core. Though theoretically sound, such a scheme is unlikely to see a practical implementation due to the complexity of the multicore fibre to waveguide coupling.

An alternative scheme has been proposed by Wielandy and Dunn [5] using a superstructured blazed Bragg grating in an optical fibre (an introduction into the theory of blazed Bragg gratings can be found in section 4.1.1). A pair of blazed Bragg gratings with different periods were fabricated on top of each other. Light diffracted from the fibre exhibits an interference pattern dependent on the wavelength of the light and the period offset between the two gratings. Light input into the fibre results in a spatial interferogram which can be measured by placing a detector array (eg. a charge-coupled device (CCD)) near the fibre; the input spectrum can be recovered by Fourier transforming the spatial intensity distribution. Limited characterisation is shown in the above publication, however the device operates over a 1509 nm to 1585 nm wavelength range

and should theoretically achieve a resolution below 3 nm over the whole wavelength range, with resolution at the top of the wavelength range approaching the 0.2 nm level. Such a device exhibits a much wider bandwidth, however the highly variable resolution will likely limit the usefulness over much of that bandwidth.

1.1.2 Arrayed waveguide grating (AWG)

Arrayed waveguide gratings (AWG) split light into many different propagation paths of different lengths and recombine them into a distributed wavefront. The phase of the wavefront is engineered by the length variation across the waveguide array. A central wavelength is designed such that the phase from different waveguides is offset by multiples of 2π. Deviations from that central wavelength incur a linear phase delay across the reconstructed phasefront resulting in angular dispersion. Light of different wavelengths is captured in different output waveguides; for spectrometer operation output waveguides are connected to a detector array. Such devices have been shown in silicon-on-insulator (SOI) [6] and SiON [7], [8] platforms, with a resolution of 0.16 nm and a 20 nm FSR at a wavelength of 800 nm. The resolution is attractive, however increased FSR requires additional waveguides; AWGs with large numbers of waveguides are susceptible to phase errors due to fabrication tolerances. A potential solution to this was proposed by Takada et al. using a silica platform [9]. After fabrication and characterisation of waveguide arrays a UV laser was used to correct phase errors. This approach enabled a multiplexed AWG device operating between 1460 nm and 1620 nm, with a channel spacing of 40 pm. Though extremely impressive, such a device is impractical to fabricate and expensive; the UV phase compensation process is complex and time consuming, and the device spanned an entire 4 inch wafer.

1.1.3 Integrated echelle gratings

In an integrated analogue of bulk spectrometers Ma et al. [10] showed a curved echelle grating spectrometer in a SiON platform which achieved a resolution of 0.49 nm at a wavelength of 850 nm. A channel waveguide sends light into a planar waveguiding layer, where it is free to diffract in-plane. The light propagates onto a curved echelle grating which provides angular dispersion and focusing. Light is focused onto an array of output waveguides which contain integrated detectors. The operation bandwidth of the device is limited by the FSR of the echelle, which is 24 nm. Contrary to previously discussed Fourier transform and AWG schemes, echelle grating spectrometers are not dependent on waveguide uniformity. This means complimentary metal-oxide semiconductor (CMOS) fabrication techniques can be used to mass-produce devices at low-cost.

1.1.4 Planar holograms

More general diffractive structures can be used as an alternative to historically proven echelle gratings. Calafiore et al. [11] demonstrated a planar hologram scheme in SiN. Similar to the echelle scheme a channel waveguide is used to diffract light into a planar layer where it is incident on a pair of 2D planar holograms optimised using computational design [12], [18]. A single device demonstrates 0.15 nm resolution across two wavelength bands: 630 nm to 694 nm and 766 nm to 850 nm. By changing the hologram design, operation over a wide continuous wavelength band at high resolution is possible. Poor coupling efficiency to optical fibre (20 %) resulted in considerable stray light inside the device, which would be an issue for applications with weak signals.

1.1.5 Optimisation-based schemes

Redding et al.[13], [14], [19] have shown a number of spectrometers using complex interference. Rather than using any a priori assumptions about the device characteristics the schemes used optimisation techniques to reconstruct the input spectrum based on results from training with various input spectra. Spectrometer operation has been shown for wavelengths between 400 nm and 750 nm with a resolution of 1 nm by imaging the speckle pattern distribution in 4 cm length of optical fibre. Due to the nonlinearity of the system, the reconstruction is extremely sensitive to environmental conditions and poorly suited for portable use. It is possible that environmental monitoring alongside the calibration procedure could suppress such effects.

1.1.6 Waveguide grating schemes

In many of the integrated schemes shown above channel waveguides inject light into a planar waveguide where it is incident on a diffractive structure. Instead of using the waveguide as a delivery system it is possible to embed the diffractive structure along the waveguide. Meltz et al. [20] first demonstrated such a device; UV laser-written blazed Bragg gratings in silica were used to tap light out of the core of the fibre [20]. It was later shown that by chirping the period of the grating the output from the fibre could be focused [21]. Wagner et al [15], [16], [22] then highlighted that such a structure produced angular dispersion, different wavelengths travelling along the fibre focused to different positions outside the fibre. By placing a linear CCD array at the focal plane of the fibre output the spatial intensity distribution along the detector could be mapped to the input spectrum along the fibre. Later refinement in a silica chip achieved a resolution of 0.15 nm with a 7.8 nm bandwidth at 1550 nm [16]. The phase mask fabrication method used to create these devices resulted in a very small period chirp 4 nm/mm, which resulted in a focal length much longer than the device. As a consequence the detctor had to be mounted in free space well outside the chip.

Bock et al. demonstrated an alternative approach by etching 'teeth' angled at 45° into a curved waveguide in a silicon platform. This device had a broad bandwidth, with less than 3 dB variation in peak device output over the wavelength range 1340 nm to 1620 nm in a package with a 100 µm × 160 µm footprint. While the device is presented as a wavelength division multiplexer with a 15 nm channel spacing the authors suggest that a larger device would reduce the channel spacing (and increase the resolution).

1.2 Applications

The required specifications of a spectrometer will depend on its intended application. Three specific applications which would benefit from integrated spectrometers have been identified: Raman spectroscopy, OCT and hyperspectral imaging. Details of these technologies and the requirements of a spectrometer for these applications are given in the following sections and are used to derive a set of targets for a spectrometer to be applicable to such applications.

1.2.1 Raman spectroscopy

Raman spectroscopy probes the vibrational energy levels of a material using photon-phonon coupling. A probe beam at a frequency ν_0 is shifted to frequencies $\nu_+ = \nu_0 + \nu_M$ and $\nu_- = \nu_0 - \nu_M$, where ν_M is the frequency corresponding to the energy difference between the two molecular vibrational energy levels [23]. ν_+ and ν_- are referred to as anti-Stokes and Stokes processes respectively. At 300 K there is little population in the upper vibrational level, so anti-Stokes Raman shifts are heavily suppressed.

Raman spectroscopy is particularly useful in interrogating the 'fingerprint region' of vibrational frequencies between 800 cm^{-1} and 1800 cm^{-1} , which is commonly used to identify organic and biological compounds. Direct measurement of these transitions requires detection in 5.5 µm to 12.5 µm region, where sources and detectors are expensive. Raman spectroscopy measures a frequency offset, so these signals can be measured in the visible region using conventional sources and detectors.

Fluorescence and Rayleigh scattering both result in strong signals which can obscure Raman scattering. Rayleigh scattering results in a signal following the spectrum of the pump beam, whereas fluorescence results in a significantly broader response [24]. Fluorescence can be eliminated by using an infra-red pump beam with less photon energy than the shortest expected electronic transition. Raman and Rayleigh scattering still both occur with virtual intermediate states due to their fast time-scales. Rayleigh scattering is typically removed using a high-pass filter. Even after filtering, Raman signals are likely to be weak. Photon-phonon coupling is weak, spontaneous Raman scattering is typically observed in 1 in 10^8 photons [25], requiring any spectrometer for

Raman spectroscopy to have a high signal-to-noise ratio (SNR). Alternative stimulated Raman schemes are possible which increase SNRs of the Raman signals, however these typically require a tunable probe beam, and as such are less suited to ruggedised portable operation (due to limits on the stability of tunable lasers).

The pump beam must also be chosen to match detectors. CMOS detectors can exhibit high quantum efficiency (conversion of photons to electrons) in the 550 nm to 900 nm wavelength range depending on detector cooling. InGaAs detectors are sensitive across the 900 nm to 1700 nm range, however 2D InGaAs arrays are much more expensive ($>$ £10 000), compared to CMOS detectors ($\approx$ £10).

A number of companies (Ocean Optics, Wasatch Photonics etc.) offer portable bulk spectrometers aimed at Raman spectroscopy. In their product specifications, Ocean Optics detail which detectors they use as well as details of signal to noise ratio and dynamic range. The HR4000, specifically designed for Raman spectroscopy [26], uses an uncooled Toshiba TCD1304AP detector and achieves a SNR of 300 : 1 and a dynamic range of 2×10^9 (though limited to 2×10^3 over a single measurement. In addition they list the stray light inside the spectrometer ($<$0.05% at 600 nm and $<$0.1% at 435 nm). This provides a benchmark for SNR for devices fabricated as part of this thesis.

Recently low-cost demonstrations of Raman spectroscopy have been shown using off-the-shelf components [27] and even using a laser pointer for a pump source [28]. A low-cost portable Raman spectrometer could be used for rapid testing of drugs and other complex compounds [29], [30] or for securing evidence at a crime scene. The first step to realising such a device is the development of an integrated spectrometer platform. The device would need to operate in the visible and near infrared (NIR) wavelength bands and span the spectral region for chemical fingerprints (800 cm^{-1} to 1800 cm^{-1}), which requires a bandwidth of 80 nm for detection at 870 nm and a bandwidth of 50 nm for detection at 690 nm.

Studies of chemical analysis using Raman spectroscopy give no clear consensus on the required spectral resolution to successfully identify compounds. Muhamadali et al. [30] showed analysis and quantification of a number of controlled psychoactive substances; the finest features of their spectral data were separated by 20 cm^{-1}, corresponding to a resolution of 1.6 nm at a wavelength of 870 nm. The data was captured using a commercially available Renishaw inVia system, with a spectral resolution of 0.3 cm^{-1}, corresponding to 23 pm at 870 nm [31]. A resolution target of 5 cm^{-1} was chosen; this provides enough precision to differentiate sharp features in spectra with limited SNR.

1.2.2 Optical coherence tomography (OCT)

Optical coherence tomography (OCT) is a non-invasive technique for measuring the scattering properties at different depths in a sample, in a manner similar to ultrasound

imaging. OCT is often used in medical imaging of tissue and eyes, as it is able to provide images of cross sections of samples with µm axial and lateral resolution.

Spectral-domain OCT uses a broadband source, an interferometer and a spectrometer to characterise samples. Different wavelengths accrue phases with distance at different rates (due to their wavevectors). The difference in phase between a wavelength in the sample and reference arm will modulate the signal, creating an interferogram in the frequency domain. Spectral interrogation of the signal output from the interferometer will allow analysis of depth information to reconstruct the scattering profile. A scanning mirror is normally used to build up a line scan or an image from multiple single-point interferograms. For a more detailed discussion see [32].

The spectral properties of the light source and measurement properties of the spectrometer dictate the performance of the OCT system. The lateral resolution of the system is given by the resolution of the imaging system, which is ultimately limited by the imaging wavelength. The maximum depth, $z_{\max}$, and axial resolution, δ_z, are given by a combination of the source bandwidth and spectrometer characteristics [32]:

$$\delta_z = \frac{2\ln 2}{\pi}\frac{\lambda_0^2}{\Delta\lambda_{\mathrm{FWHM}}}, \tag{1.1}$$

$$z_{\max} = \frac{1}{4}\frac{\lambda_0^2}{\delta\lambda}N, \tag{1.2}$$

where λ_0 is the centre wavelength of the device, $\Delta\lambda_{\mathrm{FWHM}}$ is the 3 dB bandwidth of the system, $\delta\lambda$ is the wavelength resolution and N is the number of pixels on the spectrometer detector. Increasing spectral bandwidth increases the axial resolution of OCT. The maximum depth is proportional to the number of discrete spectral channels (which depends on the ratio of resolution to bandwidth).

Two wavelengths commonly used in OCT are 800 nm and 1300 nm as they correspond to dips in the absorption spectrum of water. 800 nm is more typically used in ophthalmic imaging to avoid absorption in the eye [33]. For imaging of tissue 1300 nm light is often preferred as the longer wavelengths experiences less scattering from tissue [34]. Requirements for OCT can be analysed using equations 1.1 & 1.2. Spectral resolutions of 2 nm and bandwidths of 150 nm and 370 nm would be required to perform OCT at 800 nm and 1300 nm respectively, achieving > 1 mm depth of field with a 1024 element detector and suitable resolution to analyse biological structures.

Due to the advent of supercontinuum generation there are many potential sources which more than satisfy the bandwidth requirements of the device in integrated [35], [36] and fibre platforms [37], [38] that are suitable for a miniaturised platform. As such we will consider the optical bandwidth of the OCT system to be limited by the spectrometer.

1.2.3 Hyperspectral imaging

Hyperspectral imaging is a technique where spectral data beyond the typical RGB values are recorded for every pixel. This allows analysis of absorption and reflectance features across a wide spectral band. It is a non-destructive testing method and is of particular interest within food monitoring and medical imaging [39], [40]. Commonly, hyperspectral imaging uses a line scan method [40]: a narrow slit is used to image a line across a sample through a grating or prism. The line is mapped to one spatial axis of the detector, with the spectral information encoded on the other axis. A 2D hyperspectral image can then be built up by scanning the line across the object. Alternatively images can be taken through a tunable wavelength filter to capture images over different narrow wavelength bands and build up a hyperspectral image. Both these approaches require multiple exposures to build a hyperspectral image; generating full hyperspectral images is much slower than conventional imaging, with typical acquisition times of ms per spectral band [41].

A low-cost integrated spectrometer could pave the way to high-speed hyperspectral imaging to observe dynamic processes. By multiplexing devices together a large area could be imaged using a fibre bundle to route imaging pixels to spectrometers. Such a device would preserve the étendue of a typical hyperspectal imaging system.

Lu et al. [40] summarises wavelength ranges and spectral resolutions used to analyse a wide range of medical applications. Typical medical applications operate in the 450 nm to 700 nm range, with a few devices operating up to 1000 nm. A useful device would work in the visible wavelength range, and possibly as far as the NIR. Devices used in medical applications have resolutions of between 1 nm and 10 nm, though publications rarely address the variation in spectral resolution across the operating bandwidth of the system. Gowen et al. [39] presents a similar review of hyperspectral imaging in food analysis. The wavelength ranges and resolution requirements are similar to those found by Lu. It is possible this simply reflects the current level of performance of hyperspectral imaging systems, rather than the requirement for a useful system.

1.3 Summary

Using the previously described literature as a guide, target characteristics for devices in each of the listed applications are shown in tables 1.2, 1.3, 1.4. The applications all required devices in the visible and NIR spectral regions. Raman spectroscopy requires the smallest bandwidth and the highest resolution. In addition Raman spectroscopy also requires a platform that has low scattering, low fluorescence and low loss, as well as the ability to remove pump light (via filtering) before it reaches the detector. OCT requires a larger bandwidth to achieve high axial resolution, though the parameters shown in

Pump wavelength (nm)	532	633	780
Detection wavelength (nm)	570	690	870
Bandwidth (nm)	35	50	80
Resolution (nm)	0.15	0.22	0.35
SNR (dB)	33 dB		

TABLE 1.2: Target spectrometer parameters for Raman spectroscopy

Design wavelength (nm)	800	1300
Bandwidth (nm)	150	370
Resolution (nm)	2	2

TABLE 1.3: Target spectrometer parameters for OCT

	Visible	Visible and NIR
Wavelength range (nm)	450 - 700	450 - 1000
Resolution (nm)	1 - 10	1 - 10

TABLE 1.4: Target spectrometer parameters for hyperspectral imaging

table 1.2 for Raman spectroscopy would likely be of interest for a low-cost OCT system. Hyperspectral imaging requires very high bandwidth and low resolution. Such a device is likely to be difficult to achieve in a waveguide platform, as higher-order modes from short wavelengths are likely to interfere with spectrometer operation without significant waveguide engineering.

Devices are intended to be used in a portable manner, so the footprint should be small. Existing companies (Ocean Optics, Thorlabs) offer 'compact' spectrometers with a volume of less than $300\,\mathrm{cm}^3$, largely limited by the space required by beam paths inside the device. I propose a limit on the size of integrated optics to $20\,\mathrm{mm} \times 10\,\mathrm{mm}$ to reduce the effects of propagation loss and mechanical instability across the device. It is expected that the bulk of the volume of the device will be attributed to processing electronics at the prototyping phase, however once a design has been finalised purpose built electronics should allow fibre-in spectrometer package with a volume less than $10\,\mathrm{cm}^3$.

The spectrometer schemes shown in table 1.1 tend to focus on resolution, however for the applications discussed in this chapter bandwidth is the limiting factor. Redding et al. [14] have shown a device with high bandwidth and good resolution, however it is poorly suited to portable use, with environmental stability and mechanical stability both concerns. Similar concerns about environmental stability also apply to AWG schemes with sufficient FSR to be of interest, such as those shown by Takada et al. [9]. The planar holograms shown by Calafiore et al. [11] use a dispersive spectrometer regime which will be more robust to temperature variations, while still providing good resolution and bandwidth. However stray light due to the etched SiN platform and poor mode matching to the optical fibre input limits the SNR potential. The waveguide schemes shown in table 1.1 show potential. The devices are dispersive, so will be tolerant to

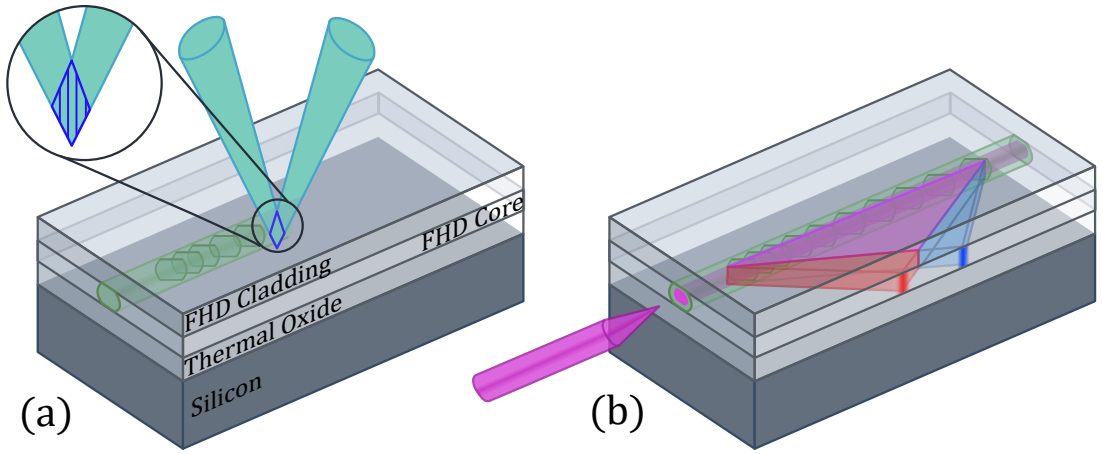

FIGURE 1.1: Proposed highly-chirped 45° blazed Bragg grating spectrometer scheme. a) FHD platform and ssDUW fabrication of gratings and channel waveguide inside photosensitive core layer. b) Input spectra coupling into channel waveguide is diffracted out of the channel waveguide into a planar waveguide. The light focuses onto the side facet, where a detector will be mounted.

temperature fluctuations. The device in silicon [17] exhibits a good bandwidth and small footprint, although the spectral resolution is limited by the output coupler design. The devices in silica [15], [16] are attractive due to the low refractive index contrast platform, which should minimise scatter. In addition they also show the potential for high spectral resolution in this scheme.

1.4 Proposed scheme

We propose a spectrometer scheme using highly-chirped, 45° blazed Bragg gratings in a photosensitive silica-on-silicon platform. The small-angle scheme shown by Madsen et al. [16] was promising, but suffered from extremely long focal length, birefringent wavelength shift, and low-bandwidth. To improve on this, my work proposes to exploit Brewster's angle using 45° Bragg gratings; resulting in only one polarisation state being diffracted by the waveguide [42]. The grating period and chirp can then be designed to focus light onto the side facet of the detector by diffracting light 90° out of the grating, as shown in figure 1.1b. 45° degree gratings also show a much wider transmission reflection bandwidth than small angle gratings [43] so such a device is likely to exhibit greater bandwidth. The multilayer silica platform shown in figure 1.1a has a germanium doped core layer. This has a higher refractive index, so creates a planar waveguide and is also photosensitive: small-spot direct UV writing (ssDUW) can be used to create channel waveguides and highly chirped Bragg gratings (necessary for short focal lengths) inside the core layer. The channel waveguide inside the planar waveguide will avoid loss from mode-matching and interfaces seen in previous approaches by Madsen et al. [16].

The index contrast of gratings fabricated via ssDUW is relatively small (3×10^{-3}) [42], devices will have to be longer to compensate for the low reflectivity.

ssDUW waveguides fabricated in Southampton have already been shown to have low propagation and coupling losses [44], and previous work within our research group [45] has shown that highly uniform gratings can be achieved, both of which should reduce the stray light inside the device for Raman spectroscopy.

This is the first work from the University of Southampton that investigates the properties of blazed chirped Bragg gratings. I demonstrate the viability of a blazed chirped Bragg grating spectrometer platform and explore the physics principles behind these devices to optimise their performance for various applications. The goals of this research can be broadly encapsulated in a number of questions:

- Do 45° low-index contrast blazed Bragg gratings diffract enough light to make useful spectrometers?
- Can we model the output of the device for a given wavelength to predict performance?
- What factors control the spectral resolution of the device?
- What factors control the response bandwidth of the device?
- Are the proposed devices fabricable?

1.5 Outline of thesis

Chapter 2 presents an introduction to the flame hydrolysis deposition (FHD) and ssDUW fabrication platform. The method of twin beam UV writing with phase control is presented to show how chirped gratings, or gratings with different periods are fabricated.

Chapter 3 presents theory on planar and channel waveguides, as well as the spectral properties of Bragg gratings. A number of waveguides and Bragg gratings are fabricated in a new FHD layer recipe which supports a strong planar waveguide at a 780 nm wavelength. The spectral properties of the fabricated Bragg gratings are used to characterise ideal fabrication parameters for spectrometer gratings.

Chapter 4 presents work on modelling blazed chirped Bragg gratings. A ray model is used to predict the focal length and dispersion of devices. Ray intercept diagrams are used to analyse the aberrations present in previous schemes and correct for such aberrations. A beam propagation model is used to calculate the electric field during propagation and image the beam waist through the focus. Finally a scalar diffraction

model is used to investigate device bandwidth, the effects of blaze angle and potential detector mounting geometries.

Chapter 5 details work to correct for primary coma aberration apparent in devices with a linear period chirp. Beam propagation modelling is used to identify the cause of discrepancies between the observed resolution and that predicted by Gaussian optics and ray modelling.

Chapter 6 presents work on fabricating gratings with variable blaze angle at 780 nm in an effort to increase resolution without increasing the device footprint. In addition a move to 780 nm satisfies requirements for low-cost devices. A custom C++ library was created to allow coordinate transformations and rotate the sample whilst writing.

Chapter 7 summarises the findings in this thesis, as well as discussing potential future work.

1.6 References

[1] B. Ramsay, E. Cleveland, and O. Koppius, "Criteria and the intensity epoch slope," *Journal of the Optical Society of America*, vol. 31, pp. 26–33, 1941.

[2] U. Paudel and T. Rose, "Ultra-high resolution and broadband chip-scale speckle enhanced Fourier-transform spectrometer," *Optics Express*, vol. 28, no. 11, pp. 16 469–16 485, 2020.

[3] J. den Dekker A and A. van den Bos, "Resolution: A survey," *Journal of the Optical Society of America*, vol. 14, no. 8, pp. 547–557, 1997.

[4] A. Velasco, P. Cheben, P. J. Bock, A. Delâge, J. Lapointe, S. Janz, M. Calvo, D. Xu, M. Florjańczyk, and M. Vachon, "High-resolution Fourier-transform spectrometer chip with microphotonic silicon spiral waveguides," *Optics Letters*, vol. 38, no. 5, pp. 706–708, 2013.

[5] S. Wielandy and S. C. Dunn, "Tilted superstructure fiber grating used as a Fourier-transform spectrometer," *Optics Letters*, vol. 29, no. 14, pp. 1614–1616, 2004.

[6] P. Cheben, J. H. Schmid, A. Delâge, A. Densmore, A. Janz, B. Lamontagne, J. Lapointe, P. E., P. Waldron, and D. Xu, "A high-resolution silicon-on-insulator arrayed waveguide grating microspectrometer with sub-micrometer aperture waveguides," *Optics Express*, vol. 15, no. 5, pp. 2299–2306, 2007.

[7] B. I. Akca, V. D. Nguyen, J. Kalkman, N. Ismail, G. Sengo, F. Sun, A. Driessenm, T. G. van Leeuwen, M. Pollnau, K. Wörhoff, and R. M. de Ridder, "Towards spectral-domain optical coherence tomography on a silicon chip," *IEEE Journal of Selected Topics in Quantum Electronics*, vol. 18, no. 3, pp. 1223–1233, 2011.

[8] N. Ismail, L. Choo-Smith, K. Wörhoff, A. Driessen, A. C. Baclig, P. J. Caspers, G. J. Puppels, R. M. de Ridder, and M. Pollnau, "Raman spectroscopy with an integrated arrayed-waveguide grating," *Optics Letters*, vol. 36, no. 23, pp. 4629–4631, 2011.

[9] K. Takada, M. Abe, and K. Okamoto, "5 GHz-spaced 4200-channel two-stage tandem demultiplexer for ultra-multi-wavelength light source using supercontinuum generation," vol. 38, no. 12, pp. 572–573, 2002.

[10] X. Ma, M. Li, and J. He, "CMOS-compatible integrated spectrometer based on echelle diffraction grating and MSM photodetector array," *IEEE Photonics Journal*, vol. 5, no. 2, 2013.

[11] G. Calafiore, A. Koshelev, S. Dhuey, A. Goltsov, P. Sasorov, S. Babin, V. Yankov, and C. Cabrini S.and Peroz, "Holographic planar lightwave circuit for on-chip spectroscopy," *Light: Science and Applications*, vol. 3, no. 9, pp. 1–7, 2015.

[12] C. Peroz, A. Goltsov, S. Dhuey, P. Sasorov, B. Harteneck, I. Ivonin, S. Kopyatev, S. Cabrini, S. Babin, and V. Yankov, "High-resolution spectrometer-on-chip based on digital planar holography," *IEEE Photonics Journal*, vol. 3, no. 5, pp. 888–896, 2011.

[13] B. Redding, S. F. Liew, R. Sarma, and H. Cao, "Compact spectrometer based on a disordered photonic chip," *Nature Photonics*, vol. 7, pp. 746–751, 2013.

[14] B. Redding, M. Alam, M. Seifert, and H. Cao, "High-resolution and broadband all-fiber spectrometers," *Optica*, vol. 1, no. 3, pp. 175–180, 2014.

[15] J. L. Wagener, T. A. Strasser, J. R. Pedrazzani, J. DeMarco, and D. DiGiovanni, "Fiber grating optical spectrum analyzer tap," in *11th International Conference on Integrated Optics and Optical Fibre Communications and 23rd European Conference on Optical Communications*, vol. 5, 1997, pp. 65–68.

[16] C. K. Madsen, J. Wagener, T. A. Strasser, M. A. Muehlner, E. J. Laskowski, and J. DeMarco, "Planar waveguide optical spectrum analyzer using a UV-induced grating," *IEEE Journal of Quantum Electrononics*, vol. 4, no. 6, pp. 925–929, 1998.

[17] P. J. Bock, P. Cheben, J. H. Schmid, A. V. Velasco, A. Delâge, S. Janz, D. Xu, J. Lapointe, T. J. Hall, and M. L. Calvo, "Demonstration of a curved sidewall grating demultiplexer on silicon," *Optics Express*, vol. 20, no. 18, pp. 19 882–19 892, 2012.

[18] S. Babin, A. Bugrov, S. Cabrini, S. Dhuey, A. Goltsov, I. Ivonin, E. B. Kley, C. Peroz, H. Schmidt, and V. Yankov, "Digital optical spectrometer-on-chip," *Applied Physics Letters*, vol. 95, no. 4, pp. 2–5, 2009.

[19] B. Redding, S. M. Popoff, and H. Cao, "All-fiber spectrometer based on speckle pattern reconstruction," *Optics Express*, vol. 21, no. 5, pp. 6584–6600, 2013.

[20] G. Meltz, W. Morey, and W. Glenn, "In-fiber Bragg grating tap," *Optical Fiber Communication*, TUG1, 1990.

[21] G. Meltz, W. M. Morey, and A. L. Wilson, "Optical waveguide embedded light redirecting and focusing Bragg grating arrangement," U.S. Patent 5 061 062, 1991.

[22] C. Koeppen, J. L. Wagener, T. A. Strasser, and J. DeMarco, "High resolution fibre grating optical network monitor," in *National Fibre Optic Engineers Conference*, 1998, Session 17 paper 2.

[23] D. A. Long, "Raman spectroscopy," in *The Characterisation of Chemical Purity: Organic Compounds*, Elsevier, 1970, ch. 10.

[24] P. Matousek, M. Towrie, C. Ma, W. M. Kwok, D. Phillips, W. T. Toner, and A. W. Parker, "Fluorescence suppression in resonance Raman spectroscopy using a high-performance picosecond Kerr gate," *Journal of Raman Spectroscopy*, vol. 32, pp. 983–988, 2001.

[25] R. R. Jones, D. C. Hooper, L. Zhang, D. Wolverson, and V. K. Valev, "Raman Techniques: Fundamentals and frontiers," *Nanoscale Research Letters*, vol. 14, no. 1, pp. 1–34, 2019.

[26] Ocean Optics, *Document Number 210-00000-000-02-1006*, HR4000 and HR4000CG-UV-NIR Series High-Resolution Fiber Optic Spectrometers.

[27] O. Aydogan and E. Tasal, "Designing and building a 3D printed low cost modular Raman spectrometer," *CERN IdeaSquare Journal of Experimental Innovation*, vol. 2, no. 2, pp. 3–12, 2018.

[28] W. R. C. Somerville, E. C. Le Ru, P. T. Northcote, and P. G. Etchegoin, "High performance Raman spectroscopy with simple optical components," *American Journal of Physics*, vol. 78, no. 7, pp. 671–677, 2010.

[29] J. S. Day, H. G. M. Edwards, S. A. Dobrowski, and A. M. Voice, "The detection of drugs of abuse in fingerprints using Raman spectroscopy I: Latent fingerprints," *Spectrochimica Acta - Part A: Molecular and Biomolecular Spectroscopy*, vol. 60, no. 3, pp. 563–568, 2004.

[30] H. Muhamadali, A. Watt, Y. Xu, M. Chisanga, A. Subaihi, C. Jones, D. I. Ellis, O. B. Sutcliffe, and R. Goodacre, "Rapid detection and quantification of novel psychoactive substances (NPS) using Raman spectroscopy and surface-enhanced Raman scattering," *Frontiers in Chemistry*, vol. 7, no. 412, pp. 1–10, 2019.

[31] Renishaw, *InVia^{TM} confocal Raman microscope*, Part number: BR010-03-A L-9836-4969, 2019.

[32] S. D. Aumann, J. Fischer, and F. Müller, "Optical coherence tomography(OCT): Principle and technical realization," in *High Resolution Imaging in Microscopy and Ophthalmology*, Springer, 1970, ch. 3.

[33] W. Drexler, U. Morgner, R. K. Ghanta, F. X. Kärtner, J. S. Schuman, and J. G. Fujimoto, "Ultrahigh-resolution ophthalmic optical coherence tomography," *Nature Medicine*, vol. 7, no. 4, pp. 502–506, 2001.

[34] I. Hartl, X. D. Li, C. Chudoba, R. K. Ghanta, T. H. Ko, J. G. Fujimoto, J. K. Ranka, and R. S. Windeler, "Ultrahigh-resolution optical coherence tomography using continuum generation in an air–silica microstructure optical fiber," *Optics Letters*, vol. 26, no. 9, pp. 608–610, 2001.

[35] J. P. Epping, T. Hellwig, M. Hoekman, R. Mateman, A. Leinse, R. G. Heideman, A. van Rees, P. J. M. van der Slot, C. J. Lee, C. Fallnich, and K. Boller, "On-chip visible-to-infrared supercontinuum generation with more than 495 THz spectral bandwidth," *Optics Express*, vol. 23, no. 15, pp. 19 596–19 604, 2015.

[36] H. Zhao, B. Kuyken, F. Leo, S. Clemmen, E. Brainis, G. Roelkens, and R. Baets, "Visible-to-near-infrared octave spanning supercontinuum generation in a silicon nitride waveguide," *Optics Letters*, vol. 40, no. 10, pp. 2177–2180, 2015.

[37] J. K. Ranka, R. S. Windeler, and A. J. Stentz, "Visible continuum generation in air–silica microstructure optical fibers with anomalous dispersion at 800 nm," *Optics Letters*, vol. 25, no. 1, pp. 25–27, 2000.

[38] X. Jiang, N. Y. Joly, M. A. Finger, F. Babic, G. K. L. Wong, J. C. Travers, and P. S. J. Russell, "Deep-ultraviolet to mid-infrared supercontinuum generated in solid-core ZBLAN photonic crystal fibre," *Nature Photonics*, vol. 9, no. 2, pp. 133–139, 2015.

[39] A. A. Gowen, C. P. O'Donnell, P. J. Cullen, G. Downey, and J. M. Frias, "Hyperspectral imaging - an emerging process analytical tool for food quality and safety control," *Trends in Food Science and Technology*, vol. 18, no. 12, pp. 590–598, 2007.

[40] G. Lu and B. Fei, "Medical hyperspectral imaging: a review," *Journal of Biomedical Optics*, vol. 19, no. 1, pp. 10 901–10 923, 2014.

[41] R. Jackisch, S. Lorenz, R. Zimmermann, R. Möckel, and R. Gloaguen, "Drone-borne hyperspectral monitoring of acid mine drainage: An example from the Sokolov lignite district," *Remote Sensing*, vol. 10, pp. 1–23, 2018.

[42] M. T. Posner, N. Podoliak, D. H. Smith, P. L. Mennea, P. Horak, C. B. E. Gawith, P. G. R. Smith, and J. C. Gates, "Integrated polarizer based on 45° tilted gratings," *Optics Express*, vol. 27, no. 8, pp. 11 174–11 181, 2019.

[43] K. Zhou, G. Simpson, X. Chen, L. Zhang, and I. Bennion, "45° tilted fiber Bragg gratings," *Optics Letters*, vol. 30, no. 11, pp. 1285–1287, 2005.

[44] H. L. Rogers, S. Ambran, C. Holmes, P. G. R. Smith, and J. C. Gates, "In situ loss measurement of direct UV-written waveguides using integrated Bragg gratings.," *Optics letters*, vol. 35, no. 17, pp. 2849–2851, 2010.

[45] R. Bannerman, "Microfabrication of waveguide devices for quantum optics," Ph.D. dissertation, 2019.

Chapter 2

Small-spot direct UV writing

This chapter serves as an introduction to the UV written FHD silica platform used to make all devices in this thesis which has been developed over the last 20 years. FHD silica fabrication and photosensitivity are discussed and contrasts are drawn with photosensitivity mechanisms seen in silica fibres. The small-spot direct UV writing (ssDUW) is introduced with particular attention to the electro-optic modulator (EOM) phase control system, which allows rapid prototyping of different devices and Bragg gratings without use of a phase mask.

During my PhD I have helped maintain the system alongside other researchers, as well as designing and building new interferometer boards with computer aided design (CAD) support from Rex Bannerman and Devin Smith, and machining support from Sam Berry and Glenn Topley.

2.1 Flame hydrolysis deposition

Flame hydrolysis deposition (FHD) is a process of fabricating micron scale glass layers from high purity liquid precursors and is commonly used as a platform for etched devices within the telecommunications industry. Precursors are combined in an oxy-hydrogen flame to form a glass soot which can be consolidated into a thin, uniform layer of doped silica glass using a furnace. The system in Southampton uses $SiCl_4$, $GeCl_4$, PCl_3 and BCl_3 as precursors; they are available in high purity, in part due to their use in silica fibre manufacture. A bubbler system is used to house liquid precursors at controlled temperatures and pressures and deliver vapours at a specified rate. The precursors are fed into a torch and combined in a high-temperature (>1400 °C) oxy-hydrogen flame which passes over a rotating platen, as shown in figure 2.1, upon which substrate wafers are mounted. Inside the flame the precursors react to form a white doped silica 'soot' of amorphous silica particles ($< 50\,\mu m$ in size depending on flame conditions [1]) along

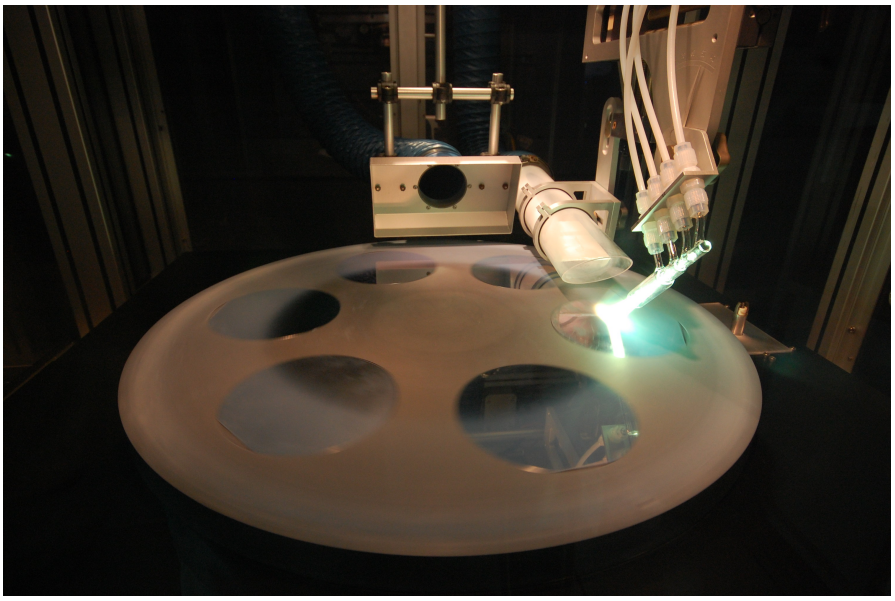

FIGURE 2.1: The FHD deposition system during a deposition run. The torch appears blue due to the boron dopants in the flame. The FHD layer can be seen as a white coating across the platen.

with HCl and water

$$SiCl_4 + 2\,H_2O \longrightarrow SiO_2 + 2\,HCl, \tag{2.1}$$

$$SiCl_4 + O_2 \longrightarrow SiO_2 + 2\,Cl_2. \tag{2.2}$$

The processes described by equations 2.1 and 2.2 are respectively hydrolysis and oxidation. Oxidation takes place in higher temperature environments (in the centre of the torch), hydrolysis takes place at lower temperatures. The platen is heated during deposition to prevent condensation of water, however the glass is still inherently wet and exhibits characteristic water absorption. After deposition the glass soot must undergo a consolidation process to convert it from an opaque white fluffy layer to a uniform glass film. Silicon substrate wafers which have been deposited with FHD soot are heated to a consolidation temperature (typically 1360 °C and 1200 °C respectively for core and cladding layers) and held at this temperature for 2 h to 3 h. Though this is far below the melting temperature of the glass it is hot enough to viscous reflow the glass [2]. As the glass heats it slowly transitions to a liquid, becoming less viscous but not fully melting. Once it gets to the consolidation temperature the particulates of glass soot overcome surface tension and wet together to form a uniform layer, in much the same manner as powder sintering. The glass then must be cooled fast enough to prevent crystallisation, but slow enough to prevent cracking due to thermal expansion. Choice of substrate is also important; silicon wafers provide good thermal and mechanical stability but have high refractive index. Pure silica wafers have the correct refractive index but the thermal expansion mismatch between germanium doped layers and pure silica results in tensile stress, which results in micro-cracking in deposited layers [3]. Silicon wafers with

a thermal oxide (THOX) layer provide a good compromise; the THOX layer of pure silica has the correct refractive index and can be grown thick enough to provide ample undercladding (typically 15 µm). The THOX layer layer is also thin enough that the deposited layer experiences compressive stress from the silicon wafer rather than tensile stress from the silica. After a single layer has been deposited additional layers may be deposited on top to create multi-layer stacks. Layers deposited later in a recipe are designed to use a lower consolidation temperature to reduce dopant migration between different layers.

Dopants are used to control the refractive index, photosensitivity and consolidation temperatures of glass layers. Doping a layer with germanium increases the refractive index and makes the layer photosensitive to UV light. Co-doping the layer with boron promotes this photosensitivity and decreases the refractive index [4]. Doping with phosphorous increases the refractive index without adding significant photosensitive properties. Addition of any of these dopants reduce the consolidation temperature of the glass. Creating FHD substrates for ssDUW requires deposition of a core and a cladding layer; the near-pure silica THOX layer is typically used as an undercladding as well as a thermal expansion buffer. The index change from the UV writing process is weak ($<5 \times 10^{-3}$) so the FHD refractive index profile has a strong influence on the final waveguide mode structure. Every deposition run includes a test wafer as well as any process wafers; the thickness and refractive index of the deposited glass can be measured from the test wafer using a Metricon 2010 prism coupler. The mode properties of devices after ssDUW can be modelled using the measured thicknesses and refractive indices of deposited layers, along with known properties of the writing beam. This allows pre-emptive modification of the wafer recipes before writing takes place, decreasing the time required to optimise devices.

2.2 Photosensitivity

Silica glasses exhibit a number of different mechanisms for UV photosensitivity, depending on fabrication method and composition. Excluding effects observed above the damage threshold of the glass (which induce significant scattering losses, which are to be avoided) doped silica glasses exhibit refractive index changes from photochemical changes in defects, densification and changes in stresses [5]. Densification and changes in stress lead to some of the more complex dynamics seen in Bragg grating formation in optical fibres (Bragg wavelength blue shift with increasing fluence, grating erasure and regeneration at high fluence, etc.). These more complex effects are not typically observed in UV written FHD samples; the fluence required to see such effects generates enough refractive index to disturb the waveguide mode significantly and mask these effects. Due to the limiting factor of the waveguides, gratings are investigated across a relatively narrow range of refractive index contrasts compared to optical fibres. As

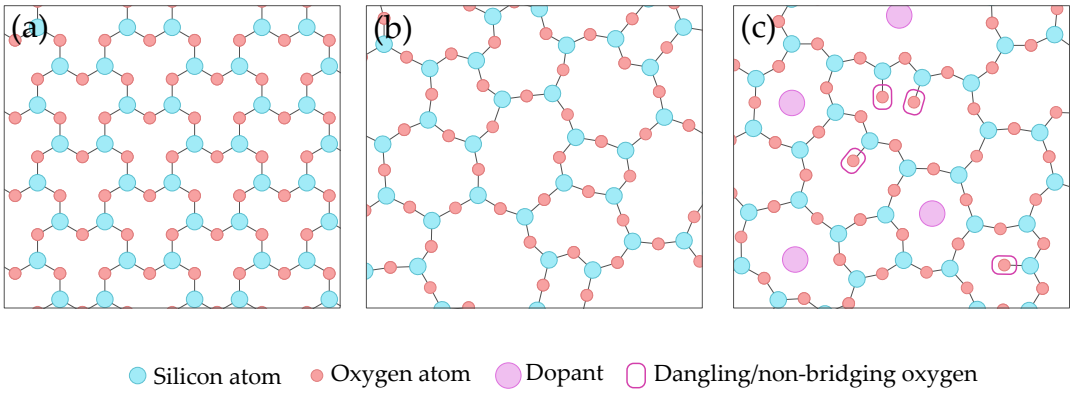

FIGURE 2.2: Structure of crystalline and amorphous materials. a) 'Flattened' crystalline SiO_2 structure with regular repeating units. b) Amorphous glass structure. Chemical species still make the same number of bonds however band angles are distorted due to the irregular structure. c) Examples of defects in amorphous glass.

such refractive index contrasts monotonically increase with increasing fluence within the regime where waveguides and gratings are fabricated simultaneously in a single pass.

2.2.1 UV-induced photochemical refractive index change

Though they lack a repeating unit cell, amorphous glasses have a recurring bond structure as shown in figure 2.2b. This imposes a condition on bonding angles and lengths. As such it is possible for defects in the amorphous structure to form (figure 2.2c shows some possible defects due to doping and dangling oxygen bonds). Silica glass has a number of absorptions in the 4 eV to 6 eV region [6] which correspond to photochemical changes in the bonding structure. Any change in the absorption properties of a material must be accompanied by an associated change in the refractive index of the material due to the Kramers-Kronig relation [7]. Addition of dopants leads to an increase in the variety of absorption defects, as well as disrupting the structure to increase the likelihood of bonding defects. Despite much research, the defects responsible for photosensitivity at 244 nm in germanosilicate glasses are still disputed [5], [6], [8]. Techniques used to identify defects in crystalline structures struggle with amorphous defects; the electronic structure surrounding the defect has a significant effect on the response of the defect itself. For the purposes of fabricating devices it is not necessary to understand the underlying glass chemistry, as the refractive index response is predictable and easily characterisable.

In addition to doping, samples require hydrogen indiffusion to exhibit significant photosensitivity at 244 nm. Lemaire et al. reported an increase in refractive index contrast from 3×10^{-5} to 5.9×10^{-3} in germanium doped fibres after hydrogen indiffusion. Indiffused hydrogen is thought to interact with the defect induced index change by stabilising UV-induced chemical changes with hydroxyl groups [9]. Work within our wider research

group has found that UV written FHD glass samples do not produce enough refractive index contrast to support waveguides without hydrogen loading, consequently all of our FHD samples are placed in a high-pressure ($\approx$ 120 bar) hydrogen environment for at least 72 h before UV writing. Deuterium loading has also been trialled, as literature suggests that it may result in lower loss than hydrogen near 1550 nm due to the shift in the OH overtone from 1.4 µm to 1.9 µm for OD [9]. As of yet initial tests in Southampton have not shown significant differences in hydrogen loading and deuterium loading, as such hydrogen is generally preferred over deuterium in integrated chips due to reduced cost.

Hydrogen rapidly outgasses after planar silica chips are removed from the pressure cell. Previous modelling has shown that within an hour the hydrogen concentration inside a planar layer with a 15 µm cladding layer has reduced by half [10]. Typically 3 h is used as a hard time limit for UV writing to ensure waveguides/gratings are fabricated. Chips are stored in liquid nitrogen after removal from the hydrogen cell; modelling from previous students has shown the diffusion rate becomes negligible in this case [10]. Methods of eliminating hydrogen outgassing have also been investigated for applications where processing leaves samples too delicate to store in the pressure cell, or where writing times exceed the outgassing time. Hydrogen can be 'thermally locked' into a sample using a rapid thermal annealing process [11]–[13]. This allows samples to be written at a later date (after further processing for example). Alternatively, other work within our research group is investigating ssDUW using a nanosecond pulsed 213 nm laser. It has been found that this can achieve induced refractive indices of 2.4×10^{-3} without hydrogen loading [14].

2.2.2 Densification

Densification is a change in the density of a glass sample under exposure to UV light. This change in density causes an associated change in the refractive index [15] alongside photochemical changes. Densification is closely related to changes in stresses in the glass which also change the refractive index. Trenches have been observed in unclad FHD samples after UV exposure [10], providing direct evidence of densification in the core layer. In contrast PECVD samples under UV exposure have seen localised decreases in density [16]. Typically densification and stress effects cause changes in grating growth dynamics (blue shift of Bragg wavelength, partial erasure of gratings) at high exposures below the damage threshold. However in the regime where channel waveguides are formed densification merely contributes to the monotonic index increase with increasing fluence.

2.3 UV writing

Small-spot direct UV writing (ssDUW) is a method of defining Bragg gratings and waveguides in planar platform in a single-step process. Gratings are defined using computer control, and fabricated using an interferometer scheme with an EOM. This is substantially different from the typical phase mask scheme, where each device must use a different phase mask. The ssDUW scheme allows for low-cost, rapid prototyping of new devices whist implementing real-time feedback. This section focuses on the physical implementation of the UV writing scheme: the generation of the control signal and the capabilities that the scheme provides. Details about design and implementation of software control for fabrication of advanced devices can be found in chapter 6.

2.3.1 Phase mask method

The phase mask method is the most common method of fabricating Bragg gratings in photosensitive silica platforms. There are few requirements on the phase stability of the source, and gratings can be easily mass-produced with good repeatability. Waveguides are defined first, often via etching or using optical fibre, and Bragg gratings are added as a perturbation to the refractive index of the waveguide. In both these cases the cladding (air in the etched case, non-photosensitive glass in the fibre case) is not photosensitive, so the width of the exposure can be much larger than the core width of the waveguide. In such platforms Bragg grating definition is typically achieved using a phase mask method [17] where the sample is held stationary under a phase mask and exposed to a large UV beam. The grating is entirely controlled by the phase mask, as such it is difficult and expensive to iterate through different device designs. A number of other schemes [18]–[20] have made modifications to the basic phase mask scheme to allow a degree of customisation to the fabricated grating, either in apodisation or in grating period using a coherent beam and electro-optic phase control. These methods still use a large writing beam to take advantage of the stability of the phase mask scheme. Conversely the customisation is limited to the scale of the writing spot size. Some extra device flexibility is recovered in the fibre platform, gratings are often tuned after fabrication by applying tension or heat to the fibres to shift the Bragg wavelength of the response.

2.3.2 Small-spot direct UV writing

An alternative approach to the phase mask scheme was suggested by Stepanov [21] and was later developed, refined, and commercialised at Southampton. Instead of using a phase mask, a coherent writing beam and an interferometer can generate a set of interference fringes inside a diffraction limited spot for simultaneous fabrication of waveguides and gratings. The period of the interference pattern is set by the design of

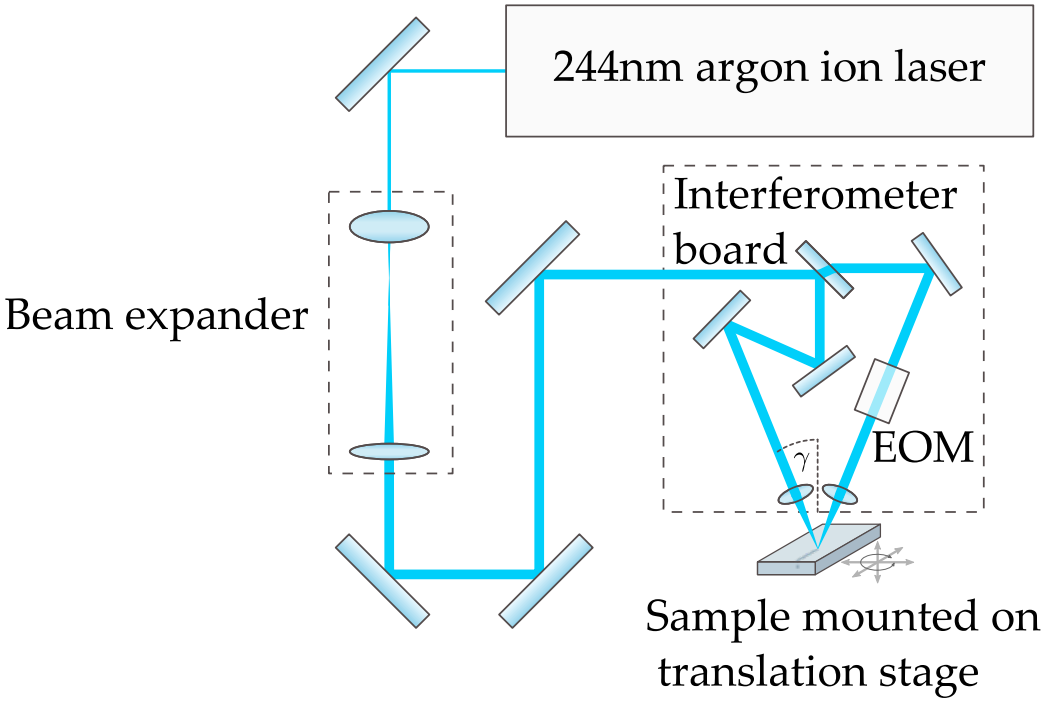

FIGURE 2.3: The 244 nm UV writing system.

the interferometer and can be readily changed. The tiny grating spot allows maximum customisation of fabricated gratings from a single interferometer, however it also requires more advanced control systems as it lacks the large scale stability of a phase mask.

All devices in this thesis are fabricated using a small ($\approx 5\,\mu m$) writing spot from a 244 nm frequency doubled argon ion laser. A sample is translated underneath the writing spot at a defined speed which traces the desired waveguide structure across the device. The waveguide width is primarily controlled by the width of the writing spot and the waveguide refractive index contrast is set by the laser power and the translation speed of the sample via the radiative fluence. Grating writing in this scheme is more complex than in the phase mask method but provides greater flexibility. Firstly, the writing spot is structured using a Michelson interferometer (see figure 2.3). The angle, γ, at which the beams are combined inside the interferometer (as well as the wavelength of the writing beams) defines the fringe period, Λ_0, of the interference pattern of the beams:

$$\Lambda_0 = \frac{\lambda_{uv}}{2\sin\gamma}, \tag{2.3}$$

where λ_{uv} is the writing wavelength. Before recombination each beam passes through a lens; the system is aligned such that the beams overlap at their foci, producing a small structured writing beam.

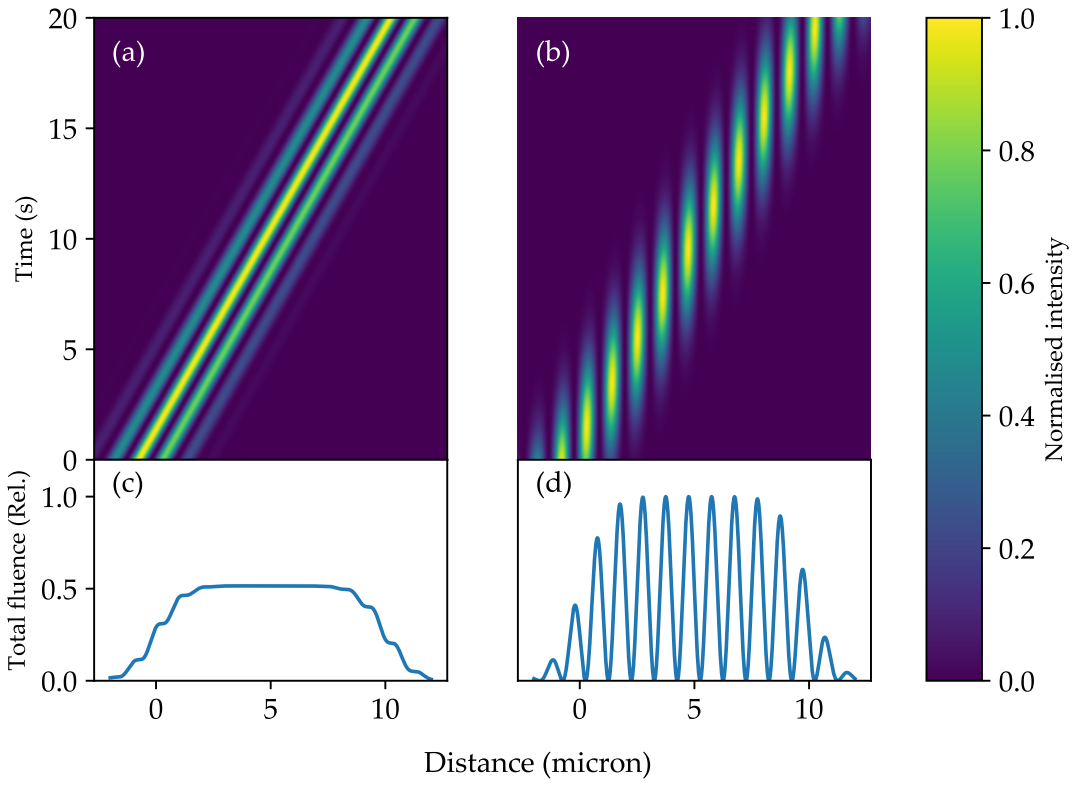

FIGURE 2.4: Evolution of the UV intensity distribution (from the stationary reference frame of the chip). By integrating the evolution over time we find the fluence distribution across the chip (bottom line plots), which is expected to be proportional to the refractive index contrast. a) Intensity distribution with no phase control, no grating fringes are observed. b) Intensity and fluence distribution with perfect linear phase control signal, resulting in grating fringes. c & d) fluence distributions resulting from integrating intensity distributions shown in a & b respectively over time.

Writing Bragg gratings with a structured beam requires further control systems; a stationary exposure results in a very short grating. However, moving the sample continuously averages out the index contrast of the device; the fluence absorbed by all points along the waveguide is the same, so no index variation is observed. Figure 2.4a shows the time evolution of the writing spot in this situation, figure 2.4c shows the total fluence by integrating the intensity from the writing spot over time (summing figure 2.4a vertically). More detail of this modelling can be found in appendix A. An EOM is present in one arm of the interferometer; supplying a control voltage to the EOM shifts the fringes relative to the writing spot. By supplying the correct control voltage it is possible to ensure fringes continue to constructively interfere whilst the sample is moving (see figure 2.4b and figure 2.4d).

To achieve maximum constructive interference of the writing spot fringes whilst writing a waveguide at a constant speed a linearly increasing EOM phase (and therefore linearly increasing driving voltage) is required. If we define $V_{2\pi}$ as the voltage required to shift the interference fringes by a single period using the EOM then the rate of voltage increase

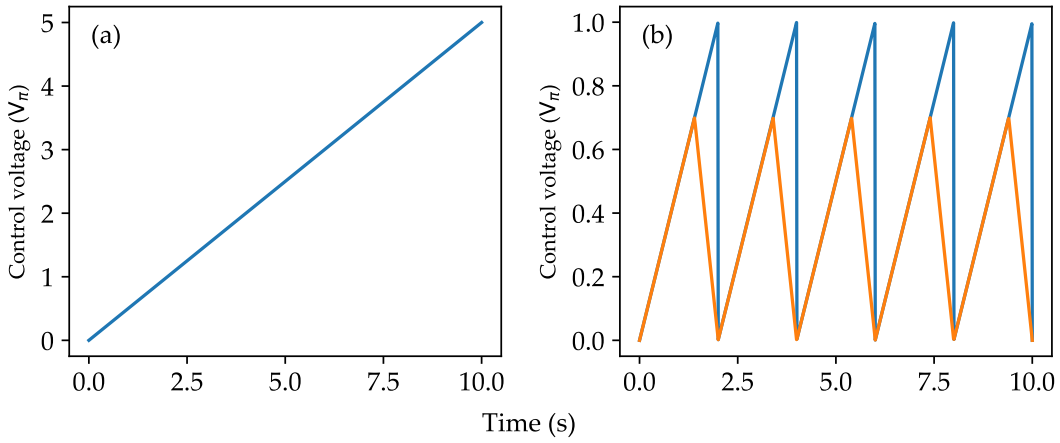

FIGURE 2.5: a) EOM ideal control voltage signals increasing at a constant rate. b) Phase control signal which reset every period, resulting in a lower peak voltage (blue and orange for high-slew rate and low-slew rate respectively).

should be

$$\frac{\mathrm{d}V}{\mathrm{d}t} = \frac{V_{2\pi} v}{\Lambda_0}, \tag{2.4}$$

where v is the writing speed. For a single mode waveguide with Bragg gratings at telecommunications wavelengths the fringe period is approximately 500 nm and $V_{2\pi} \approx 4.2\,\mathrm{kV}$. In a grating of 1 mm length this would result in a total increase in voltage of $\approx 10\,\mathrm{MV}$. Such large voltages would cause breakdown and arcing, which will likely damage equipment and endanger the user.

An alternative scheme developed and implemented in Southampton uses a much smaller voltage range and a high slew-rate amplifier. Once in every grating period the system resets the control voltage to 0 V, 'jumping' the fringes sideways one period such that constructive interference is still achieved while limiting the maximum required voltage to $V_{2\pi}$ (see figure 2.5b.). When the reset section of the signal is much shorter than a single period then the ratio of the ideal refractive index modulation to that achieved with the resetting signal can be approximated by the fraction of the period taken up by the reset signal:

$$\frac{\Delta n_{\mathrm{reset}}}{\Delta n_{\mathrm{ideal}}} = 1 - \frac{V_{2\pi}\sigma\Lambda_0}{v}, \tag{2.5}$$

where σ is the slew rate of the amplifier.Figure 2.6 shows the reduction in index contrast due to a slow amplifier slew-rate. The system in Southampton utilises a high slew-rate amplifier (700 V/µs) and results in minimal blurring. The achievable refractive index modulation with this reset rate and a writing speed of 6 mm/min is within 0.1 % of that achieved with an ideal EOM driving signal.

Such a scheme also allows controlled blurring of the interference fringes to control the refractive index contrast along the grating; this is referred to as the grating apodisation. When the grating control voltage is turned off or held constant it adds a blurred fluence

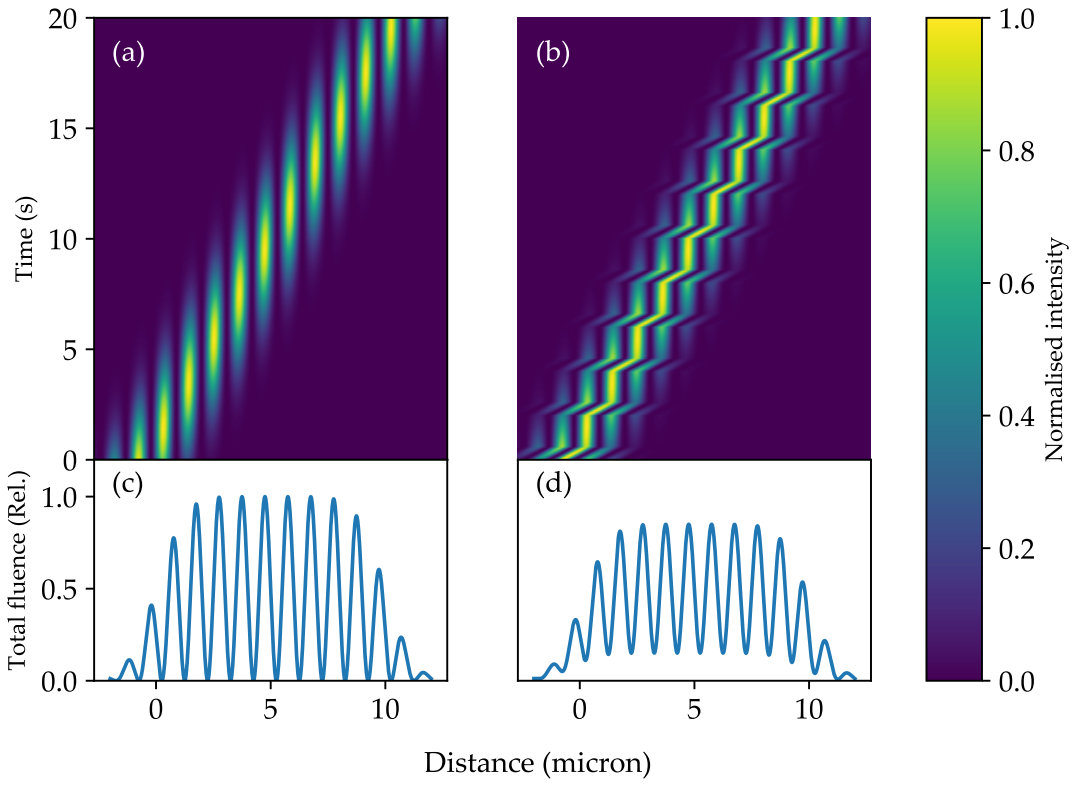

FIGURE 2.6: a) Intensity distribution and c) fluence distribution for grating with linear phase control signal. b) Intensity distribution and d) fluence distribution for resetting phase control signal with low slew-rate. The low slew-rate resetting significantly reduces the refractive index modulation compared to the linear signal.

distribution with no interference fringes. If instead of increasing the EOM drive voltage at all times we increase it for half a grating period, then hold it constant we achieve a 'partial blurring' which results in a weaker grating. Importantly this allows us to change the refractive index contrast of the grating whilst preserving the average refractive index contrast of the waveguide.

We can also detune the period of the grating by resetting the grating voltage with a period of Λ, rather than Λ_0, the period defined by the interferometer (see figure 2.7). The change in the reset period means that some of the interference fringes do not add constructively reducing the grating strength, however it does allow the grating period to be modified. The reduction in strength can be qualitatively analysed using the number of interference fringes in the writing spot. The reduction in grating strength comes from beating between the interference fringe period (Λ_0) and the desired grating period (Λ). The larger the difference between Λ_0 and Λ, the smaller the beat period between them. When the size of the writing spot becomes comparable to the beat period then the grating strength will be very weak. A full quantitative analysis of this effect has previously been attempted in previous group theses [10], [22] and is the subject of ongoing publications [23].

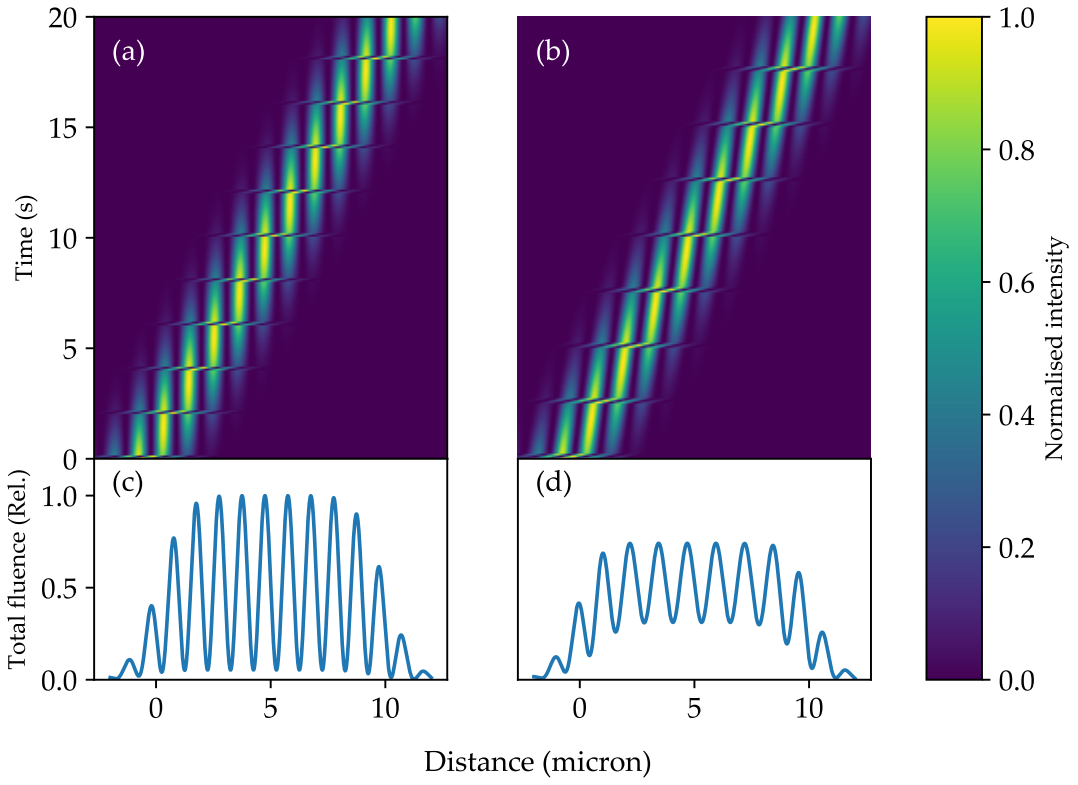

FIGURE 2.7: a) Intensity distribution and c) fluence distribution for grating with high slew-rate resetting phase control signal for a period Λ_0. b) Intensity distribution and d) fluence distribution for grating with high slew-rate resetting phase control signal for a period $\Lambda \neq \Lambda_0$. Detuning the grating period from the design period of the interferometer results in lower refractive index modulation.

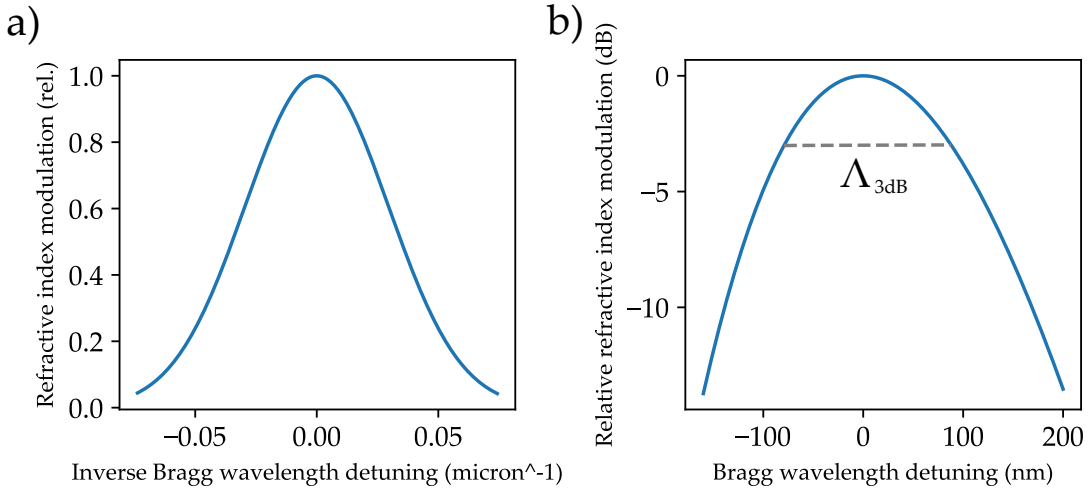

FIGURE 2.8: Relation between index modulation and period detuning (often referred to as the detuning curve) for grating writing at 1550 nm with a 2.5 µm Gaussian beam.

These works found that the achievable index contrast is well described by a Gaussian distribution in $1/\Lambda$ (as shown in figure 2.8), resulting in an asymmetric strength curve in Bragg wavelength[10]

$$\Delta n_{\max} = \exp\left[\frac{-\left(\frac{1}{\Lambda}-\frac{1}{\Lambda_0}\right)^2}{\sigma^2}\right], \tag{2.6}$$

$$\sigma = \frac{1}{\sqrt{\ln 2}}\left[\frac{1}{\Lambda_0 r}+\sqrt{\frac{1}{\Lambda_0^2}\left(1+\frac{1}{r^2}\right)}\right], \tag{2.7}$$

where r is the relative detuning width and is given by:

$$r = \frac{0.2703}{w}, \tag{2.8}$$

where w is the waist of the writing spot in µm. The 3 dB width of the detuning curve can be extracted as:

$$\Delta\Lambda_{3\mathrm{dB}} = r\Lambda_0 \tag{2.9}$$

These detuning effects are particularly important when considering the output of highly-chirped spectrometer devices as it substantially perturbs the spectrometer output.

2.4 Implementation of the phase control scheme

In the phase mask scheme it is simple to make short gratings, that is, gratings with a length smaller than the phase mask itself. The beam can be tailored to the correct size such that the grating is completed in a single exposure. The main concern in such a system is the stability of the interference pattern relative to the device. The small-spot scheme adds a greater degree of complexity by having a continuously moving sample. To produce high quality gratings the sample must be moved at a constant speed, and the period of the reset signal must be synchronised to the system. This is implemented using a nanometre resolution Aerotech A3200 4-axis stage system(the layout of the stage system is shown in figure 2.9). The stage system uses a feedback loop to ensure the position and velocity are accurate. Motion commands are given to the stage system using Aerobasic, a modified version of G code, different devices can be created by running different scripts on the control PC. The stage system also has analogue and digital voltage outputs. The analogue output is not reliable for synchronisation, however the digital output can be set up to toggle state when the stage passes a pre-set position in an array (known as position-synchronised output (PSO) mode). A schematic of how this works in practice is shown in figure 2.10.

The phase control signal requires precise reset positions to ensure the grating period is correct and a precise ramp rate to ensure the grating strength doesn't fluctuate. This is

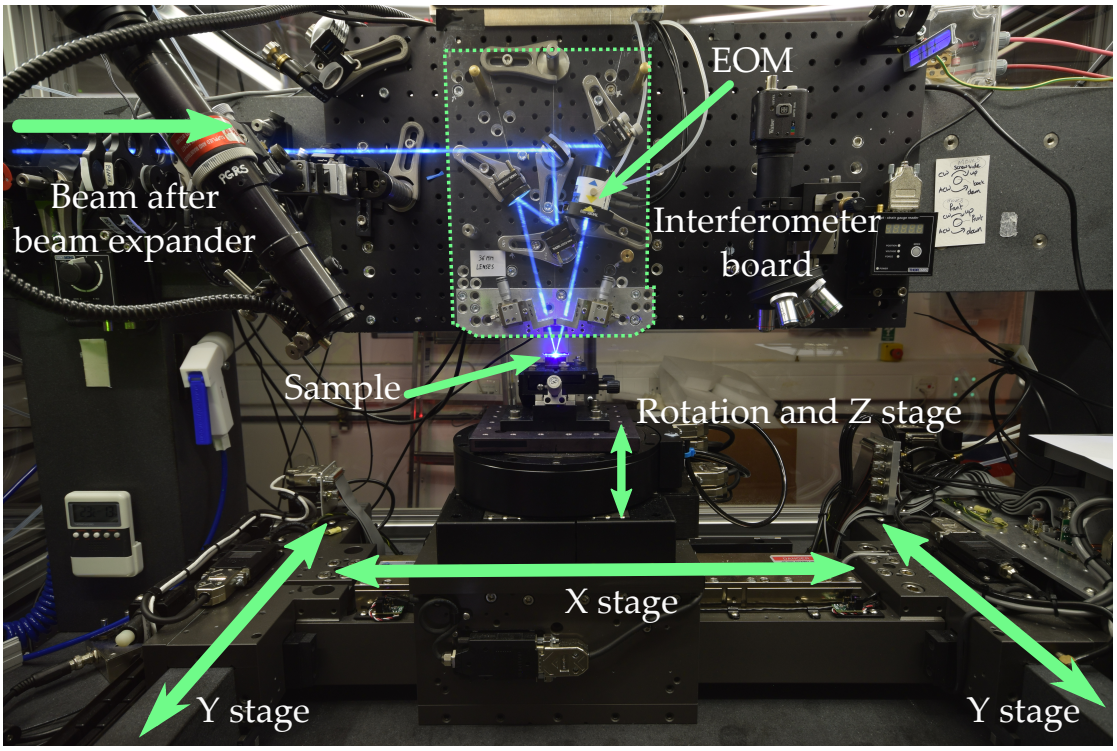

FIGURE 2.9: Aerotech stage system

PSO firing position array
0.5
0.6
1.1
1.2
1.7
1.8

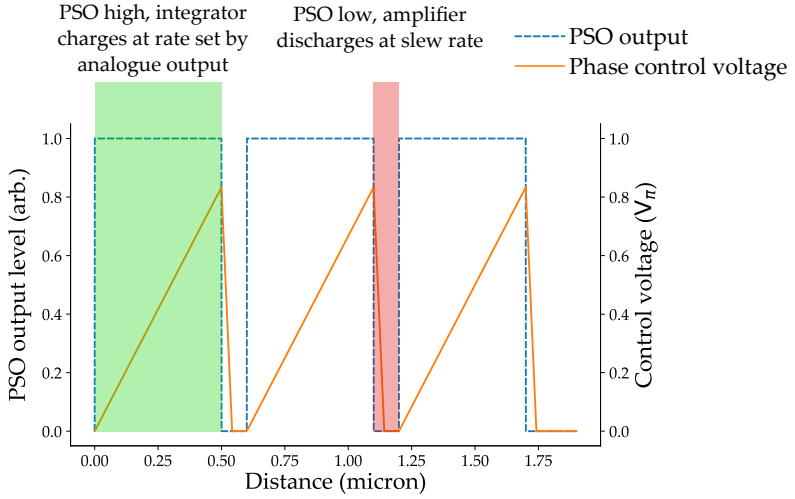

FIGURE 2.10: Conversion of firing positions phase control voltage for an 83% duty cycle uniform grating with a period of 0.6 µm. The PSO firing position array generates a digital voltage signal in distance. The op-amp integrator converts the digital signal to an analogue phase control signal which is used to drive the EOM.

implemented using the analogue and digital outputs from the stage system, along with an op-amp integrator circuit (as shown in figure 2.11). The analogue output from the stages is used to drive the input of the integrator, resulting in a voltage which increases at a constant rate. The PSO signal is used to control the integrator reset. The positions which make up the PSO array (known as 'firing positions') specify the grating period and duty cycle. When the digital output from the PSO is held low, the integrator charges

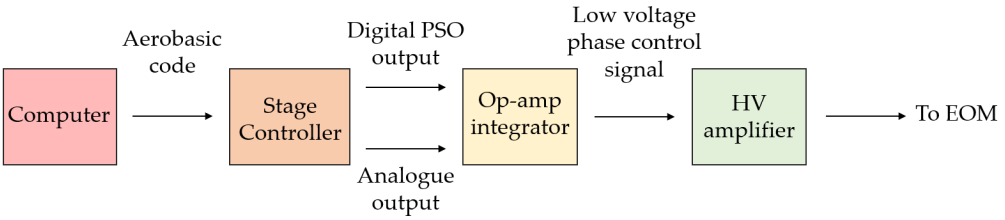

FIGURE 2.11: Implementation of phase control voltage scheme

and the fringes are moved relative to the sample, resulting in grating writing. When the integrator is toggled from low to high the integrator signal quickly drops to 0 V. The high voltage output which drives the EOM follows slightly later (limited by the slew rate of the amplifier). This constitutes the reset part of the signal. If the digital output is held high for longer than it takes to reset the EOM driving voltage to zero then the interference fringes are held stationary with respect to the sample, resulting in 'blurring' and a reduction in the strength of the grating. In Aerobasic programming these firing positions must be explicitly calculated (or loaded from file) for each specific device. An alternative scheme is presented in chapter 6 where the user defines the duty cycle and period over the grating using functions and the the firing positions are calculated automatically using a C++ library.

2.5 Conclusions

A broad background of the fabrication platform used to create devices within this thesis was presented. Photosensitivity of FHD silica was discussed and methods of increasing the photosensitive response were described. The ssDUW scheme was introduced; this enables fabrication of a wide range of waveguide and grating devices using software control. The scheme has great flexibility in device apodisation and period via manipulation of the EOM phase control signal. Limits on period detuning were discussed, this effect is apparent in chapter 5 when highly-chirped Bragg gratings are fabricated. Later devices in this thesis replaced Aerobasic code with a high-level C++ library to generate firing positions and motion commands (including rotations) with coordinate transformations. More information about this can be found in chapter 6.

2.6 References

[1] S. P. Watts, "Flame hydrolysis deposition of photosensitive silicate layers suitable for the definition of waveguideing structures through direct ultraviolet writing," Ph.D. dissertation, 2002.

[2] R. Brückner, "Properties and structure of vitreous silica. I," *Journal of Non-Crystalline Solids*, vol. 5, no. 2, pp. 123–175, 1970.

[3] A. J. Mclaughlin, "Hybrid silicon optoelectronic technologies," Ph.D. dissertation, 1998.

[4] D. L. Williams, B. J. Ainslie, J. R. Armitage, R. Kashyap, and R. Campbell, "Enhanced UV photosensitivity in boron codoped germanosilicate fibres," *Electronics Letters*, vol. 29, no. 1, pp. 45–47, 1993.

[5] J. Canning, "Fibre gratings and devices for sensors and lasers," *Laser and Photonics Reviews*, vol. 2, no. 4, pp. 275–289, 2008.

[6] L. Skuja, "Optically active oxygen-deficiency-related centers in amorphous silicon dioxide," *Journal of Non-Crystalline Solids*, vol. 239, no. 1-3, pp. 16–48, 1998.

[7] D. C. Hutchings, M. Sheik-Bahae, D. J. Hagan, and E. W. Van Stryland, "Kramers-Kronig relations in nonlinear optics," *Optical and Quantum Electronics*, vol. 24, no. 1, pp. 1–30, 1992.

[8] L. Skuja, H. Hosono, and M. Hirano, "Laser-induced color centers in silica," in *Proceedins of SPIE*, International Society for Optics and Photonics, vol. 4347, SPIE, 2001, pp. 155–168.

[9] J. Stone, "Interactions Of hydrogen and deuterium with silica optical fibers - a review," *Journal of Lightwave Technology*, vol. LT-5, no. 5, pp. 712–733, 1987.

[10] R. Bannerman, "Microfabrication of waveguide devices for quantum optics," Ph.D. dissertation, 2019.

[11] M. Fokine and W. Margulis, "Large increase in photosensitivity through massive hydroxyl formation," *Optics Letters*, vol. 25, no. 5, pp. 302–304, 2000.

[12] A. Jantzen, "The design, fabrication and development of micromechanical integrated optical pressure sensors for aerospace," Ph.D. dissertation, 2019.

[13] C. Holmes, "Direct UV written planar devices for sensing and telecommunication applications," Ph.D. dissertation, 2009.

[14] P. C. Gow, R. Bannerman, J. Gates, P. Mennea, C. Holmes, A. Jantzen, and P. G. Smith, "Integrated waveguides and Bragg gratings UV written with 213nm light," in *2019 Conference on Lasers and Electro-Optics Europe and European Quantum Electronics Conference*, 2019.

[15] M. Douay, W. X. Xie, T. Taunay, P. Bernage, P. Niay, P. Cordier, B. Poumellec, L. Dong, J. F. Bayon, H. Poignant, and E. Delevaque, "Densification involved in the UV-based photosensitivity of silica glasses and optical fibers," *Journal of Lightwave Technology*, vol. 15, no. 8, pp. 1329–1342, 1997.

[16] F. Knappe, "Waveguide structuring and Bragg grating fabrication by ultraviolet light induced refractive index changes in photosensitive optical materials," Ph.D. dissertation, 2007.

[17] "Bragg gratings fabricated in monomode photosensitive optical fiber by UV exposure through a phase mask," *Applied Physics Letters*, vol. 62, no. 10, pp. 1035–1037, 1993.

[18] I. Peterman, B. Sahlgren, S. Helmfrid, A. T. Friberg, and P. Fonjallaz, "Fabrication of advanced fiber Bragg gratings by use of sequential writing with a continuous-wave ultraviolet laser source," *Applied Optics*, vol. 41, no. 6, pp. 1051–1056, 2002.

[19] M. Gagné, L. Bojor, R. Maciejko, and R. Kashyap, "Novel long fiber Bragg grating fabrication technique based on push-pull phase-shifting interferometry," *Optics Express*, vol. 16, no. 26, pp. 21 550–21 557, 2008.

[20] H. Deyerl, N. Plougmann, J. B. Jensen, F. Floreani, H. R. Sørensen, and M. Kristensen, "Fabrication of advanced Bragg gratings with complex apodization profiles by use of the polarization control method," *Applied Optics*, vol. 43, no. 17, pp. 3513–3522, 2004.

[21] D. Stepanov and M. Sceats, "Controlled phase delta between beams for writing Bragg gratings," European pat. 1 082 627, 1999.

[22] C. Sima, "Integrated planar Bragg grating devices for advanced optical communication systems," Ph.D. dissertation, 2013.

[23] D. H. Smith, R. H. S. Bannerman, and J. C. Gates, "Direct UV writing of grating structures," *Article in preparation*,

Chapter 3

Bragg Gratings and Planar Waveguide Development

Due to work in the research group spanning over 20 years, we are able to fabricate devices with somewhat arbitrary Bragg gratings over a large spectral range. The wide spectral range allows us to discern how waveguide properties change with position by spectral characterisation. Software control of the system, rather than being limited to phasemasks, enables fast iteration of new device designs. When investigating a large parameter space (such as the UV written FHD platform provides) it is important that characterisation methods provide as much information as possible to quickly optimise devices. An example of this process is given in the later half of the chapter when developing a new wafer and waveguide recipe. Spectrometer devices operating around the 780 nm wavelength band (to exploit silicon detectors) required development of non-standard wafers which support a strong planar waveguide mode, in addition to a channel waveguide. This required modelling and full experimental characterisation to verify device operation.

The chapter starts with a summary of waveguide theory and description of waveguide modes. Next it describes Bragg grating theory using both a Fourier transform method and full coupled mode theory. It then describes typical characterisation methods for gratings. Finally modelling and experimental results are presented for the wafers used to make the devices described in chapter 6.

FHD layers discussed in this chapter were fabricated by Rod Cecil, James Gates and Paolo Mennea. Mode modelling and grating modelling were performed in conjunction with Rex Bannerman and Paolo Mennea. Waveguide fabrication, characterisation and analysis were solely my own work.

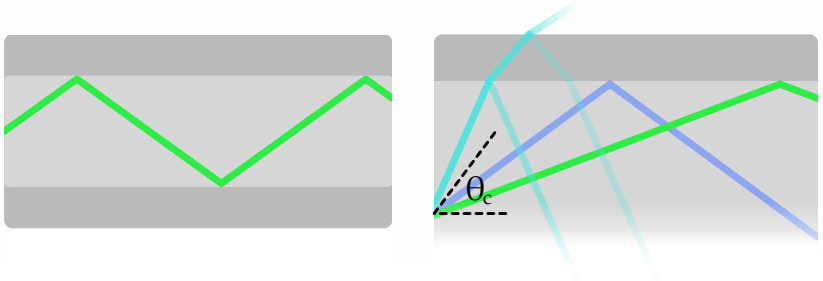

FIGURE 3.1: A simple reflection waveguide. Light propagating at an angle smaller than the critical angle will be trapped by total internal reflection. Light travelling at an angle greater than the critical angle will partially escape the waveguide.

3.1 Waveguide theory

Optical waveguides have a structured refractive index which guides light, much like pipes guide the flow of liquid. Analytical analyses of optical waveguides are complex, however we can consider a simple waveguide geometry and infer some more complex properties from it.

A basic waveguide can be created with a strip of high index core surrounded by a lower index cladding as shown in figure 3.1. Rays hitting the high to low refractive index boundary will experience total internal reflection provided the angle at which they strike the surface is below the critical angle given by Snell's law:

$$\theta_c = \arcsin \frac{n_{\mathrm{cl}}}{n_{\mathrm{co}}}, \tag{3.1}$$

where n_{cl} and n_{co} are the refractive indices of the waveguide cladding and core respectively. Such a reflection based waveguide should confine rays forever. Typical optical fibres have a small core radius ($\sim$10 µm) and are designed to operate with NIR light with a wavelength $\sim$1.5 µm so rays would diffract within a few microns. In actuality the waveguide shapes the phasefront of the light to counteract diffraction. We can derive this effect, following the approach shown by Okamoto [1]. Maxwell's equations in a material are

$$\nabla \times \mathbf{E} = -\mu_0 \frac{\partial \mathbf{H}}{\partial t}, \tag{3.2}$$

$$\nabla \times \mathbf{H} = \epsilon_0 n^2 \frac{\partial \mathbf{E}}{\partial t}, \tag{3.3}$$

where $\mathbf{E}$ is the vector electric field, $\mathbf{H}$ is the magnetic auxiliary field, μ_0 and ϵ_0 are respectively the permeability and permittivity of free space, n is the refractive index of the material, and t is time. These, when combined with general plane wave solutions

$$\mathbf{E} = \mathbf{E_0}(x, y) \exp\{[\mathrm{i}(\omega t - \beta z)]\}, \tag{3.4}$$

$$\mathbf{H} = \mathbf{H_0}(x, y) \exp\{[\mathrm{i}(\omega t - \beta z)]\}, \tag{3.5}$$

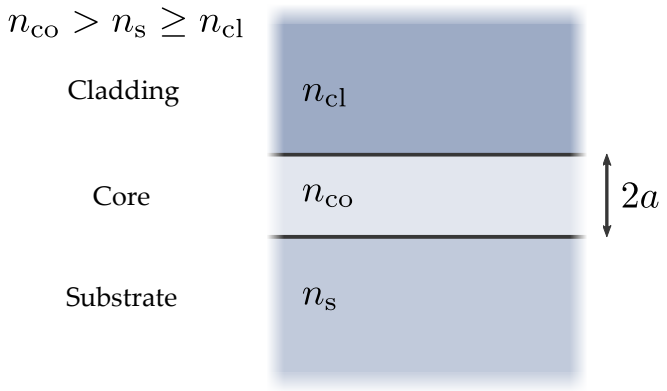

FIGURE 3.2: 1-D step index waveguide geometry. The slab is infinitely wide, cladding and substrate are both infinitely thick.

where x and y are coordinates perpendicular to the direction of propagation, z is the coordinate along the propagation axis, ω is the angular frequency of the wave, and β is a general propagation constant. Such plane wave solutions can be used to derive wave equations, however these equations are difficult to solve analytically unless symmetry conditions are used. General solutions to waveguides are normally modelled using finite-element method (FEM) or finite-difference method (FDM) simulations using proprietary software packages (FIMMWAVE, COMSOL Multiphysics etc.).

The 1-D step index waveguideshown in figure 3.2 offers a lot of insight into general waveguide properties and is useful to illustrate concepts that are complex to visualise in higher dimensional cases. The step index waveguide here contains 3 layers, a low refractive index cladding, a high refractive index core and a substrate with refractive index between that of the core and cladding. Indices are denoted by n_{co}, n_{cl} and n_s for core, cladding and substrate respectively. The cladding and substrate are assumed to be infinitely thick (in practice this requires layers be significantly thick that evanescent waves are highly attenuated). Symmetry conditions allow two independent sets of equations to be constructed:

$$\begin{aligned} \frac{\partial^2 E_y}{\partial x^2} + (k^2 n^2 - \beta^2) E_y &= 0, \\ -\frac{\beta E_y}{\mu_0 \omega} &= H_x, \\ \frac{\partial E_y}{\partial x} &= -\mathrm{i}\mu_0 \omega H_z, \\ E_x = E_z &= H_y = 0, \end{aligned} \tag{3.6}$$

$$\begin{aligned} \frac{\partial}{\partial x}\left(\frac{1}{n^2}\frac{\partial H_y}{\partial x}\right) + (k^2n^2 - \beta^2)H_y = 0, \\ \frac{\beta H_y}{\epsilon_0 n^2 \omega} = E_x, \\ \frac{\partial H_y}{\partial x} = -\mathrm{i}\epsilon n^2 \omega E_z, \\ H_x = H_z = E_y = 0, \end{aligned} \tag{3.7}$$

where x, y and z subscripts describe a component of the vector quantity and k is the wavevector. The first set of equations (3.6) describes a mode with transverse electric field, but with a non-zero component of H_z, so are referred to as the transverse electric (TE) modes. Conversely 3.7 has a non-zero E_z and a purely transverse **H** field, so are referred to as the transverse magnetic (TM) modes.

Using a suitable ansatz (see [1] for more details) results in a dispersion equation that can be solved to calculate waveguide mode properties:

$$2v\sqrt{1-b} = m\pi + \arctan\sqrt{\frac{b}{1-b}} + \arctan\sqrt{\frac{b+\gamma}{1-b}}, \tag{3.8}$$

$$2v\sqrt{1-b} = m\pi + \arctan\frac{n_{\mathrm{co}}^2}{n_{\mathrm{s}}^2}\sqrt{\frac{b}{1-b}} + \arctan\frac{n_{\mathrm{co}}^2}{n_{\mathrm{cl}}^2}\sqrt{\frac{b+\gamma}{1-b}}, \tag{3.9}$$

for TE and TM modes respectively. b is the normalised propagation constant, v is the normalised frequency and γ is the asymmetry parameter:

$$b = \frac{n_{\mathrm{eff}}^2 - n_{\mathrm{s}}^2}{n_{\mathrm{co}}^2 - n_{\mathrm{s}}^2}, \tag{3.10}$$

$$v = ka\sqrt{n_{\mathrm{co}}^2 - n_{\mathrm{s}}^2}, \tag{3.11}$$

$$\gamma = \frac{k^2n_{\mathrm{s}}^2 - k^2n_{\mathrm{cl}}^2}{k^2n_{\mathrm{co}}^2 - k^2n_{\mathrm{s}}^2}, \tag{3.12}$$

$$0 < \gamma, b < 1,$$

n_{eff} is the effective mode index and a is half the height of the core region. Solutions of equation 3.8 and equation 3.9 have been calculated for a slab waveguide to show some basic mode properties (figure 3.3). This shows that modes appear at some cutoff wavelength with a low propagation constant ($n_{\mathrm{eff}} \approx n_{\mathrm{s}}$) and more modes are supported as the wavelength decreases (v increases). TM modes have a slightly lower mode index at the same wavelength (for 1D slabs); differences between TE and TM modes diminish as the asymmetry decreases. For simple slab waveguides the mode number also describes the number of lobes present in the mode.

Much of this can be applied to the theory of 2D waveguides. There exist a set of TE_{ij} and TM_{ij} modes, where i and j refer to the order of the waveguide in the x and y

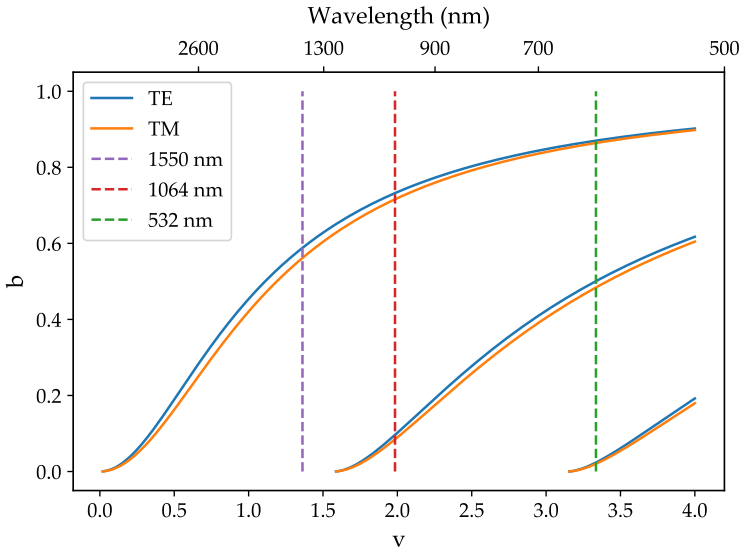

FIGURE 3.3: v-b diagram for a 1D slab waveguide with $n_{co} = 1.48$, $n_{cl} = n_s = 1.40$ and $a = 0.7\,\mu m$. From left to right are the 0^{th}, 1^{st} and 2^{nd} order modes with $m = 0$, 1 and 2 respectively. Solutions calculated by using the Newton-Raphson method to solve roots of eqns. 3.8, 3.9

dimension respectively. Higher ordered modes also have larger numbers of lobes, similar to the 1D case.

Waveguides operating with multiple modes with different refractive indices are not ideal when working with Bragg gratings; the different mode index shifts the spectral fingerprint of each grating and coupling between different modes makes the strength of the grating difficult to characterise. Instead waveguides for Bragg gratings are often designed to support a single set of TE and TM modes. As mentioned earlier TE and TM modes often have very similar mode indices, however they are perpendicular to each other so can be separated using polarisation. Therefore we are primarily concerned with engineering the refractive index and spatial properties such that higher order modes are not supported.

3.2 Bragg grating theory

Bragg gratings are a periodic refractive index variation inside a waveguide. They are diffraction gratings, however due to momentum conservation constraints on the angle of the grating planes diffraction is limited to lie along the waveguide axis. Bragg gratings are typically used as spectral filters. Each grating plane is a weak reflector, contributions from each grating plane build up over the length of the grating. If a wavelength of light is phasematched to the grating then these reflections add in phase and get stronger, if it is not phasematched then they add with different phases and have a negligible sum.

The phasematching condition can be calculated by considering a bulk diffraction grating with and input angle of 0° and an output angle of 180°, and results in peak reflectivity at a Bragg wavelength, λ_B, described by

$$\lambda_B = 2n_{\text{eff}}\delta, \tag{3.13}$$

where δ is the period of the refractive index variation. To calculate the spectral response of the grating we must consider the phase and reflectance profile of the grating, something which will be assessed in more detail in the following sections.

3.2.1 Coupled mode theory

Coupled mode theory is the most commonly used approach to calculate the reflectivity (among other properties) of Bragg gratings. Erdogan showed many different properties of Bragg grating spectra using coupled mode theory, however the approach shown in his 1998 review [2] is aimed predominantly at Bragg gratings fabricated inside optical fibre. In fibre grating fabrication the grating is a perturbation to the refractive index of an existing waveguide. Erdogan considers a refractive index variation to have an AC and a DC component, both of which perturb existing waveguide modes to allow the forward propagating mode to couple power into the corresponding backward propagating mode. In the case of small-spot direct UV written waveguides and Bragg gratings the waveguides and gratings are fabricated in a single-step process. Both the AC and DC refractive index changes ($\sim 1 \times 10^{-4}$) are small when compared to the index of the material used to create the waveguide (~ 1.45), however we cannot consider the index change using perturbation theory as no modes exist before the index change occurs. Instead we can consider the unperturbed system to be the structure with the refractive DC index change and the AC refractive index change as a perturbation. The net result of this is a small change in the definitions of terms compared to the Erdogan case, but the same functional form. A full derivation can be found in [3].

We can use this to provide an analytic solution for the reflectivity of a uniform grating with constant period for arbitrary grating strengths. As discussed in Erdogan's review the reflectivity of a Gaussian grating with arbitrary strength may be calculated using a contraction of many transfer matrices. Such an approach is more complex to fit to experimental data. Instead coupled mode theory was restricted to analysis of uniform gratings, where parameters can be extracted by a simple fitting routine over a single analytic function.

The reflectivity of a uniform grating is given by [3]:

$$r = \frac{\sinh^2\left(\sqrt{\kappa^2 - \psi^2}L_g\right)}{\left(\cosh^2\sqrt{\kappa^2 - \psi^2}L_g\right) - \frac{\psi^2}{\kappa^2}}, \tag{3.14}$$

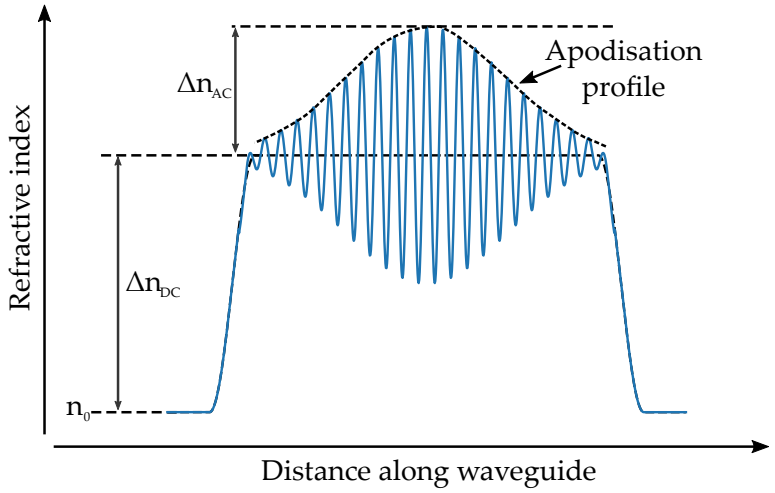

FIGURE 3.4: Schematic of refractive index modulation in ssDUW waveguides and gratings. Before writing the glass has a refractive index of n_0. ssDUW induces an AC and DC refractive index modulation. The DC component creates a waveguide and is typically constant across a waveguide. The AC refractive index modulation is controlled by the EOM phase control system and defines the apodisation across the grating.

Where L_g is the grating length, ψ is the phase mismatch,

$$\psi = 2\pi n_{\text{eff}} \left(\frac{1}{\lambda} - \frac{1}{\lambda_D} \right), \tag{3.15}$$

λ_D is the design Bragg wavelength of the grating and κ is the AC coupling coefficient,

$$\kappa = \frac{\pi}{\lambda} \Delta n_{\text{AC}}, \tag{3.16}$$

where Δn_{AC} is the AC refractive index modulation, defined in figure 3.4. This form of the grating reflectivity assumes unit input power to the grating so when considering waveguides with losses a multiplicative amplitude term must be added. For weak gratings, $\kappa L_g \ll 1$, the reflectivity of a uniform grating is approximately a sinc^2 profile. Above this limit gratings begin to saturate: the bandwidth increases and the grating becomes 'flat-topped', as shown in figure 3.5. Strong gratings and coupled mode theory are often used to analyse the refractive index modulation inside waveguides. In weak gratings waveguide loss is indistinguishable from changes in the index modulation, however in stronger gratings the index modulation also changes the width of the grating as well as the height (the refractive index modulation can be extracted from how 'flat-topped' the grating is).

Coupled mode theory provides an analytic solution to the reflectivity of gratings, however it can be cumbersome to work with for apodised gratings. Instead we often consider the weak grating limit.

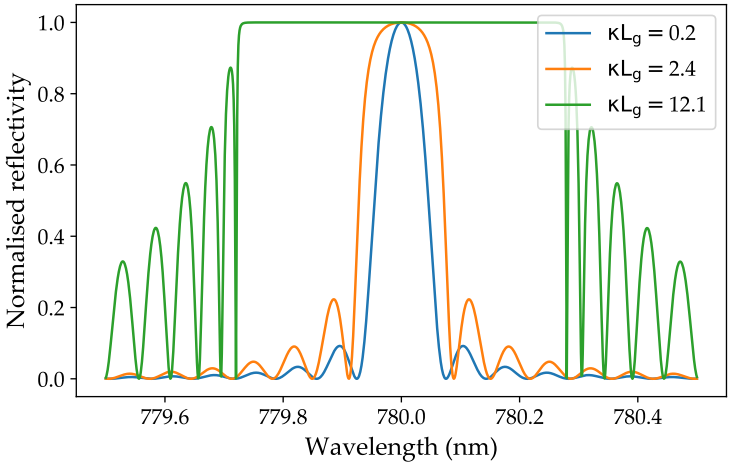

FIGURE 3.5: Plot of uniform Bragg grating reflectivity modelled with coupled mode theory. As κL_g exceeds 1 the reflectivities start to flatten and deviate from a sinc^2 profile.

3.2.2 Weak gratings

Weak gratings ($\kappa L_G \ll 1$) are often used to characterise devices, as they typically have narrow spectral features and minimal excess loss to cladding modes. In such a limit we can make a number of approximations. Firstly the reflectivity per unit length inside the grating is low enough that light inside the grating will experience (at most) a single reflection, therefore we can ignore cavity effects. In addition the total reflectivity over the whole length of the grating is low enough that we can make the non-depleted pump approximation: the power inside the grating does not diminish significantly along its length.

Under these approximations the reflection spectrum of the grating can be calculated from the Fourier transform of the grating apodisation [4]. A demonstration of the equivalence of the Fourier transform solution and coupled mode theory is shown in figure 3.6. The Fourier transform relationship is much more intuitive than the cumbersome form of the reflectivity from coupled mode theory, in addition it provides a simple solution for the reflection spectra of gratings with arbitrary apodisation. Weak Gaussian gratings are typically used for loss measurements, as they provide smooth features which result in more stable fits than strong gratings or uniform gratings.

3.3 Waveguide characterisation

The FHD and UV writing processes have many free parameters (see section 2.2); as such it is necessary to characterise wafers and waveguides after every fabrication run to optimise devices. A set of test waveguides are written at different UV laser fluences to

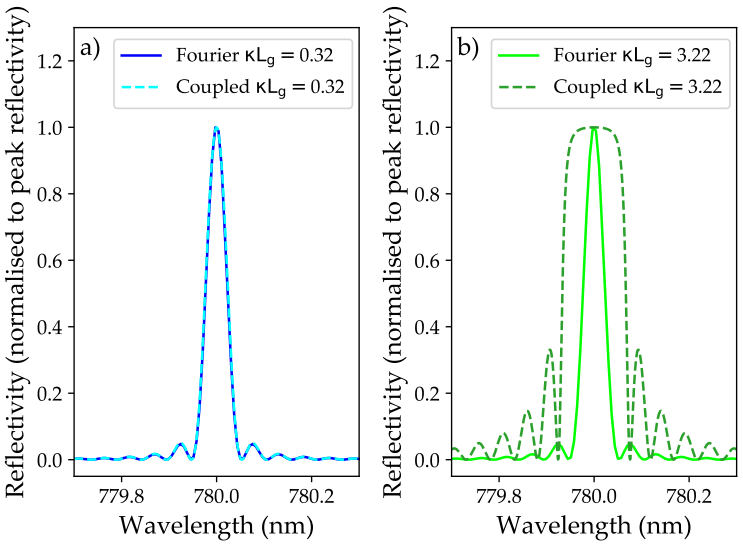

FIGURE 3.6: Comparison of grating reflection spectra calculated using coupled mode theory and Fourier transforms. a) The reflection spectra for weak gratings ($\kappa L_g \ll 1$) is approximated by the Fourier transform of the apodisation as shown in [4]. b) For gratings with coupling coefficient stronger than this limit the Fourier transform relation yields incorrect results and full coupled mode theory must be used.

examine the waveguide mode and grating properties as a function of refractive index. We can characterise the waveguide mode of these 'fluence test' devices by imaging the output mode (mode profiling) and we can infer further properties (n_{eff}, loss, nonuniformity, etc.) using the spectral response of Bragg gratings fabricated inside the devices. This section describes the different optical setups and procedures for measuring devices with both these approaches.

3.3.1 Mode profiling

Mode profiling interrogates the mode properties of a waveguide by imaging its modes. The system used in this thesis was originally built by Rex Bannerman, however it was modified and recalibrated by myself to support interchangeable lenses with different focal lengths. Light is coupled into a waveguide and the output mode is imaged using an InGaAs camera (Raptor Photonics OWL1.7-VS-CL-640) and telescope system as shown in figure 3.7. The camera is mounted on a motorised translation stage along the direction of propagation; the NA and mode diameter of the waveguide can be calculated by imaging the mode at different distances away from the waveguide and following the procedure laid out in [5], [6].

The mode profiling system enabled past measurements of the mode overlap of ssDUW FHD waveguides with SMF-28 fibre. These measurements were used as a basis for optimisation of the UV writing beam properties, resulting in waveguides with 0.3 dB coupling loss to optical fibre at 780 nm [7]. The mode profiling system is also useful in

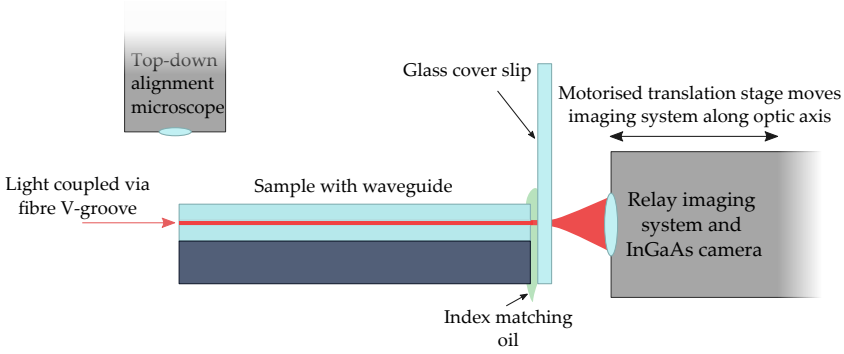

FIGURE 3.7: Mode profiling setup

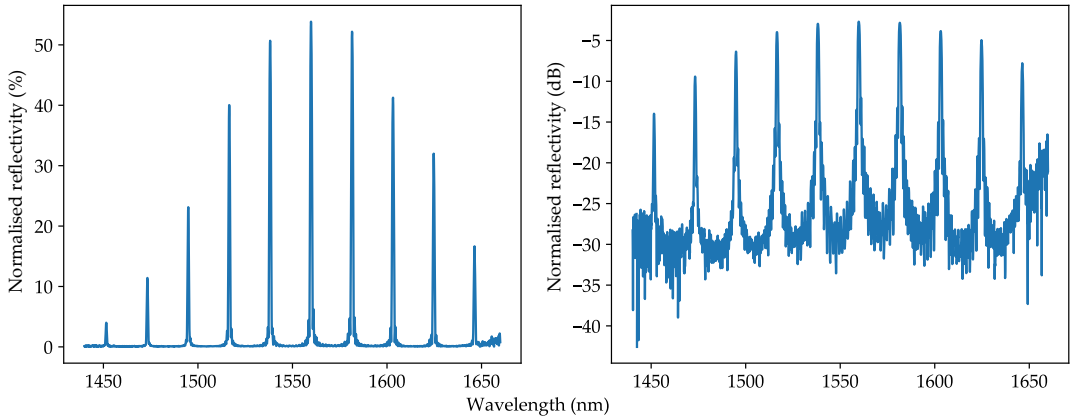

FIGURE 3.8: Typical reflection spectrum of ssDUW waveguide with Bragg gratings. The variation in grating reflection with wavelength is due to the grating detuning curve. Data courtesy of Qazi Salman Ahmed.

multi-mode waveguides; while Bragg gratings can reveal that a waveguide is multi-mode an image of the output of a waveguide can show if a waveguide is multi-mode vertically or horizontally. This is an important qualitative measurement for refining recipes to produce single-mode waveguides.

3.3.2 Grating characterisation

Bragg gratings can be used to spectrally interrogate the modal properties of waveguides. The spectra of a grating depends on its mode index, so a single input signal through a waveguide with multiple modes results in many overlapping spectral reflectance peaks. These can be quickly characterised using a wideband source and an optical spectrum analyser (OSA). By fabricating a number of gratings in different positions with different Bragg wavelengths it is also possible to spatially discriminate waveguide properties by analysing Bragg gratings spectrally. The wide grating detuning bandwidth achievable with the ssDUW system allows many Bragg gratings to be spectrally multiplexed within the same waveguide, as shown in figure 3.8. By randomising the order of grating Bragg wavelength correlations between grating wavelength and position are removed, allowing

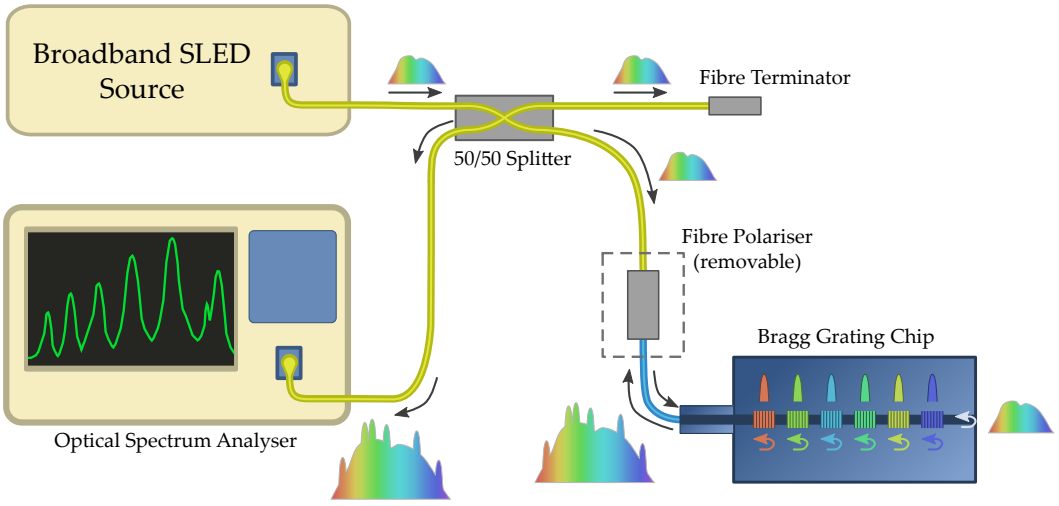

FIGURE 3.9: Grating characterisation setup. A wideband source is coupled into a device through a 50/50 splitter and a polariser. Gratings reflect narrow spectral bands and the facet at the end of the chip acts as a 3.3 % broadband Fresnel reflector. The signal due to the gratings can be measured on the OSA.

discrimination of changes in waveguide properties due to intrinsic loss, poor alignment and hydrogen outgassing.

Gratings are typically measured in reflection. This method allows gratings to be characterised, as shown in figure 3.9, with alignment to one side of the chip; not only is this easier than aligning transmission measurements, but it allows the output mode to be imaged while taking measurements to gather data for mode profiling measurements. The reflection method can also be used to characterise loss, provided the waveguides can be accessed from both ends of the chip. Rogers et al. [8] showed that by coupling into the chip from different ends and looking at the ratios of grating reflectivity the waveguide loss can be extracted without knowledge of the coupling loss to the chip from either end.

Light is coupled into chips using a fibre V-groove, which is aligned using visible light, as shown in figure 3.10. After alignment devices are interrogated using a broadband (typically unpolarised) source; a fibre polariser is used to selectively couple into TE/TM modes. The polariser is single mode (SM) input and polarisation maintaining (PM) output with polarisation axis of the polariser aligned to the PM fibre axis. The losses of the characterisation system are difficult to measure directly, so a broadband reflection spectrum of the source is estimated by disconnecting the fibre V-groove and using the bare ferrule of the FCPC connector as a 3.3 % Fresnel reflector. This estimated source spectrum can be used to create an estimate of the normalised relative reflection spectrum (typically referred to simply as the normalised reflection spectrum) by dividing the measured reflection spectrum by the input source estimated from a 3.3 % backreflection.

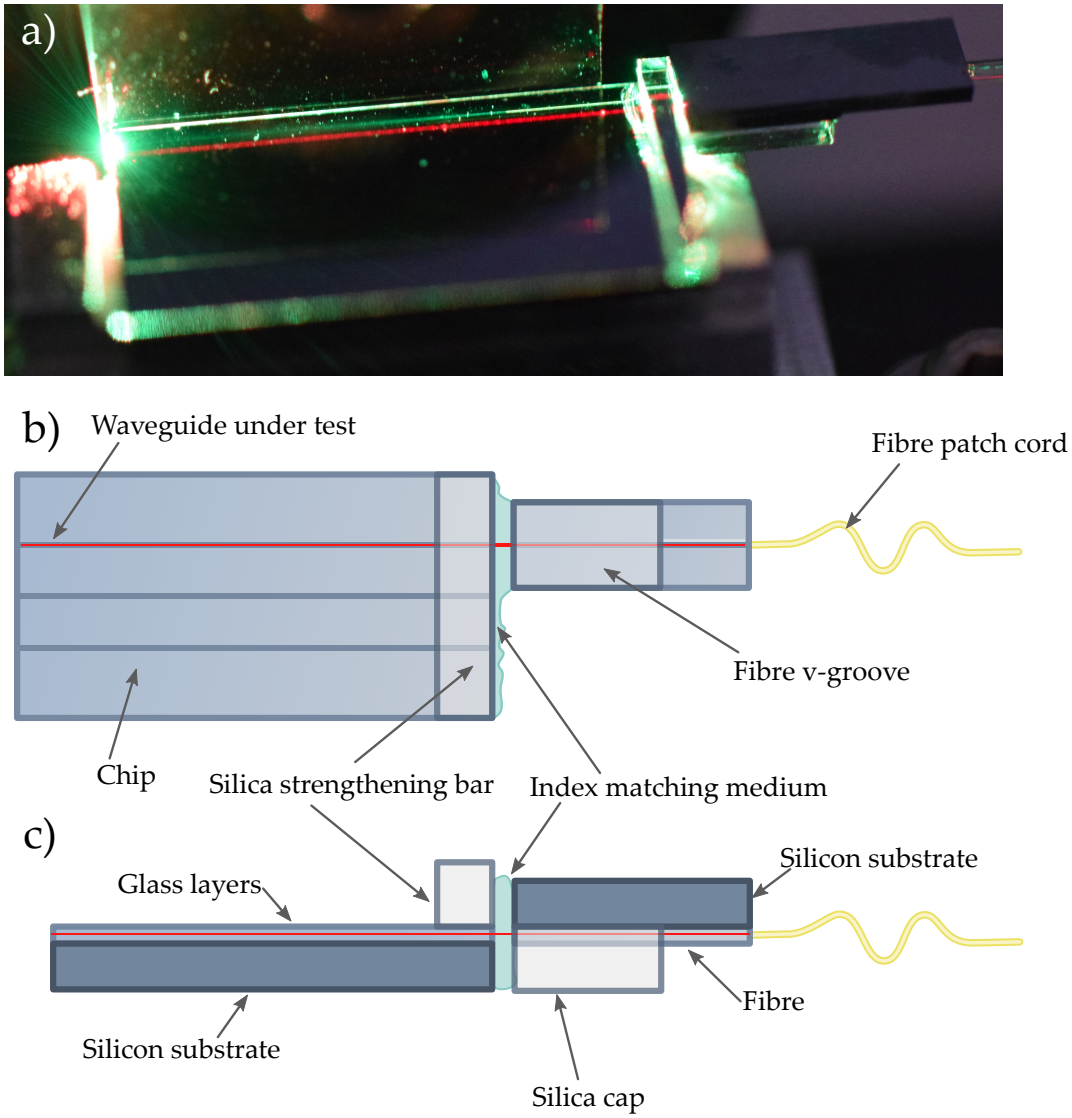

FIGURE 3.10: Light is coupled into waveguide devices using a fibre V-groove. In most characterisation index matching oil or gel is used as a medium between the device and V-groove, however some devices are permanently attached using UV-cured glue. In these cases the pigtail is flipped to aid the curing process and a silica strengthening bar is glued to the top of the chip to increase robustness of the glue joint.

3.3.3 Grating fitting

Reflection signals from Bragg gratings are complex. In an ideal situation gratings can be considered as separate peaks, however manual identification of peaks takes a lot of time; fluence test chips can often have hundreds of gratings and noise in data can often make manual identification difficult. Another problem is grating overlap. Gratings should be as closely spectrally spaced as possible to generate as many distinct data points over the limited writing bandwidth as possible. The spectral width of gratings is dependent on the refractive index modulation, which can vary due to alignment. As such it is difficult to ensure ahead of time that gratings will not spectrally overlap. To a

reasonable approximation we can consider grating reflectivities that overlap spectrally by summing the individual reflectivities of the gratings. Gratings used in characterisation are weak, so cavity effects are minimal and spectral overlap tends to occur near the band edges of the gratings. However to consider such an effect all gratings need to be fitted simultaneously rather than optimising each grating separately. This is further complicated by combining gratings of different apodisations in the same device. Uniform gratings are useful for identifying higher order modes and calculating refractive index modulation, whereas Gaussian gratings are useful for calculating waveguide loss. A fitting algorithm needs to be able to handle different types of grating spectral profile simultaneously.

To perform such a fit a good estimate of starting parameters is needed. Grating writing code logs information about every grating written in every waveguide in a machine readable format so fitting code has an estimate of where each grating peak should sit and the form of the intensity profile (sinc or Gaussian). Data is prepared for the fitting algorithm by normalising (dividing the linear signal by a 3.3 % reflection). A flat section of the spectrum is used to check for any remaining DC offset, such an offset is removed before performing fit optimisation.

Prepared data is lowpass filtered and a peak prominence algorithm [9] is used to find peaks given a minimum wavelength spacing between peaks. This same algorithm also provides initial estimates for the height, position and width of every peak. Log files are then used to assign the correct spectral shape to each peak based on fabricated periods and a refractive index estimate.

A function containing a term for each peak is constructed (see equation 3.17) and optimised simultaneously on prepared data (non-lowpass filtered) in the linear domain. The resulting grating data is plotted on top of the raw data for a comparison.

$$\begin{aligned} R(\lambda) &= \sum_{i}^{\text{Gratings}} f_i(\lambda), \\ f_i(\lambda) &= \begin{cases} A_i \,\text{sinc}^{\,2}\left(\frac{\lambda-\lambda_i}{w_i}\right) & \text{Uniform gratings,} \\ A_i \exp\left[\frac{(\lambda-\lambda_i)^2}{w_i^2}\right] & \text{Gaussian gratings,} \end{cases} \end{aligned} \tag{3.17}$$

where A_i is the maximum reflectivity of each grating, λ_i is the wavelength of the maximum reflectivity and w_i is the width of each spectral peak. This algorithm also calculates the effective index by comparing the fabricated grating period against the measured centre reflectance wavelengths.

3.4 780 nm wafer optimisation

Initial spectrometer devices (such as which will be shown in chapter 5) were all designed to operate at 1550 nm. Wafers with a weak planar waveguide resulting from design iterations of low-loss waveguides at 1550 nm were readily available, as well as sources and cameras. After the initial concept had been proven the next step was to work towards a prototype package with a detector attached to the chirped grating chip. 1550 nm detectors were found to be prohibitively expensive, however silicon detector arrays sensitive at 780 nm were much cheaper. This would however require development of a new FHD wafer recipe to support device operation at 780 nm.

A wafer recipe was designed by Paolo Mennea and fabricated by Rod Cecil, Paolo Mennea and James Gates. Pre-fabrication waveguide modelling (using FIMMWAVE) and grating modelling were performed by Paolo Mennea and Rex Bannerman. I performed all fabrication, characterisation and subsequent analysis of waveguides and Bragg gratings in this new wafer format.

3.4.1 Wafer Design

FHD fabrication is a complex process with a large parameter space. To save time and reduce design iterations new layer recipes tend to start from a known layer recipe. The thickness of each layer can be modified relatively easily by changing the number of passes the FHD torch makes over the rotating platen. Small perturbations can be made to the flow rates of process gasses to modify the refractive index of layers.

FHD wafers in Southampton are typically designed to be 'zero-delta'; before UV writing there should be no refractive index difference between the core, cladding and THOX layers. This produces a low-loss symmetric waveguide which can be optimised for fibre coupling. Wafers with a planar index contrast to support guided modes in-plane are highly non-standard. A wafer was designed by Paolo Mennea based on a layer produced during optimisation of zero-delta wafers at 1550 (known as layer PX113). The original PX113 core layer had a 0.22% percentage difference between core and THOX refractive indices and was 5.41 µm thick. FIMMWAVE modelling showed that the same refractive index contrast value with a 3.3 µm thickness would produce a single-mode channel waveguide at 780 nm(as shown in figures 3.12 e & f), as well as supporting planar waveguide modes (as shown in figure 3.13).

Two sets of core layers were deposited by Rod Cecil, PX193 and PX194, using 15 µm THOX wafers as a substrate. Both wafers were later clad using a standard cladding layer recipe. Refractive indicies and thicknesses of layers were measured using the Metricon system at a wavelength of 1550 nm. Refractive indicies were converted to 780 nm by assuming a linear dispersion model. Refractive index data for pure silica [10] and FHD

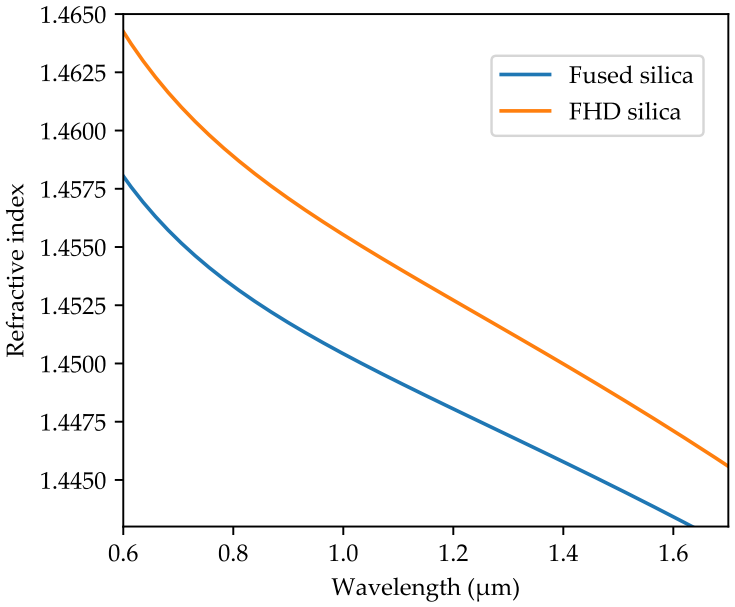

FIGURE 3.11: Dispersion in FHD doped silica glass [11] and pure silica [10]. Though the absolute refractive index is different the wavelength dispersion is very similar across the waveguide range shown, and is expected to be very close to the dispersion of the layers shown in this chapter.The linear dispersion was calculated to be $1.418 \times 10^{-5}\,\mathrm{nm}^{-1}$.

Layer	THOX	PX113	PX193	PX194	Clad
Thickness µm	15.00	5.41	3.27	3.31	>17.7
Refractive index (1550 nm)	1.4440	1.4483	1.4532	1.4510	1.4457
Refractive index (780 nm)	1.4537	1.4581	1.4630	1.4608	1.4555

TABLE 3.1: Layer parameters. The cladding layer was slightly nonuniform, with a minimum measured thickness of 17.7 µm. Cladding layer is thick enough that nonuniformity is not expected to perturb the guided mode.

doped layers [11] show that the linear dispersion in the 700 nm to 1600 nm region is relatively insensitive to glass composition (see figure 3.11); the same linear dispersion parameter can be used for core, cladding and THOX layers. The resulting parameters for all layers are summarised in table 3.1

PX193 and PX194 were fabricated using the the same parameters as the PX113 recipe, however with a modified boron flow rate. The nominal flow rate of BCl_3 in the PX113 recipe was 19 g/h, however an equipment failure during the fabrication run modified the flow rate of BCl_3 by an unknown amount. Values of 15 g/h and 20 g/h were respectively used for PX193 and PX194. The layer indices of PX193/PX194 were higher than PX113, meaning multi-mode waveguides are more likely (finite-difference time domain (FDTD) mode modelling for these layers si shown in figure 3.12). However the stronger planar waveguide should reduce propagation loss through the planar layer. As such the waveguides were still deemed worth investigating before further wafer iterations were created.

Both wafers were diced into $20 \times 10\,\mathrm{mm}^2$ chips which were loaded into the hydrogen

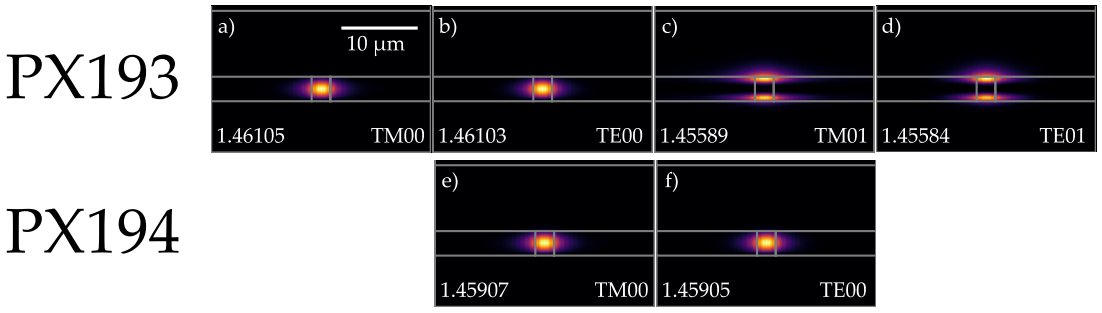

FIGURE 3.12: Normalised intensity of the guided modes at 780 nm calculated via FDTD modelling with an induced refractive index change of 1×10^{-3} for PX193 and PX194 ([a-d] and [e-h] respectively). PX194 is single mode, whereas PX193 supports a pair of modes with 2 vertical modes (due to the higher core index of PX193)

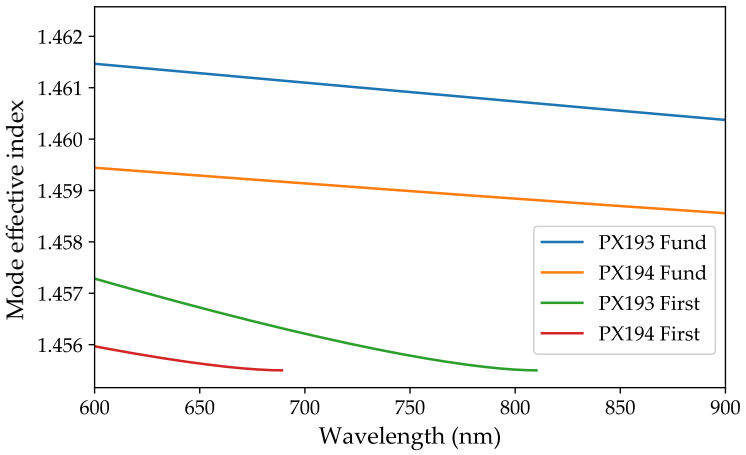

FIGURE 3.13: Dispersion curves for planar waveguide modes in PX194 and PX193 (modelled using equations 3.8 and 3.9), showing cutoff wavelengths for first order modes. At the design wavelength of 780 nm PX194 is single-mode, while PX193 supports 2 modes.

cell for at least a week before writing. Waveguides with sets of Bragg gratings were written into each chip for a range of fluences to establish waveguide properties with a range of refractive index contrasts. Waveguide fluences were written in a random order so hydrogen outgassing effects could be decoupled from any nonuniformites in the glass layer. Bragg wavelengths of gratings inside waveguides were similarly randomised to decouple cavity effects from the edge of the waveguide and lossy modes from grating detuning effects. Half of the waveguides in each chip (chosen randomly) were Gaussian apodised, the rest were uniform apodised.

Waveguide length	20 mm
Waveguide pitch	127 µm
Number of waveguides	16
Waveguide vertical offset	1 mm
Maximum fluence	30 kJ/cm^2
Minimum fluence	5 kJ/cm^2
Pre-fabrication n_{eff} estimate	1.445
Central grating Bragg wavelength	780 nm
Grating wavelength spacing	4 nm
Number of gratings	18
Grating length	0.8 mm
Grating peak duty cycle	70%
Grating to grating spacing	0.2 mm
Grating to facet spacing	1 mm

TABLE 3.2: Parameters for fluence test chips in PX193 and PX194.

3.4.2 Results and analysis

3.4.2.1 PX193

Waveguides and Bragg gratings were fabricated inside PX193, a selection of spectra from which can be seen in figure 3.14. The spectrum of the wideband source varied significantly over the experiment (it is likely that the source had not fully warmed up when the background signal was taken). This is the cause of the shift in the baseline shown in the logarithmic domain in figure 3.14. Though this shift appears dramatic, it is negligible in the linear domain, when grating fitting occurs.

This device was one of the first written using a C++ library developed as part of chapter 6 instead of AeroBasic. This greatly simplified the characterisation procedure; grating wavelengths and positions were written to a log file and could be directly interpreted via fitting code rather than having to be manually entered for each grating. Unfortunately the early version of the C++ library had a programming error affecting Gaussian apodised gratings, which caused significant amounts of high-frequency noise across the whole grating reflection spectrum and much weaker reflections than expected from Gaussian gratings. This programming error was corrected in subsequent devices.

The fine data (see figure 3.14c and figure 3.14d) shows that each grating has a number of side peaks (even at low fluences). These peaks are all at a lower wavelength than the primary peak, which indicate the presence of significant higher order modes.

At low fluences the gratings were relatively weak. When the refractive index contrast was increased to support stronger gratings the waveguide became multi-mode. Tests of loss within this device were inconclusive due to the poor quality of the Gaussian gratings and additional modes, however there was already enough information to deem the wafer

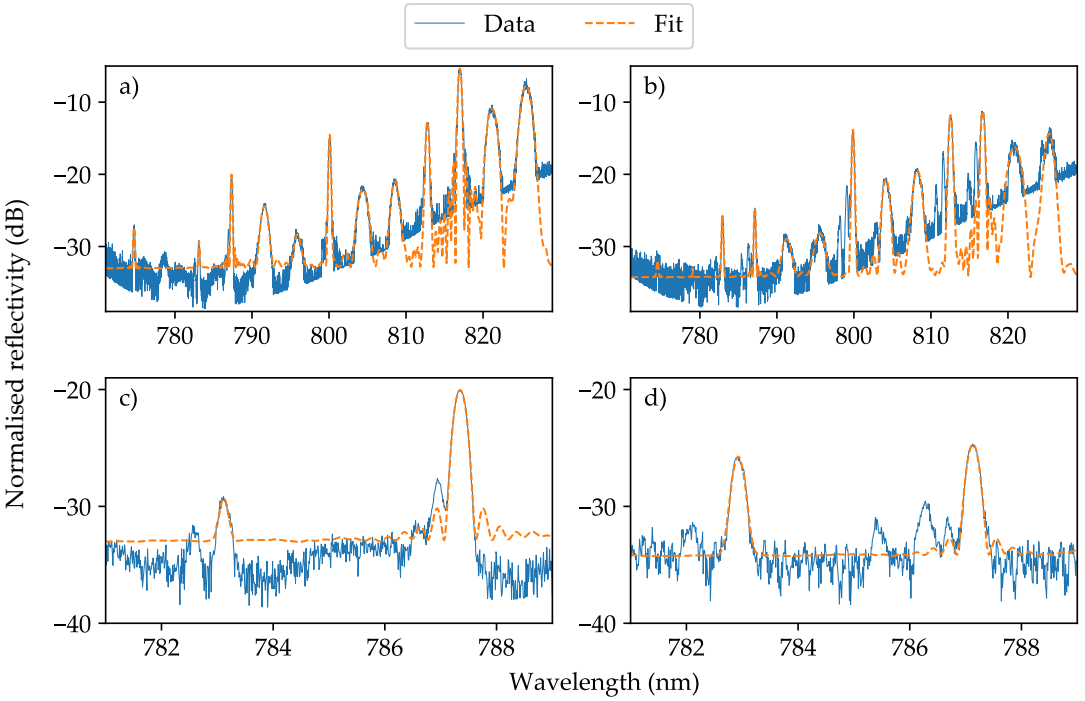

FIGURE 3.14: Bragg gratings in PX193. a&b) Broad spectrum of normalised reflectivity from gratings in PX193 for fluences of 5 kJ/cm^2 and 15 kJ/cm^2 respectively. c&d) Narrow spectrum of gratings 3&4 from for fluences of 5 kJ/cm^2 and 15 kJ/cm^2 respectively showing fine detail.

unsuitable for Bragg grating spectrometer fabrication. Bragg grating spectrometers require single mode waveguides. Multiple modes with different effective mode indices cause a single wavelength to have multiple intensity peaks at different positions along the detector. It is likely this would narrow the usable bandwidth of the device by introducing a FSR, or reduce the resolution by blurring multiple intensity peaks from different modes together (depending on the effective index separation).

3.4.2.2 PX194

A device was made in PX194 following the values in table 3.2, however the gratings were much stronger and saturated. The aforementioned code issue affecting Gaussian gratings had also been corrected. A second device was used to collect the majority of results, with the grating duty cycle reduced to 50 % and the length of Gaussian gratings reduced to 0.5 mm. Characterisation of the initial device suggested that the fluence range investigated could be narrowed to 6 kJ/cm^2 to 15 kJ/cm^2. Not all gratings present in the device could be analysed; gratings designed at 743.5 nm and 747.7 nm fell below the noise floor of the characterisation system.

Gratings in PX194 had a much cleaner spectral profile than those in PX193 and were much stronger even with reduced length and duty cycle, as can be seen in figure 3.15.

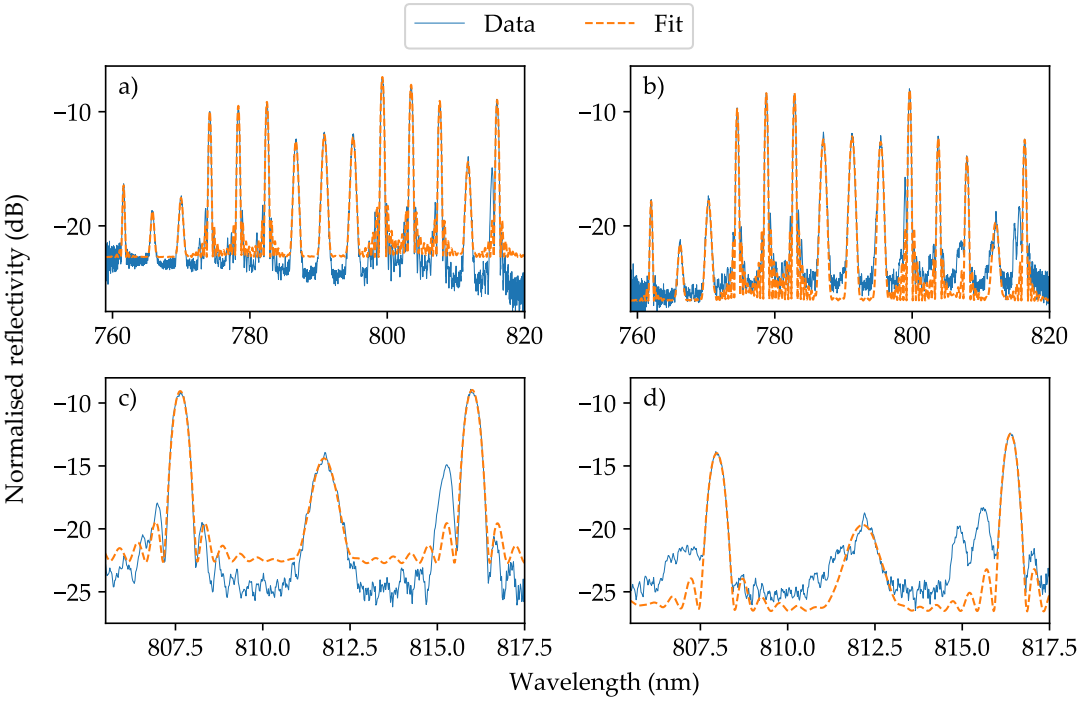

FIGURE 3.15: Reflectance spectra for PX194 devices. a&b) Broad spectrum of gratings in PX194 (after normalisation to 3.3 %) for fluences of 7.2 kJ/cm^2 and 15 kJ/cm^2 respectively. c&d) section of spectra from a&b respectively. A secondary peak at 815.2 nm can be seen for the 7.2 kJ/cm^2 gratings. The 15 kJ/cm^2 gratings at 800 nm and 815 nm are noisy, 'humps' and sidelobes can be seen for all the gratings shown in d).

Firstly, gratings were qualitatively analysed to attempt to infer an optimum writing fluence. High wavelength gratings ($>$ 798 nm) tended to exhibit perturbations to spectral profile and additional spectral peaks before the rest of the gratings in any given waveguide. These gratings were close to the centre of the chip; the multi-mode behaviour would be explained by a minor angular misalignment along the waveguide axis when mounting the chips. At the start of each waveguide the writing spot is slightly out of focus, resulting in a larger (and therefore lower fluence) writing spot. Towards the centre of the device the angular misalignment brought the device into the focal plane of the writing spot resulting in higher fluence and multimode behaviour. At the other end of the waveguide the beams are again out of focus, resulting in a lower fluence. The grating at 816 nm has an anomalous second peak, visible even when all other gratings showed a single peak (indicating single-mode operation). It is thought that this peak is due to the close proximity between that grating and the front facet.

Quantitative analysis was also attempted using the fitting algorithm described in section 3.3.3. Firstly the effective index of the waveguides at different fluences were calculated fitting the peak reflective wavelength of each grating against the fabricated period (see figure 3.16). As expected, the effective index increases as higher writing fluences are used. Writing time has also been indicated on each data point, it can be clearly seen

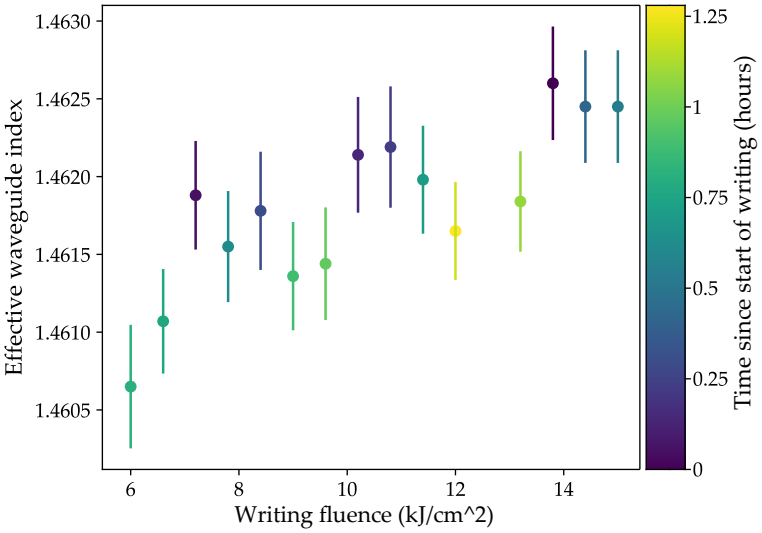

FIGURE 3.16: Fitted n_{eff} of waveguides at different wavelengths, measured using Bragg wavelength. Writing time color coded to give an indication of effects of outgassing. Darker shades represent waveguides written within a shorter time of being removed from storage in liquid nitrogen (to indicate outgassing effects).

that those waveguides written first sit above the general trend and those written later sit below it due to hydrogen outgassing. The curve follows expected photosensitive behaviour with fluence: increasing the fluence results increases the induced refractive index, tending toward a constant value. Subject to higher order modes and saturation behaviour, greater fluence results in stronger gratings.

The AC refractive index modulation can be extracted from uniform gratings using coupled mode theory (see figure 3.17). The fitting algorithm was modified to use the spectral profile from equation 3.14 rather than a simple sinc^2 model. This allows changes in the strength of each grating plane to be decoupled from the duty cycle or grating length, as each parameter has a different effect on the shape of the coupled mode theory grating profile. Unfortunately as the gratings were not saturated ($\kappa L_g << 1$) they were still in the Fourier transform limit. This meant it was very difficult to decouple waveguide loss from trends in refractive index modulation; fits for Δn_{AC} were highly variable.

The propagation loss for each waveguide was extracted using the method described by Rogers et al. [8] and is shown in figure 3.18. This propagation loss describes the change in power due to the waveguide, irrespective of any coupling loss. Above fluences of $9\,\text{kJ/cm}^2$ the data is does not follow a clear trend, however at lower fluences a positive trend between fluence and propagation loss can be seen. It is proposed that at low fluences devices are single-mode, however cladding modes couple small amounts of light causing propagation loss in the channel mode. As the fluence increases the first cladding mode overlaps more with the core until it becomes the first order waveguide mode at around $12\,\text{kJ/cm}^2$. These results suggest that for single-mode waveguides with weaker

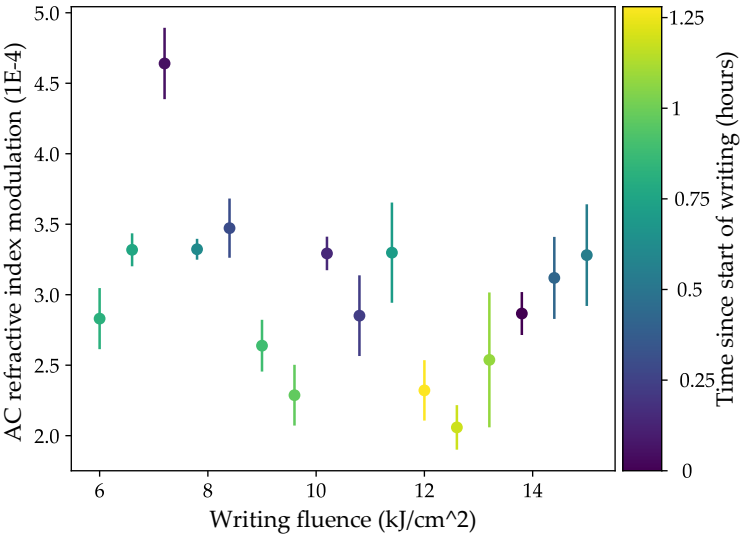

FIGURE 3.17: Variation in AC refractive index modulation with fluence. Darker shades represent waveguides written within a shorter time of being removed from storage in liquid nitrogen (to indicate outgassing effects).

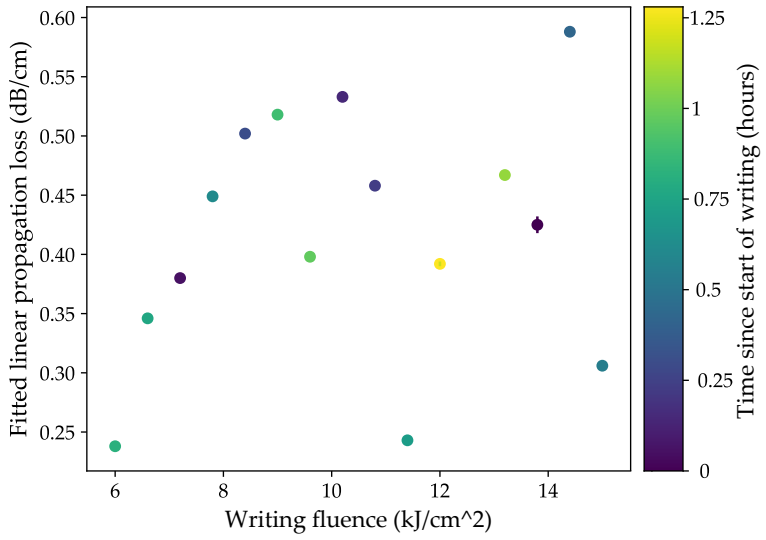

FIGURE 3.18: Measured propagation loss as a function of fluence. Darker shades represent waveguides written within a shorter time of being removed from storage in liquid nitrogen (to indicate outgassing effects).

gratings fluences near $6\,\mathrm{kJ/cm^2}$ are appropriate, whereas for stronger gratings, albeit with higher loss, fluences of $10\,\mathrm{kJ/cm^2}$ are better.

3.5 Conclusions

This chapter has presented a theoretical backgrounds to waveguides and Bragg gratings. Analytic solutions to Bragg grating spectra have been derived for use in characterisation. Typical characterisation methods for planar UV-written devices with Bragg gratings have been described, notably mode profiling and reflection spectrum interrogation.

A new FHD core recipe was developed to support a planar waveguide and a UV written channel waveguide (in conjunction with existing cladding layers) at 780 nm. FDTD modelling was used to ensure channel waveguides would be single mode, alongside effective index modelling to ensure single mode planar waveguides. After wafer iterations to ensure the fabricated layers matched the target recipe, channel waveguides and Bragg gratings were fabricated inside core glass layers using ssDUW. One of the fabricated wafer recipes (PX194) was found to support single-mode channel waveguides with strong Bragg gratings for fluences of $5\,\mathrm{kJ/cm^2}$ and $12\,\mathrm{kJ/cm^2}$. Modelling of the layer structure suggests this wafer should also support single-mode planar waveguides.

Reflection spectra of fabricated Bragg gratings were analysed in detail to investigate the optimum writing fluence for both propagation loss and refractive index modulation. It was found that wafer PX194 produced single mode waveguides between fluences of $6\,\mathrm{kJ/cm^2}$ and $10\,\mathrm{kJ/cm^2}$, with lower fluences resulting in better propagation loss, and higher fluences resulting in stronger gratings. Propagation losses between 0.25 dB/cm and 0.6 dB/cm were obtained, and grating index modulation was estimated at 3×10^{-4}.

The substrates developed in this chapter are used later in chapter 6 to fabricate spectrometers at 780 nm.

3.6 References

[1] K. Okamoto, *Fundamentals of optical waveguides*, 2nd ed. Academic Press, 2006.

[2] T. Erdogan, "Fiber grating spectra," *Journal of Lightwave Technology*, vol. 15, no. 8, pp. 1277–1294, 1997.

[3] C. Sima, "Integrated planar Bragg grating devices for advanced optical communication systems," Ph.D. dissertation, 2013.

[4] J. Skaar, "Synthesis and characterization of fiber Bragg gratings," Ph.D. dissertation, 2000.

[5] "Lasers and laser-related equipment — Test methods for laser beam parameters — Beam widths, divergence angle and beam propagation factor," International Organization for Standardization, Tech. Rep., 1999.

[6] R. Bannerman, "Microfabrication of waveguide devices for quantum optics," Ph.D. dissertation, 2019.

[7] P. L. Mennea, W. R. Clements, D. H. Smith, J. C. Gates, B. J. Metcalf, R. H. S. Bannerman, R. Burgwal, J. J. Renema, W. S. Kolthammer, I. A. Walmsley, and P. G. R. Smith, "Modular linear optical circuits," *Optica*, vol. 5, no. 9, pp. 1087–1090, 2018.

[8] H. L. Rogers, S. Ambran, C. Holmes, P. G. R. Smith, and J. C. Gates, "In situ loss measurement of direct UV-written waveguides using integrated Bragg gratings.," *Optics letters*, vol. 35, no. 17, pp. 2849–2851, 2010.

[9] E. Jones, T. Oliphant, P. Peterson, *et al.*, *SciPy: Open source scientific tools for Python*, 2001. [Online]. Available: `http://www.scipy.org/`.

[10] I. H. Malitson, "Interspecimen comparison of the refractive index of fused silica," *Journal of the Optical Society of America*, vol. 55, no. 10, pp. 1205–1209, 1965.

[11] H. L. Rogers, "Direct UV-written Bragg gratings for waveguide characterisation and advanced applications," Ph.D. dissertation, 2013.

Chapter 4

Modelling of blazed Bragg gratings and aberrations

Blazed Bragg gratings allow light to be coupled and focused out of waveguides onto a detector, with the position on the detector dependent on wavelength, as shown in figure 4.1. Such devices form the centre of the spectrometer scheme investigated in this thesis. Iteration of device fabrication using ssDUW is extremely time-consuming and only limited information can be recovered during characterisation. Theoretical models are required to probe the initial design space and understand the influence of various physical effects.

Models have previously been presented [1], [2] based on specific devices using a Rowland circle geometry and an array of receiver waveguides. These models were only concerned

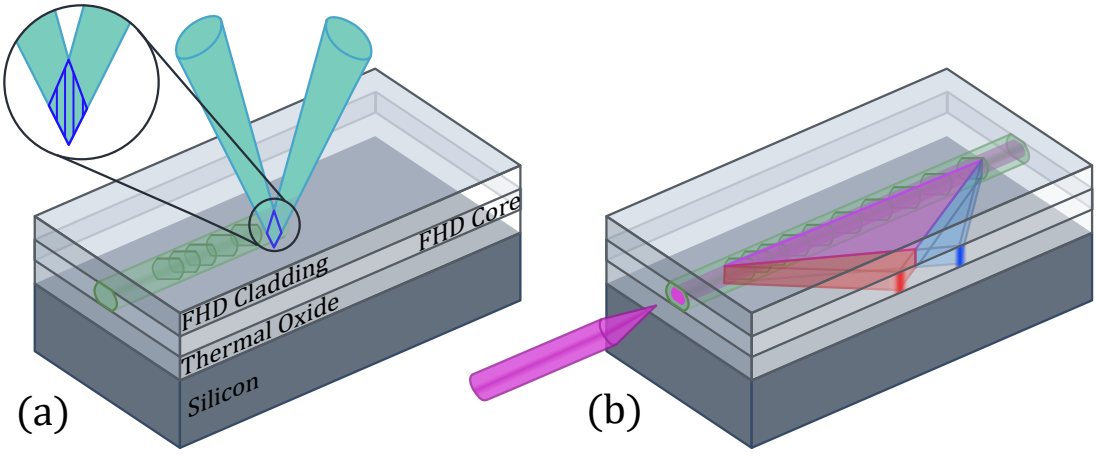

FIGURE 4.1: Proposed highly-chirped 45° blazed Bragg grating spectrometer scheme, reproduced from figure 1.1. a) FHD platform and ssDUW fabrication of gratings and channel waveguide inside photosensitive core layer. b) Input spectra coupling into channel waveguide is diffracted out of the channel waveguide into a planar waveguide. The light focuses onto the side facet, where a detector will be mounted.

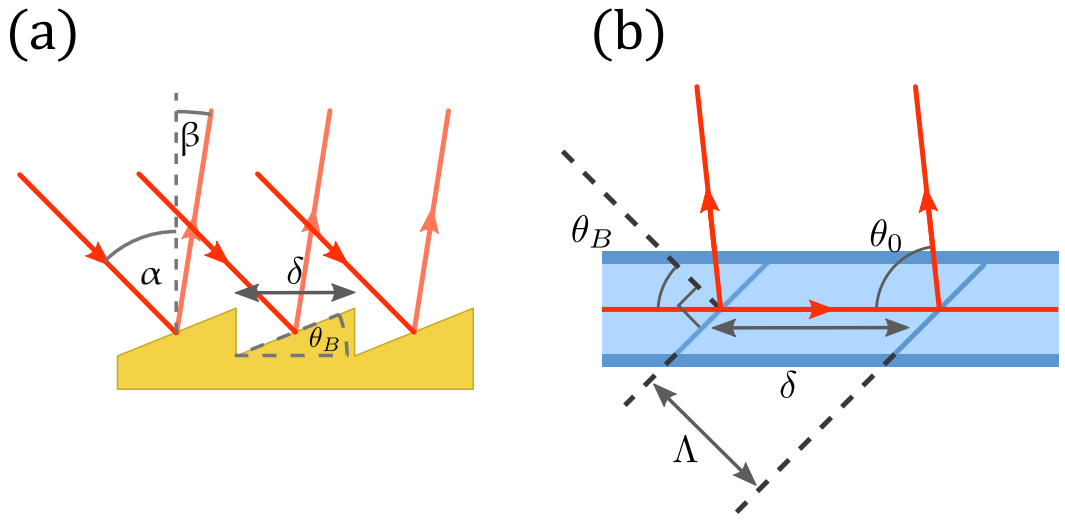

FIGURE 4.2: a) Blazed diffraction grating showing angle conventions. b) Blazed Bragg grating construction showing definitions of distances and angles.

with the output from the receiver waveguide and ignored much of the behaviour outside the focal plane. I was particularly interested in creating a full 2D intensity map of the focus, as it imparts a lot of information about imaging aberrations, and is helpful in considering optimised device geometries. In addition I wanted to create a model that could be iterated over different wavelengths to investigate the resolution and bandwidth behaviour of devices, neither of which had previously been modelled.

This chapter starts with a presentation of different methods used to model the blazed chirped Bragg gratings developed in this thesis, as well as the approximations and limitations of each method. It then discusses device design and aberrations, and uses these models to correct for imaging aberrations and increase the performance of modelled blazed Bragg grating spectrometers. All models shown in this chapter have been developed using Python.

4.1 Models of blazed Bragg gratings

4.1.1 Ray modelling

Blazed Bragg gratings are diffraction gratings hosted within waveguides; light incident on the grating is diffracted, with the diffraction angle dependent on the wavelength of the light. They are a general analogue of Bragg gratings whereby rotating the grating planes allows efficient diffraction outside of the waveguide, rather than restricting reflections to the waveguide axis. Provided a grating is long, the light diffracted out of the grating approximates a planar wave. The angle at which the plane wave travels can be calculated using the grating equation

$$\delta(\sin\alpha - \sin\beta) = m\lambda, \tag{4.1}$$

where α and β are respectively the incident and diffracted angle from the grating, and δ is the distance between grating teeth as shown in figure 4.2. In a blazed Bragg grating α is fixed at $\pi/2$ by the waveguide geometry. We follow the conventions defined by Koeppen and Madsen [3], [4] and define an 'observation angle' as $\theta_o = \beta + \pi/2$. For first order diffraction ($m = 1$), θ_o satisfies

$$n_e\delta(1 + \cos\theta_o) = \lambda, \tag{4.2}$$

$$\delta = \frac{\Lambda}{\cos\theta_B}, \tag{4.3}$$

where n_e is the effective index of the waveguide and equation 4.3 can be used to link the blazed grating period δ to the perpendicular grating period Λ (also the interference period defined in chapter 2). Note that the blaze angle does not impose a restriction on diffraction under these equations, indeed an unblazed Bragg grating should diffract light (away from the Bragg wavelength) out of the waveguide. In practice this is rarely observed due to constraints on reflection, these are discussed in more detail in section 4.2.5.

Ray modelling is incapable of modelling the output intensity distribution of the device, nevertheless it is very useful for gaining insight about device performance. A long constant period grating diffracts a plane wave out of a waveguide, we can define a ray as the normal to that plane wave. The angle of such a ray is given by equation 4.2. This approach can be extended to chirped Bragg gratings; provided the grating chirp is slow ($\mathrm{d}\Lambda/\,\mathrm{d}x \ll \Lambda$, using the conventions shown in figure 4.3a) the Bragg grating can be broken into short sections of approximately constant period. The angle of diffraction in such a case is set by the focal grating period; the path of these rays can be traced using the local diffraction angle to construct a ray diagram.

Figure 4.3b shows that ray tracing can be used to visually identify the presence of a focus. By modelling rays using different wavelengths the dispersive properties of the device can also be investigated. Unfortunately ray modelling cannot show the intensity pattern of the light. An approach by Madsen et al. used Gaussian optics to predict the size of the focal spot for a Gaussian apodised grating and calculate the resolution [4].

Ray modelling is used as a first check when designing devices or making modifications to existing devices. The model is extremely quick to run and provides a visual confirmation of the focal length and the presence of aberrations which does not depend on the paraxial approximation. Ray intercept diagrams were also used to provide quantitative analysis of aberrations as well as designing a period to correct for aberrations.

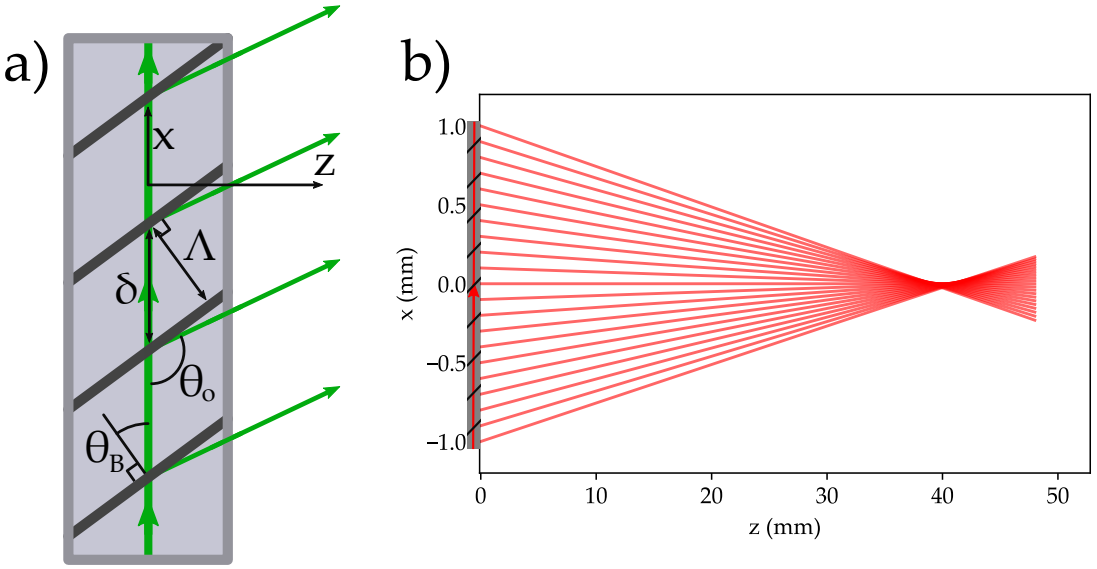

FIGURE 4.3: a) Definitions and geometric conventions used in this chapter. b)Ray tracing for a grating with linearly decreasing period, with a focal length of 40 mm.

4.1.2 Beam propagation modelling

A full intensity model gives a much more intuitive understanding of the effects of aberrations. Such a model can also be directly compared to experimental results. The first attempt at an intensity model used the beam propagation method, which provides a solution to the electric field at a plane of interest, $E(x, z)$, given the electric field at a starting plane, $E(x, z = 0)$, within the paraxial approximation [5], [6]. Figure 4.4 shows the geometric conventions used for the beam propagation model (and all other models in this chapter). The beam propagation model uses a Fourier space propagator to calculate the field away from the starting plane:

$$\hat{E}(u, z = 0) = \mathcal{F}\{E(x, z = 0)\}, \tag{4.4}$$

$$\hat{E}(u, z) = \hat{E}(u, z = 0) \exp\left(-\mathrm{i}kz\sqrt{1 - u^2\lambda^2}\right), \tag{4.5}$$

$$E(x, z) = \mathcal{F}^{-1}\{\hat{E}(u, z)\}, \tag{4.6}$$

where $\hat{E}$ denotes the Fourier transform of E and u is a spatial frequency corresponding to the x axis. $\mathcal{F}, \mathcal{F}^{-1}$ denote the Fourier transform and inverse Fourier transform respectively. It should be apparent from figure 4.4 that a natural choice of the starting electric field is the electric field instantaneously after reflection from the grating planes. This near field, E_{near}, can be calculated by deconstructing the grating into a series of constant refractive index planes and summing the individual contribution from each plane. The field reflected from each plane depends on the strength of the Fresnel reflection from the boundary, as well as the size of the plane

$$E_{\mathrm{near}}(x) = \int_{-\infty}^{\infty} E_1(x) r(x') w(x, x')\, \mathrm{d}x', \tag{4.7}$$

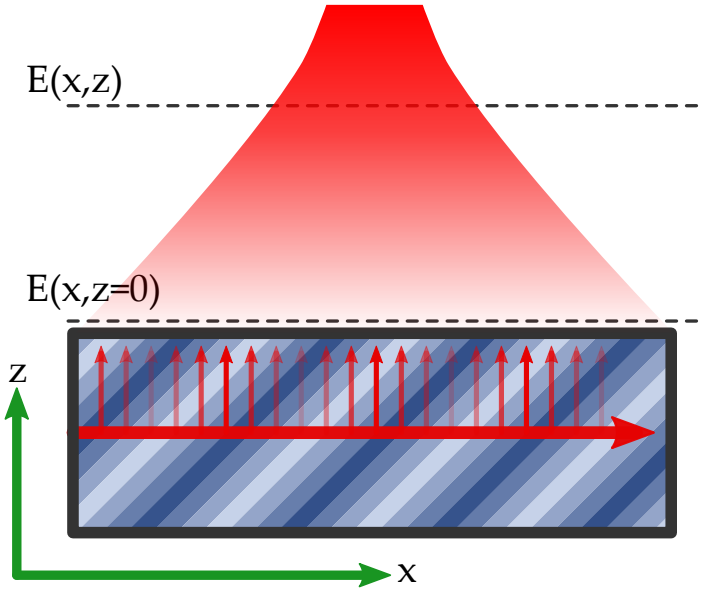

FIGURE 4.4: Geometry used for beam propagation model. A grating is split into thin slices of constant refractive index. The near field is comprised of Fresnel reflections from refractive index planes.

where $E_{\text{near}}(x)$ is the near field at a distance x along the waveguide, $E_1(x)$ is the magnitude of the electric field inside the waveguide at a position x, $r(x)$ is the Fresnel coefficient for a refractive index plane at x and $w(x, x')$ encompasses the variation in r due to the finite width and refractive index profile of the waveguide. If we consider the case of a step index waveguide with a blazed grating, the planes will have a finite width in the x axis dependent on the width of the waveguide and the blaze angle of the grating. We can make the non-depleted-pump approximation and replace $E_1(x)$ with a constant E_0, the field incident on the waveguide. r can be calculated by considering the refractive index contrast and blaze angle of the grating. The Fresnel coefficients for reflection at an oblique interface are given in chapter 1 of [7]:

$$r_{\text{TM}} = \frac{n_1 \cos\theta_i - n_2 \cos\theta_t}{n_1 \cos\theta_i + n_2 \cos\theta_t}, \tag{4.8}$$

$$r_{\text{TM}} = \frac{n_2 \cos\theta_i - n_1 \cos\theta_t}{n_2 \cos\theta_i + n_1 \cos\theta_t}. \tag{4.9}$$

$$\tag{4.10}$$

where the subscripts denote the r coefficients for TE and TM polarisation,n_1 and n_2 are the indices before and after an interface respectively, and θ_i and θ_t denote the incident and transmitted angle respectively. The refractive index can be eliminated using Snell's

law

$$r_{\mathrm{TM}} = \frac{\sin(\theta_i - \theta_t)}{\sin(\theta_i + \theta_t)}, \tag{4.11}$$

$$r_{\mathrm{TE}} = \frac{\tan(\theta_i - \theta_t)}{\tan(\theta_i + \theta_t)} \tag{4.12}$$

For a boundary between n_0 and $n_0 + \Delta n$ the transmitted angle has a small deviation, $\Delta\theta$, from the incident angle

$$n_0 \sin\theta_i = (n_0 + \Delta n)\sin(\theta_i + \Delta\theta), \tag{4.13}$$

$$n_0 \Delta\theta \cos\theta_i = -\Delta n \sin\theta_i, \tag{4.14}$$

$$\Delta\theta = -\frac{\Delta n}{n_0}\tan\theta_i. \tag{4.15}$$

For a 45° blazed grating with low index contrast $\theta_i + \theta_t \approx 90°$, therefore

$$r_{\mathrm{TE}} \approx 0, \tag{4.16}$$

$$r_{\mathrm{TM}} \approx \sin\Delta\theta \approx \frac{\Delta n}{n_0}. \tag{4.17}$$

From equation 4.7 we must also consider $w(x, x')$. As r is proportional to Δn, w is given by the relative envelope of the refractive index profile of the grating plane across the waveguide, projected along the x axis. E_{near} is given by the convolution of E_{in} with w, in Fourier space this acts as a filtering term. Narrow waveguides have a narrow distribution for w, which leads to a wide filter in spatial frequency space. Conversely wide waveguides have a sharp filter on spatial frequencies.

The beam propagation method decomposes input fields into plane waves travelling at different angles; the projection of their k-vector onto the x-axis means that plane waves with the same wavelength have different spatial frequencies (depending on their propagation angle). A narrow spatial frequency filter (from a wide waveguide) suppresses the angular range at which plane waves travel or can be diffracted at. In a blazed Bragg grating different wavelengths phasematch at different diffraction angles (as shown in equation 4.2); w imposes a limit on the actual diffraction bandwidth. The beam propagation method used here is only valid in the paraxial approximation, outside which it develops phase errors which are visible as spurious aberrations. We will consider the narrow waveguide approximation, $w(x, x') = \delta(x - x')$, therefore highlighting the effects of any gratings which exceed the paraxial approximation. Under this approximation equation 4.7 becomes

$$E_{\mathrm{near}}(x) = E_0 \frac{\Delta n(x)}{n_0}. \tag{4.18}$$

This allows the electric field (and hence intensity) to be calculated at z planes using efficient fast Fourier transform algorithms. The beam propagation model provided fast modelling of intensity patterns and was extremely useful for initial device iteration. It

was used as a basis for testing aberration corrections derived in section 4.2.2, resolution modelling of devices with flat focal planes shown in section 4.2.4 as well as understanding fabricated devices in chapter 5.

Later work in chapter 6 investigated devices which were outside of paraxial focusing approximations as well as using gratings with variable blaze angle, which were unsuitable for modelling with the beam propagation method. The beam propagation model was unable to account for effects of variable blaze angle and started showing spurious aberrations due to phase errors in the model outside the paraxial approximation. As a result a new model using scalar diffraction theory was derived.

4.1.3 Scalar diffraction modelling

This section follows the derivation of scalar diffraction theory given in chapter 13 of Born and Wolf [7], with some modifications to consider diffraction from weak perturbations from a bulk refractive index. Maxwell's equations inside an inhomogeneous material in the absence of microscopic charges can be used to create a wave equation

$$\boldsymbol{\nabla}^2\mathbf{E} - \epsilon\mu\ddot{\mathbf{E}} + (\boldsymbol{\nabla}\ln\mu)\times\boldsymbol{\nabla}\times\mathbf{E} + \underbrace{\boldsymbol{\nabla}\left(\mathbf{E}\cdot\boldsymbol{\nabla}\ln\epsilon\right)}_{\text{mixing term}} = 0, \tag{4.19}$$

where ϵ and μ are the permittivity and permeability of the material. Typically the form of the wave equation neglects the differential terms in $\ln\mu$ and $\ln\epsilon$, however we must consider them due to the spatial variation in refractive index. In a dielectric material $\mu = 1$ and refractive index variation is encoded in ϵ via $n^2 = \epsilon$. The final term on the right is referred to as a 'mixing term', as it is the only term that couples orthogonal components of the electric field to each other in the wave equation. In the absence of the mixing term each component of the electric field can be considered independently, which makes analytic solutions much simpler. For an input plane waves with a wavevector k, the mixing term is on the order of $k^2\Delta n^2$. This is much smaller than the other terms provided that $\Delta n^2 \ll 1$. This has been verified by explicitly calculating terms using a modelled grating. Under this approximation the mixing term can be neglected in equation 4.19 resulting in the Helmholtz equation

$$\boldsymbol{\nabla}^2 U(\mathbf{r},\omega) + k^2 n^2 U(\mathbf{r},\omega) = 0, \tag{4.20}$$

where we have introduced a scalar field U which contains spatial and temporal variation such that $\mathbf{E} = \mathbf{E_0}U$, where $\mathbf{E_0}$ is constant. The scalar field U extends across all space and can be separated into an incident field, $U^{(\mathrm{i})}$, and a scattered field, $U^{(\mathrm{s})}$. $U^{(\mathrm{i})}$ is the input into the system (well described by a superposition of plane waves) and $U^{(\mathrm{s})}$ is the change in U due to the presence of the scatterer. $U^{(\mathrm{i})}$ is a solution of the Helmholtz

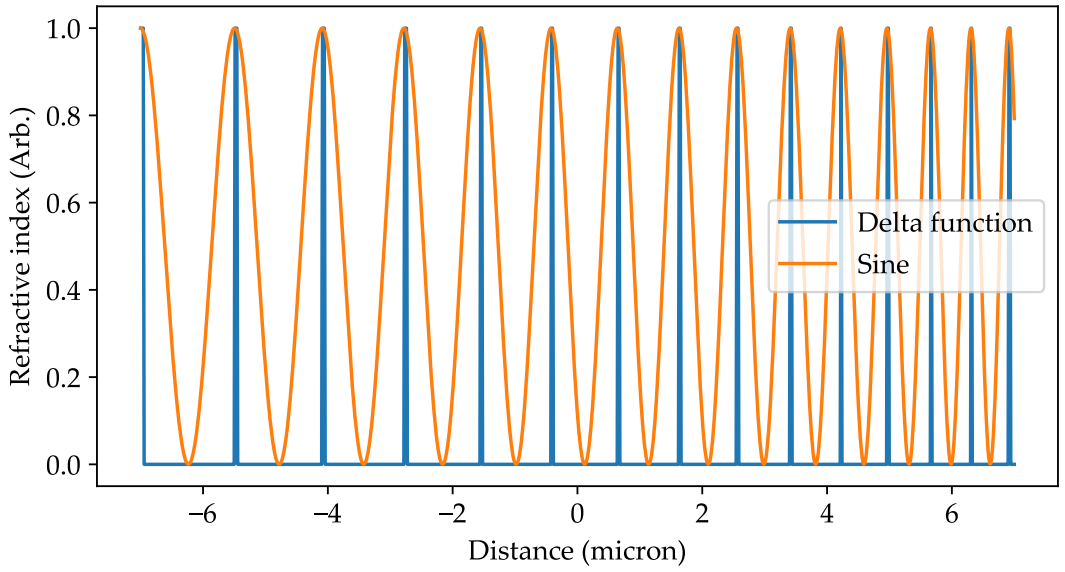

FIGURE 4.5: Comparison of delta function refractive index variation and sinusoidal refractive index variation

equation outside the grating (when $n = n_0$). If we define a scattering potential

$$F(\mathbf{r}, \omega) = \frac{1}{4\pi} k^2 \left[n^2(\mathbf{r}, \omega) - n_0^2 \right], \tag{4.21}$$

then the scattering field can be found using eqn.4.20

$$(\boldsymbol{\nabla}^2 + n_0^2 k^2) U^{(\mathrm{s})}(\mathbf{r}, \omega) = -4\pi F(\mathbf{r}, \omega) U(\mathbf{r}, \omega). \tag{4.22}$$

After some manipulation using Green's functions [7] it can be shown that the scattered field is given by

$$U^{(\mathrm{s})}(\mathbf{r}, \omega) = \int_V F(\mathbf{r}', \omega) U(\mathbf{r}', \omega) \frac{e^{\mathrm{i}n_0 k|\mathbf{r}-\mathbf{r}'|}}{|\mathbf{r}-\mathbf{r}'|} \, \mathrm{d}^3 r' \,. \tag{4.23}$$

As the refractive index contrast is weak, we can make the first order Born approximation and replace $U(\mathbf{r}', \omega)$ inside the integral with $U^{(\mathrm{i})}(\mathbf{r}', \omega)$. This is equivalent to making the approximation that the scattering probability is low enough that each ray will experience (at most) a single scattering event and in addition, such scattering events will not reduce the power in the waveguide (non-depleted pump approximation). We can further simplify matters by expanding the scattering potential for a weak refractive index

$$F(\mathbf{r}, \omega) \approx \frac{1}{4\pi} k^2 \left[2n_0 \Delta n(\mathbf{r}) \right], \tag{4.24}$$

$$U^{(s)}(\mathbf{r}, \omega) \approx \frac{k^2}{4\pi} \int_V \left[2n_0 \Delta n(\mathbf{r}) \right] \frac{e^{\mathrm{i}kn_0|\mathbf{r}-\mathbf{r}'| + \mathrm{i}kn_0 \mathbf{r}\cdot\hat{\mathbf{z}}}}{|\mathbf{r}-\mathbf{r}'|} \, \mathrm{d}^3 r' \,. \tag{4.25}$$

Note that here we have ignored the effects of dispersion and continued the convention of propagation along the z axis. Finally we can make an additional approximation

to simplify the computation of the scattered field. In a holographically defined Bragg grating the (unapodised) refractive index profile is a smoothly varying function

$$\Delta n(x) \sim \frac{1}{2} \sin \left[\int_0^x \frac{2\pi \cos \theta_B(x')}{\Lambda(x')} \, \mathrm{d}x' \right] + \frac{1}{2}. \tag{4.26}$$

As the refractive index varies the strength of the scattering varies; the integral must be sampled at a higher rate than the grating oscillation to observe the effect on the scattered field. Figure 4.5 shows an alternative grating using a Dirac delta response

$$\Delta n(x) \sim \sum_{j=0}^{N} \left\{ \int_0^x \delta^{(1)} \left[\int_0^{x'} \frac{2\pi \cos \theta_B(x'')}{\Lambda(x'')} \, \mathrm{d}x'' - 2j\pi \right] \mathrm{d}x' \right\}. \tag{4.27}$$

Here we need only sample points on the grating planes themselves, drastically reducing the number of sampling points required (and therefore computational time). This approximation holds provided the number of grating planes is large (there are enough grating planes such that the phasematching condition for the grating is narrow compared to the grating period). This approximation changes the normalisation factor required, which has not currently been investigated rigorously. As a result, modelling results are normalised using either the peak intensity or total intensity of the diffraction pattern measured with the design wavelength. This method is less computationally efficient than the beam propagation method, however it is correct outside the paraxial approximation. The beam propagation method also relies on evaluation at a plane parallel to the input field; for the field at a plane non-normal to the input field the scattering model is often more efficient.

4.2 Modelling results

Modelling was used to investigate the potential performance of ssDUW blazed Bragg grating spectrometers without fabrication iterations. The design space for these devices was complex, and fabrication and characterisation iterations were time intensive. Modelling was used to investigate new device designs, as well as understand imperfections in fabricated devices.

Early in the project it was found using approximate geometric arguments that an increase in device length would increase the spectral resolution of the device. Modelling was used to verify this relation in realistic devices.

Early modelling work investigated the differences between the 45° blazed Bragg grating scheme and the small angle scheme presented by Wagener et al. [8], in particular the effects of linear period chirp. It was found that a linear chirp results in significant aberrations when the ratio of the grating length (projected along the focal direction) to the focal length exceeds 0.1. These aberrations were investigated using the beam

propagation model and ray model and an alternative chirp function was derived using the ray model.

Beam propagation modelling was used to investigate the potential resolution of devices. It was found that the focal length changed with wavelength, as such an angled focal plane resulted in a better resolution, which was verified using the scalar diffraction model. Finally the scalar diffraction model was used to investigate the limiting factors on device bandwidth.

4.2.1 Focal length and resolution

In Field et al. [9] I derived both the focal length and resolution of blazed chirped Bragg gratings using a ray model approach, combined with the Gaussian optics method suggested by Madsen et al. [4]. They are given by:

$$f \approx \frac{n_e \Lambda_0^2 \sin^2 \theta_o}{\lambda \cos \theta_B C}, \tag{4.28}$$

$$\Delta\lambda_{\mathrm{FWHM}} = \frac{2\sqrt{2 \ln 2}\lambda^2}{n_e \pi L_g (1 + \cos \theta_o)}, \tag{4.29}$$

where Λ_0 is the average period of the chirped grating, C is $\mathrm{d}\Lambda/\,\mathrm{d}z$, and L_g is the length of the grating. Though the approximations used in their derivations are only valid for low chirp rates, they remain relatively accurate for most devices modelled in this chapter. In addition they give first insights into how devices behave. The focal length is inversely proportional to rate of period chirp, as suggested previously by [3], [4], with $\mathrm{d}\Lambda/\,\mathrm{d}x \approx -75\,\mathrm{nm/mm}$ for a focal length of 10 mm at 1550 nm in 45° chirped devices. This chirp is large, however well within the fabrication limits of the ssDUW system. Similar to bulk diffraction grating spectrometers, the resolution is inversely proportional to the maximum path length difference between rays exiting the device. This means that resolution can be increased by making longer devices, or by reducing θ_o. Additionally the focal length is not included in the resolution and is a free parameter. This allows considerable design flexibility in devices, as the focal length can be adjusted to ensure the distance between two minimally resolved wavelengths on the detector is greater than the pitch between pixels.

4.2.2 Linear period detuning in 45°devices

The small angle spectrometer scheme proposed by Wagener et al. [8] showed that a linear change in grating period with distance results in a focus, with the focal length predicted by equation 4.28. Changing the input wavelength results in angular dispersion, converting spectral information into a spatial distribution at the image plane. Figure

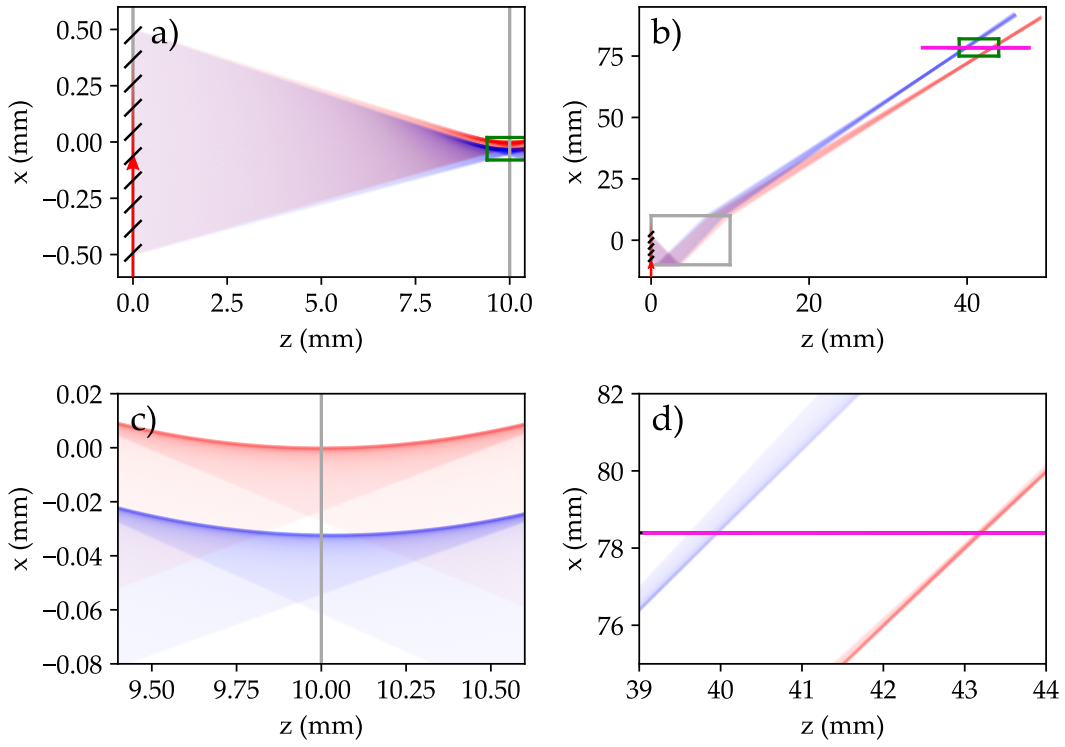

FIGURE 4.6: Ray tracing for linear period chirp in small angle scheme and perpendicular scheme for light at 1550 nm and 1555 nm (red and blue respectively). Chip extents shown in grey. a) Perpendicular scheme with a focal length of 10 mm, designed to focus on side facet of chip. b) Small angle device using parameters from [4], with detector plane shown in magenta. c) Zoom detail of green box in a) showing wavelength dispersion and aberrations. d) Zoom detail of green box in b) showing wavelength dispersion and aberrations. Aberrations are much more apparent in perpendicular scheme.

4.6b illustrates this, though the small chirp used in the small angle scheme results in a long focal length (~ 100 mm); the focal plane was significantly outside the device.

By constructing a ray trace diagram with partly transparent rays (as in figure 4.6), the concentration of rays can be observed by the strength of color at any particular point. From figures 4.6a & 4.6b respectively it can be seen that both the perpendicular scheme and the small angle scheme result in spatial separation of different wavelengths. The degree of separation in the small angle scheme is far greater due to the large focal length, and the reflection in the small angle scheme results in inverted spatial dispersion at the detector plane. Figures 4.6c and 4.6d show the foci in more detail and highlight aberrations present in the focus. Rather than all passing through a mutual focal point the rays bunch towards the low wavelength side of the detector plane. This aberration is much more prevalent in the 45° degree scheme (figure 4.6c) than in the small angle scheme (figure 4.6d). Though an intensity distribution is required to quantitatively investigate the effects of aberrations on resolution, a 'ray-intercept diagram' can be used to identify the types of aberration present and their magnitudes [10]. This evaluates the ray trace at an detector plane as shown in figure 4.7 by plotting the intersection height,

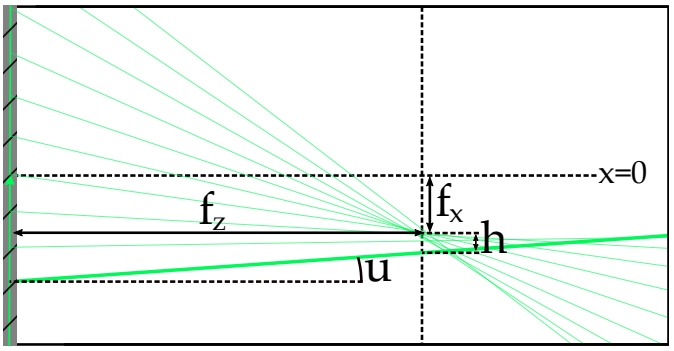

FIGURE 4.7: Rays are traced from a grating to a detector plane $z = f_z$. The distance from the intersection point to the intended focal point f_x (as projected along the detector plane) is given by h. For a perfect focus $h = 0$, for an imperfect focus aberrations will dictate where rays intersect the focal plane. A ray intercept digram quantifies these aberrations using relationship between $\tan u$ and h.

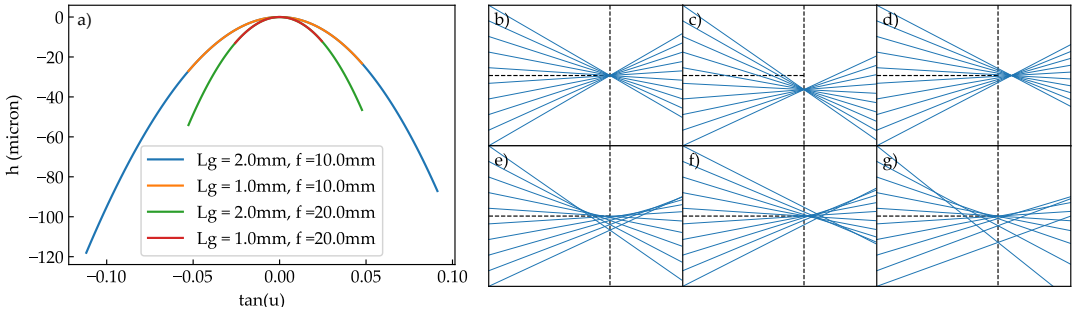

FIGURE 4.8: a) Ray intercept diagrams for 1 mm perpendicular devices of various focal lengths, with an input wavelength of 1550 nm. b) Ray tracing of a perfect focus. c-g) Ray tracing of foci with first 5 Seidel aberrations.

h, of each ray with the detector plane against the tangent of the angle, u, between the ray and the normal to the detector plane. These quantities are related by a polynomial

$$h = f(\tan u), \tag{4.30}$$

$$h \approx a + b\tan u + c\tan^2 u + d\tan^3 u + e\tan^4 u + \ldots, \tag{4.31}$$

where a, b, c, d, e are the coefficients of the first 5 Seidel aberrations and respectively correspond to lateral shift, defocus, coma, spherical aberration and third-order coma [11]. The effects of these aberrations in 2D can be seen in figures 4.8 b-g. By comparing the aberrations in figure 4.8 to the ray modelling in figure 4.6 it can be seen that the bunching effect is typical of coma. A modification to the period of the grating can be used to fix such aberrations. By considering the angle at which each ray must be diffracted to pass through a common focal point the period can be retrieved using equation 4.2:

$$\Lambda(z) = \frac{\lambda_0 \cos\theta_B(z)}{n\left[1 + \frac{z - f_z}{\sqrt{(z-f_z)^2 + f_x^2}}\right]}, \tag{4.32}$$

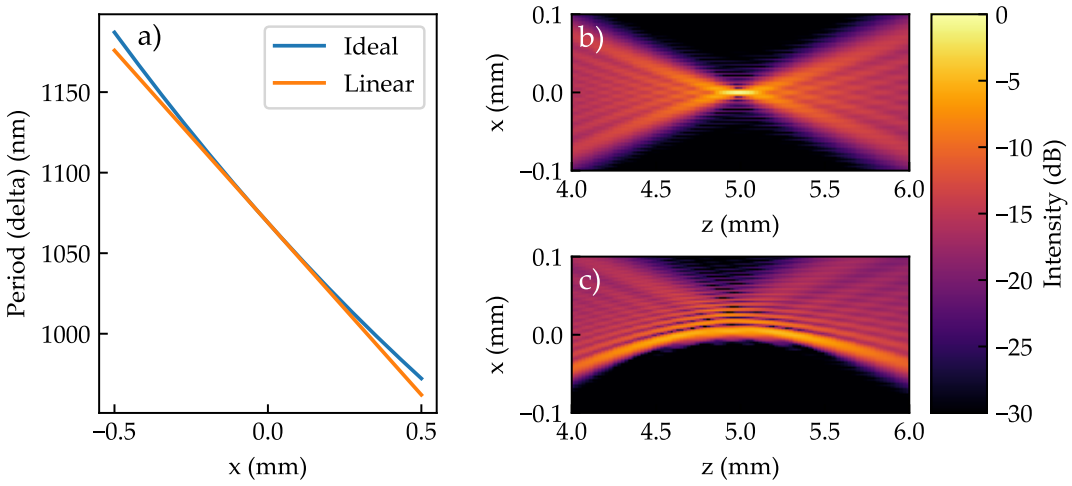

FIGURE 4.9: a) Comparison of linear period with idealised period for $f = 5\,\text{mm}$. b & c) Intensity patterns at focal plane for gratings with idealised grating period and linear period respectively. All modelled using the beam propagation model, $L_g = 1\,\text{mm}$, $f = 5\,\text{mm}$.

where f_x and f_z are projections of the focal position onto the x and z axis respectively as shown in figure 4.7. In general we will consider devices where the ray diffracted from the centre of the grating is perpendicular to the grating itself ($f_x = 0$) in which case $f = f_z$. The focusing properties of such a device are shown in figure 4.9, it can be seen that the focal width of a device without aberrations is much smaller than a device with aberrations, this should result in a substantial increase in the resolving power of such a device.

4.2.3 Wavelength dispersion and optimum detector plane

The aim of the models presented in this chapter is to understand how the parameters which define a blazed chirped Bragg grating relate to output characteristics, namely focal spot size, bandwidth, and spectral resolution. The beam propagation model is primarily used for resolution modelling, as it is more computationally efficient than the scattering model, and typical devices fall within the small angle approximation. Investigations into using detector planes rotated with respect to the grating are modelled using the scattering model, as it is not limited to evaluating planes parallel to the grating like the beam propagation model. The resolution of a device can be analysed by investigating the intensity pattern in the focal plane for different wavelengths. The following section will focus particularly on devices designed to focus light at 1550 nm inside a planar layer with an effective index of 1.45 using a fixed blaze angle of 45°.

As the wavelength is varied the output of the spectrometer moves across the image plane, resulting in spectral dispersion as desired. The dispersion is not as extreme as

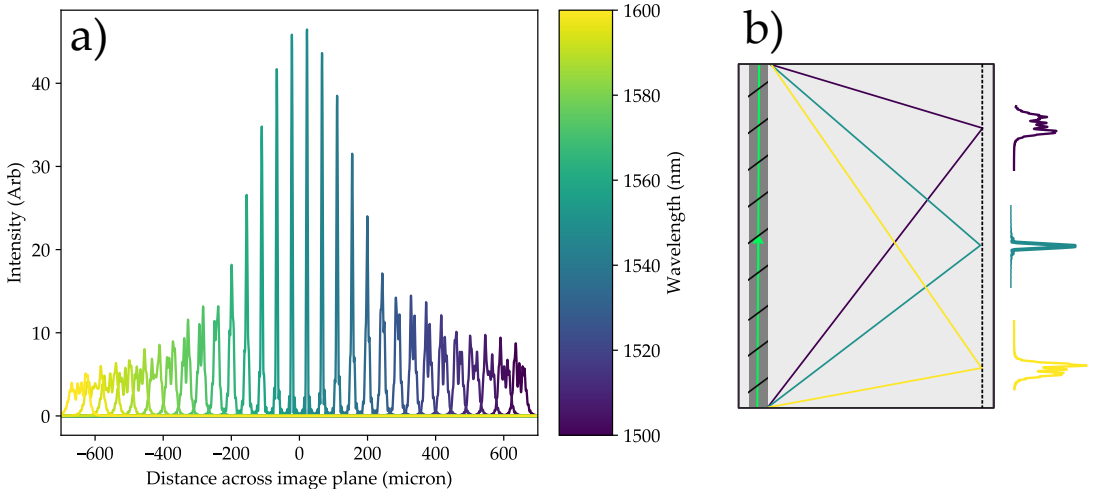

FIGURE 4.10: a) Intensity pattern at focal plane for selection of input wavelengths for a blazed chirped Bragg grating with $f = 10\,\text{mm}$ and $L_g = 1\,\text{mm}$. b) schematic of modelling geometry showing aberrations in detected intensity.

in the small angle scheme (due to the shorter focal length), however the focal spot size should be much smaller. As can be seen in figure 4.10 this is not in fact the case, as away from the design wavelength aberrations start to develop. Figure 4.11a shows the intensity propagation through the focus for a number of wavelengths, it can be seen that the focal plane shifts with wavelength. An estimate of the position of the focal plane was calculated by searching for the coordinate with greatest intensity for each wavelength propagation and is shown in figure 4.11b. Over a 200 nm bandwidth the deviation from a flat focal plane is well defined by

$$\Delta f_z \approx 0.34x^2 + 1.05x + 0.01. \tag{4.33}$$

In general the focal plane curvature is difficult to correct for, however the linear offset in the focal plane may be removed by rotating the detector plane with respect to the grating. For a grating designed to focus at $(0, f_z)$ at a wavelength of λ_0 the position of the focus, (P_z, P_x), for a wavelength $\lambda = \lambda_0 + \Delta\lambda$ is given by:

$$P_z = f_0(1 - \frac{\Delta\lambda}{\lambda_0}), \tag{4.34}$$

$$P_x = -f_0\frac{\Delta\lambda}{\lambda_0}, \tag{4.35}$$

which results in an ideal detector plane at 45° to the grating. This can also be calculated for the device modelled in figure 4.12b by taking the arctangent of the linear term in equation 4.33. This results in a detector plane at 46.4° degrees, very close to the ideal value.

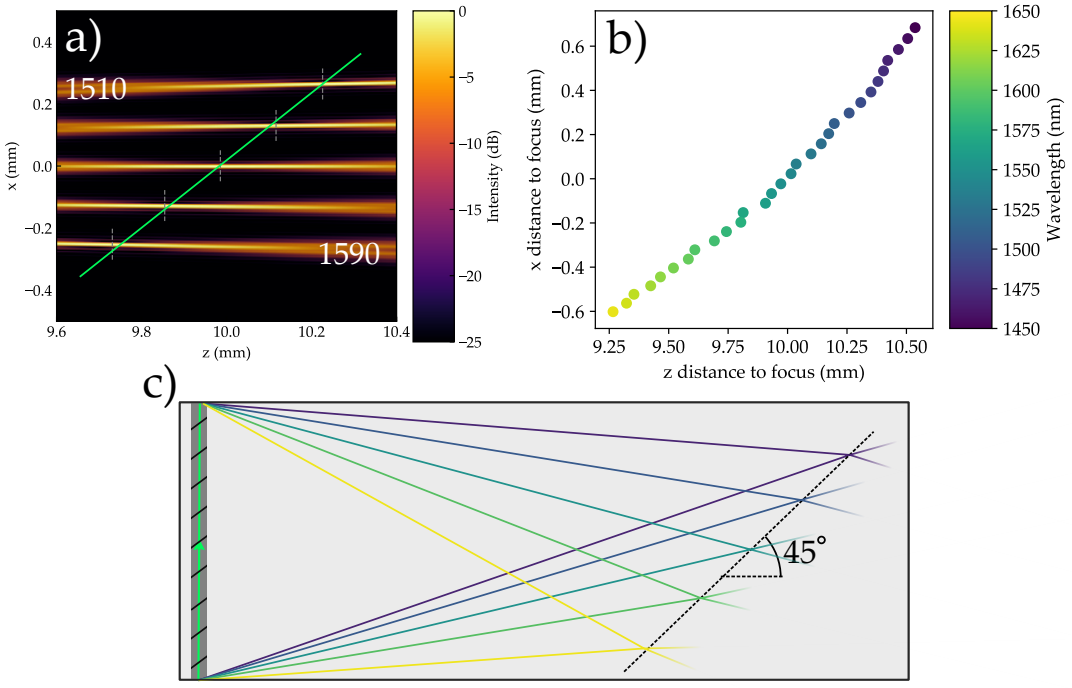

FIGURE 4.11: a) Beam propagation model of focusing for light at 1510 nm, 1530 nm, 1550 nm, 1570 nm and 1590 nm for grating at $z = 0$ with $f = 10$ mm and $L_g = 1$ mm. Focal position at different wavelength follows line marked in green. b) Variation in focal position with wavelength showing focal plane curvature. c) Illustration of focusing at different wavelengths showing ideal detector plane at 45°

4.2.4 Resolution modelling

The Houston criteria states that two wavelengths are resolved if the spatial separation of the two maxima of the intensity distributions is at least the FWHM of either of the single intensity distributions [12]

$$R(\lambda) = w(\lambda)\frac{\mathrm{d}\lambda}{\mathrm{d}x}, \tag{4.36}$$

where R is the resolvable wavelength difference (referred to as the resolution), $w(\lambda)$ is the FWHM of the intensity peak at a wavelength λ. The definition of the Houston resolution uses the single peak intensity distributions rather than the joint distribution of 2 peaks, this means it can be measured experimentally using a single tunable laser. As has been derived earlier in this chapter (see equation 4.29) the resolution of a device is dependent on the length of the grating. The resolution will also be dependent on the chosen detector plane.

As figure 4.12a shows rotating the detector plane results in a greater resolving power across a wide wavelength band while preserving the peak resolution. It also confirms the relation shown in equation 4.29: the peak resolution is inversely proportional to the device length. Shorter devices are much less sensitive to defocus aberrations from

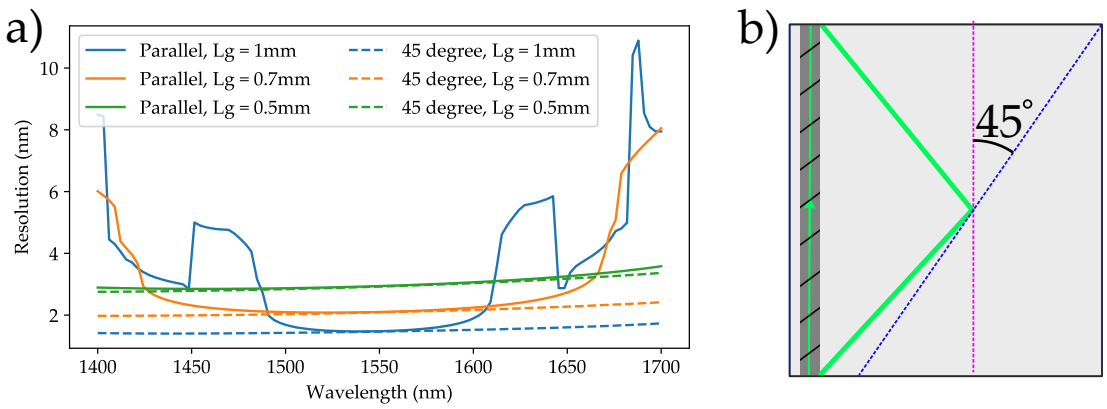

FIGURE 4.12: a) Modelled resolution for gratings of different lengths, with detector planes parallel to the grating and at 45° to the grating b) Illustration of detector plane geometries with parallel and 45° detector planes shown in magenta and blue respectively.

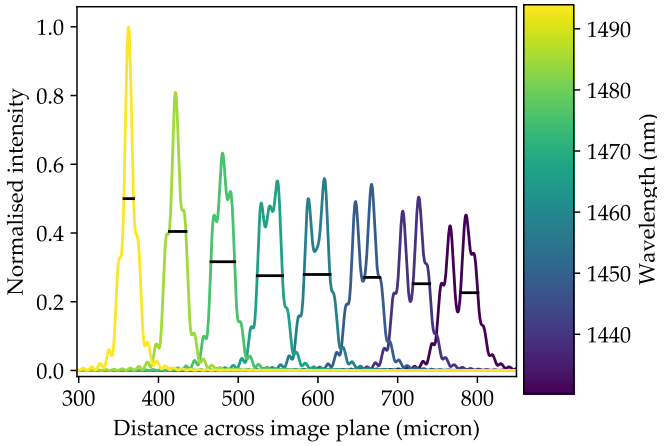

FIGURE 4.13: Intensity profiles for 1 mm perpendicular grating with 'widths' marked by black lines. A discontinuity in the width can be seen between the peaks centred at 600 µm and 670 µm when the minima between the primary peak and the first lobe dips below 50% of the primary peak height.

focal plane curvature, the width of the wavelength band before there are significant problems from such aberrations is approximately proportional to f^2/L_g^2. Figure 4.12 also illustrates one of the issues with the Houston criteria: for peaks with significant lobes the FWHM becomes poorly defined. The intensity patterns around the discontinuity at 1450 nm in figure 4.12 are shown in figure 4.13. As aberrations develop the dip between the primary peak and the first sidelobe moves below 50 % of the primary peak height causing a discontinuity in the FWHM. In devices with 45° detector mounting the defocus aberrations which cause the discontinuities are reduced to a second order effect. As we see later in figure 4.16, sidebands for such devices are not significant within the 1300 nm to 1900 nm wavelength range.

Shorter devices avoid the need for an angled detector plane. This is an illustration of the Rayleigh range: devices with larger ratio between focal length and device length

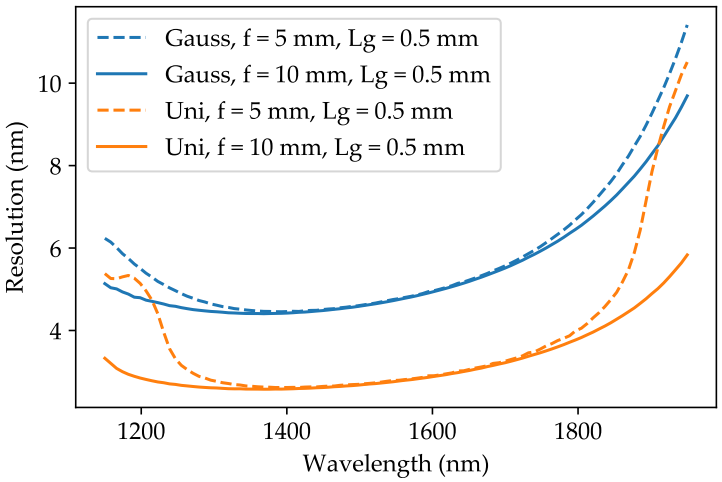

FIGURE 4.14: Resolution of Gaussian and uniform apodised gratings using a 45° detector plane. Though uniform gratings perform better at the design wavelength, Gaussian gratings are more robust to effects of focal plane curvature.

hold their beam waist over a longer distance. Though the devices with 45° degree detector planes preserve their peak resolution over a wider wavelength band the focal plane curvature eventually means the deviation from a flat focal plane is greater than the Rayleigh range of the device. Section 4.2.5 shows device bandwidth is often limited by reflectivity before aberrations become significant in devices with 45° detector planes.

Apodisation also has a significant effect on both the peak resolution and the overall resolution profile. Figure 4.14 shows that using a Gaussian apodised grating reduces the peak resolving power by a factor of approximately 1.7 when compared to a uniform grating of the same length, as such a Gaussian grating would need to be 1.7× longer than a comparable uniform grating to reach the same peak resolution. Apodisation reduces the effective length of the grating by reducing the contributions from the edges of the grating, as such a reduction in the peak resolution is to be expected. The Gaussian grating however does show less degradation in the resolution far from the design wavelength.

In the paraxial approximation we can use Fourier space propagation to describe the focussing of beams. For 'narrow' Gaussian beams the intensity cross section (perpendicular to the direction of propagation) is always Gaussian. This even holds for cross sections taken at small angles to the propagation axis. As such the cross section sampled by a fixed detector plane (even accounting for a curved focal plane) will still be Gaussian. Outside the Rayleigh range we would not expect a uniform grating to keep such a well defined profile, and it will rapidly develop strong sidelobes. This effect can be observed in figure 4.15. Far from the design wavelength of 1550 nm when focal plane curvature becomes prevalent the observed intensity profile from the Gaussian gratings (figure 4.15b) still have a Gaussian profile, with FWHM increasing from 22.6 µm at

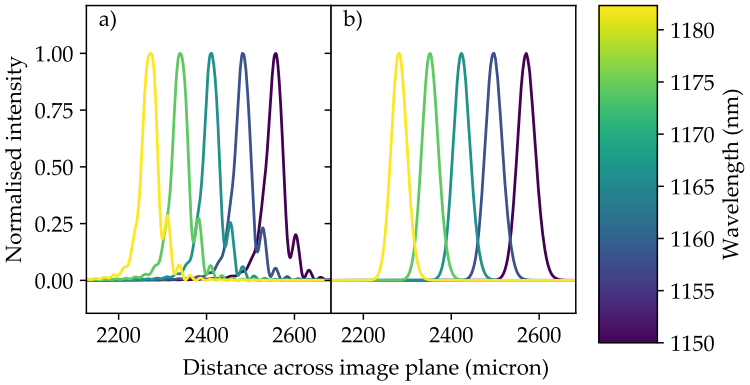

FIGURE 4.15: Comparison of intensity cross section far from the design wavelength at detector plane for a) Uniform grating b) Gaussian grating.

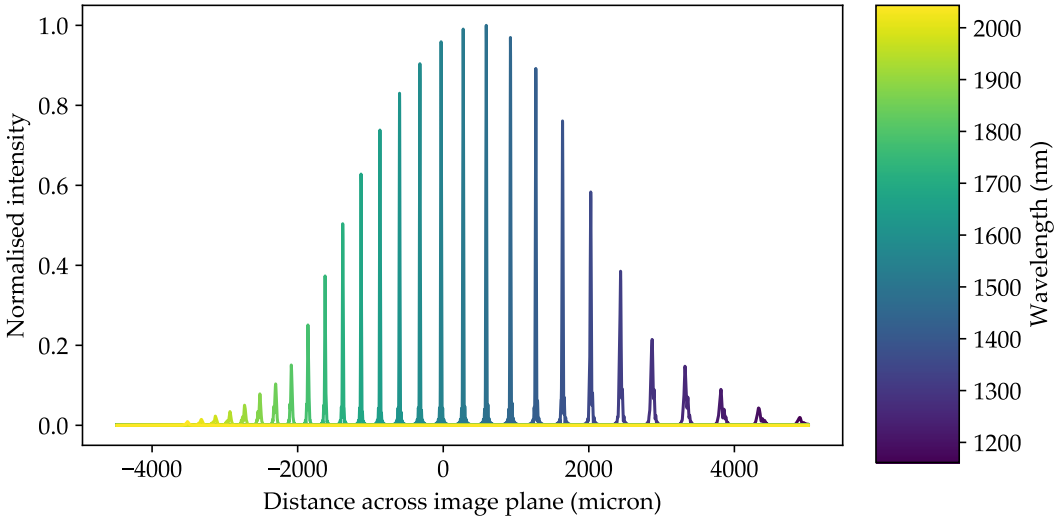

FIGURE 4.16: Device response over wide range of wavelengths. $L_g = 1\,\text{mm}$, $f = 10\,\text{mm}$.

1550 nm to 39 µm at 1150 nm. The intensity patterns for uniform gratings shown in figure 4.15a have significantly degraded, with the FWHM increasing from 13.2 µm at 1550 nm to 39 µm at 1150 nm.

4.2.5 Relative amplitude response and device bandwidth

The diffraction efficiency of blazed chirp Bragg grating devices is also important. It is pointless optimising the resolution of a device over a wide wavelength band if the output becomes negligibly weak when the input wavelength is tuned away from the design wavelength. Previous studies [13], [14] have shown that 45° degree blazed gratings have a much greater bandwidth than small angle devices, as such we would expect 45° blazed gratings spectrometers to operate over a much wider bandwidth than small angle devices.

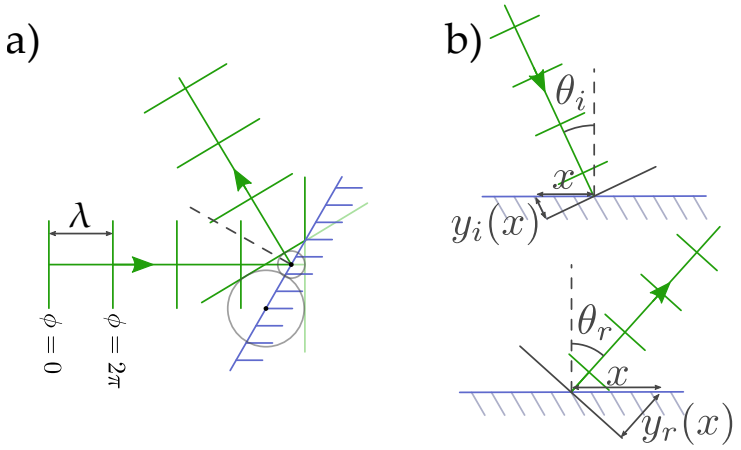

FIGURE 4.17: a) A reflected plane wave is constructed from the input plane wave using Huygens secondary sources. The incident and reflected angle are equal. b) Illustrations of plane wave incident on a reflecting surface and reflected wave leaving the surface, detailing the extra propagation distance y due to the angular offset.

Figure 4.16 shows that response of a blazed chirped Bragg grating modelled with the scalar diffraction model over a wide bandwidth, normalised to the peak reflection at the design wavelength. As the wavelength shifts from the design wavelength the device response gets weaker, limiting the bandwidth of the device. This is largely due to a vector phasematching condition between the blaze angle of the grating and the diffraction angle.

Typically when we think of light reflecting from a surface we consider the law of reflection

$$\theta_i = \theta_r, \tag{4.37}$$

where θ_i and θ_r are the incident and reflected angles relative to the normal to the reflecting surface. This makes intuitive sense, however it is not immediately clear what happens if the size of the reflecting surface is comparable to that of the wavelength of light. The law of reflection is often derived using a secondary source argument associated with Huygens: a plane wave can be constructed by placing a spherical wave source at every point along the phase front of the plane wave. Such a construction for reflection is shown in figure 4.17. If we consider a set of secondary sources along a reflecting surface of length L, we can calculate the phase delay between a wave hitting the surface, ϕ_i and the phase delay of another wave leaving the surface, ϕ_r, and then perform a phasor sum over the secondary sources with these phases. Such phases are given by

$$\phi_i(x) = kx\cos\theta_i, \tag{4.38}$$

$$\phi_r(x) = -kx\cos\theta_r. \tag{4.39}$$

The normalised phasor sum is then given by

$$R = \frac{\int_{-L/2}^{L/2} A(x) \exp\{[\mathrm{i}kx(\cos\theta_i - \cos\theta_r)]\}\,\mathrm{d}x}{\int_{-L/2}^{L/2} A(x)\,\mathrm{d}x}. \tag{4.40}$$

Note that the factor in the exponential resembles the 'obliquity factor' in the Fresnel-Kirchoff diffraction formula [7]. Taking $\theta_i = \theta_r$ trivially satisfies $R = 1$. For $L >> \lambda$ any $\theta_i \neq \theta_r$ results in a rapidly oscillating term which results in no observed reflection. For reflecting planes on the order of a wavelength the oscillating terms do not cancel out and the momentum matching condition has a width, with a narrower reflecting plane resulting in a wider momentum matching condition. As such one would expect the spectral bandwidth of a blazed Bragg grating to be set by the width of the waveguide, with narrower waveguides resulting in wider bandwidths. This is equivalent to the conclusions drawn when considering waveguide width in the beam propagation model. Figure 4.18 shows that reducing the waveguide width does indeed increase the width of the amplitude response of the device; in addition it shifts the wavelength of maximum diffraction efficiency. The diffracted field derived in equation 4.25 has a prefactor of k^2 which shifts the wavelength of maximum diffraction away from that predicted by vector phasematching (A grating blazed at 45° should be vector phasematched when diffracting light at the design wavelength of 1550 nm).

It should also be noted that the shape of the waveguide mode has not been considered in this argument, we have restricted input distributions to a single plane wave travelling along the waveguide axis. A waveguide mode can be deconstructed into a sum of plane waves travelling at different angles and phase offset to each other. Wide waveguide modes are comprised of plane waves over a narrow range of angles, while narrower waveguide modes have a much wider angular spread. The argument about momentum matching has considered a single input angle, if instead there is a range of input angles the device would momentum match over an even wider range of wavelengths. As such any estimates of bandwidths are conservative lower bounds and will increase when the effects of mode profile are added to the model.

The waveguide width in typical ssDUW devices for 1550 nm is between 6 µm and 6.5 µm depending on the wafer recipe. Figure 4.18 shows the integrated power (calculated with the scalar diffraction model) across the whole detector plane at different wavelengths for waveguides with different widths. As expected the wider the waveguide, the narrower the device bandwidth is, however the wavelength of most efficient operation also shifts with grating plane width. Even with a conservative estimate of 7 µm wide rectangular waveguides the spectrometer bandwidth is 210 nm for a design wavelength of 1550 Such devices are likely to easily satisfy the bandwidth required for Raman spectroscopy, and due to effects of mode shape could possibly satisfy the bandwidth requirements of OCT specified in section 1.3.

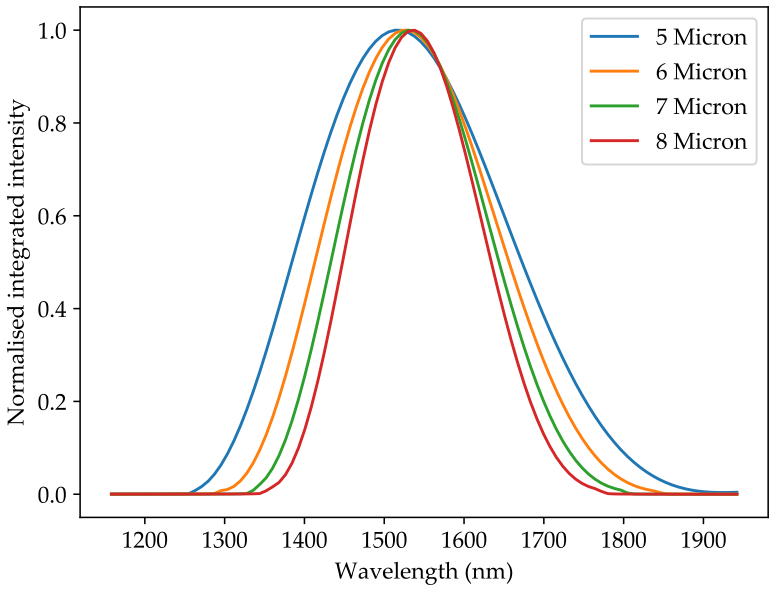

FIGURE 4.18: Modelling of peak and integrated strength of output at 45° detector plane, normalised to maximum. The width of the waveguide changes the width of greatest diffraction efficiency, as well as the bandwidth of the device.

4.3 Conclusions

This chapter has demonstrated three methods of modelling blazed chirped Bragg gratings, ray modelling, beam propagation modelling and scalar diffraction modelling. The ray model has been used for qualitative analysis of dispersion and aberrations, with ray intercept diagrams used to produce quantitative measures of aberrations. The beam propagation model has been used for fast modelling of the focal intensity profiles of devices and investigations of ideal detector mounting schemes. The scalar diffraction model has been used to model the resolution and bandwidth of devices with arbitrary detector mounting schemes, including effects due to waveguide width and blaze angle.

The results of the modelling from this chapter have also been used to derive some easy to digest findings. The length of a grating sets the peak resolution of a device, with the resolution inversely proportional to the device length. The ratio of focal length to grating length dictates the Rayleigh range of the focus, and how quickly focal plane curvature starts to degrade the resolution. Apodisation can be used to change the resolution response of the device, though using apodisation to increase the peak resolution of the device causes increased degradation of the resolution away from the peak.

For devices designed to focus light at 90° to the waveguide the detector should be mounted at 45° to the Bragg grating. A combination of wavelength dependent focal length and angular dispersion means that for small wavelength changes the grating will focus on this 45° plane. For larger wavelength ranges the rays diffracted by the device

fall outside of the paraxial approximation and the ideal focal plane curves. For a grating with $f{=}10L_g$ there is a wavelength band of 25% of the design wavelength within which focal plane curvature does not significantly affect the resolution.

The device bandwidth is set by the width of the waveguide; devices fabricated in substrates designed for operation at a 1550 nm wavelength had mode widths of 6 µm to 6.5 µm depending on UV fluence, which results in a 3 dB bandwidth of approximately 210 nm.

4.4 References

[1] P. J. Bock, P. Cheben, A. Delâge, J. H. Schmid, D. Xu, J. S., and T. J. Hall, "Demultiplexer with blazed waveguide sidewall grating and sub-wavelength grating structure," *Optics Express*, vol. 16, no. 22, pp. 17 616–17 625, 2008.

[2] Y. Hao, Y. Wu, J. Yang, X. Jiang, and M. Wang, "Novel dispersive and focusing device configuration based on curved waveguide grating (CWG)," *Optics Express*, vol. 14, no. 19, pp. 8630–8637, 2006.

[3] C. Koeppen, J. L. Wagener, T. A. Strasser, and J. DeMarco, "High resolution fibre grating optical network monitor," in *National Fibre Optic Engineers Conference*, 1998, Session 17 paper 2.

[4] C. K. Madsen, J. Wagener, T. A. Strasser, M. A. Muehlner, E. J. Laskowski, and J. DeMarco, "Planar waveguide optical spectrum analyzer using a UV-induced grating," *IEEE Journal of Quantum Electrononics*, vol. 4, no. 6, pp. 925–929, 1998.

[5] K. Okamoto, *Fundamentals of optical waveguides*, 2nd ed. Academic Press, 2006.

[6] S. A. Berry, "Ultra-high spatial and temporal resolution using scanning near-field optical microscopy," Ph.D. dissertation, 2013.

[7] M. Born and E. Wolf, *Principles of optics*, 7th ed. Cambridge University Press, 2019.

[8] J. L. Wagener, T. A. Strasser, J. R. Pedrazzani, J. DeMarco, and D. DiGiovanni, "Fiber grating optical spectrum analyzer tap," in *11th International Conference on Integrated Optics and Optical Fibre Communications and 23rd European Conference on Optical Communications*, vol. 5, 1997, pp. 65–68.

[9] J. W. Field, S. A. Berry, R. H. S. Bannerman, D. H. Smith, C. B. E. Gawith, P. G. R. Smith, and J. C. Gates, "Highly-chirped Bragg gratings for integrated silica spectrometers," *Optics Express*, vol. 28, no. 14, pp. 21 247–21 259, 2020.

[10] W. J. Smith, *Modern optical engineering*, 3rd ed. McGraw-Hill, 2000.

[11] J. Wyant and K. Creath, "Basic wavefront aberrations theory for optical metrology," in *Applied Optics and Optical Engineering XI*, Academic Press, 1992, ch. 1.

[12] B. Ramsay, E. Cleveland, and O. Koppius, "Criteria and the intensity epoch slope," *Journal of the Optical Society of America*, vol. 31, pp. 26–33, 1941.

[13] K. Zhou, G. Simpson, X. Chen, L. Zhang, and I. Bennion, "45° tilted fiber Bragg gratings," *Optics Letters*, vol. 30, no. 11, pp. 1285–1287, 2005.

[14] Y. Lu, W. Huang, and S. Jian, "Full vector complex coupled mode theory fortilted fiber gratings," *Optics Express*, vol. 18, no. 2, pp. 713–726, 2010.

Chapter 5

Blazed Bragg Gratings with Aberration Correction

Experimental devices are essential in assessing whether models accurately predict actual device performance. They also allow easy analysis of effects that are difficult to model such as: do we expect grating phase errors to cause significant aberrations, will the signal reflected from the grating be sufficient to detect with typical grating refractive index modulation?

Devices fabricated to undertake such experimental observations need not be at the same wavelength as final devices of interest. Prior to the work presented in this thesis another researcher in the group, Matthew Posner, had developed a 45° degree blazed Bragg grating platform at 1550 nm for integrated polarisers. This meant that FHD substrates and an interferometer board for grating writing were already in existence. In addition, the research group also possesses a large amount of characterisation equipment at 1550 nm, including a narrowband laser tunable over a wide wavelength range and a linear 1550 nm camera. With this development and infrastructure in place, it was decided to undertake initial investigations at 1550 nm to utilise these advantages, however due to the prohibitive cost of detectors at 1550 nm, integration with detectors was not considered. Instead it was chosen to investigate the properties of the grating solely as a diffractive lens. Later work (chapter 6) aims to address this by moving integrated devices to 780 nm where low-cost detectors are available, attractive for a real-world demonstrator.

This chapter presents the results of two system architectures: devices fabricated with linear period chirp and those implementing the correction of coma. The findings from these devices have formed the basis of a number of conference presentations [1], [2] and a peer-reviewed journal publication [3]. Methods of fabrication and characterisation are presented, and results are compared against models generated in the previous chapter to investigate the fidelity of models compared to actual devices.

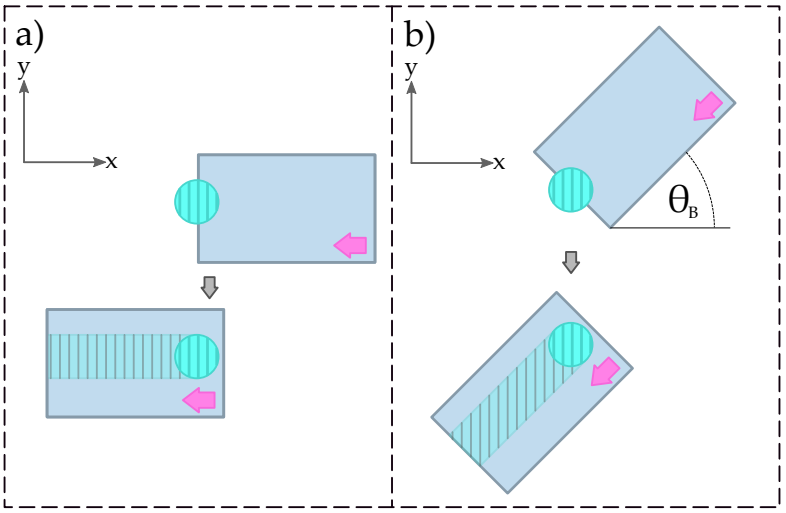

FIGURE 5.1: Sample translation in unblazed (a) and blazed (b) grating writing. Sample translation direction shown in pink. a) In non-blazed Bragg grating writing the sample is translated (in the x direction) through a stationary writing spot while phase control is applied to the writing beams. b) To write blazed gratings the sample is rotated by the blaze angle before writing, and translated in both x and y.

5.1 Linearly chirped devices

As mentioned in previous chapters, the linear period chirp scheme was first presented by Wagener et al [4] in small blaze angle devices. A highly chirped, 45° blazed device was fabricated as an initial proof of concept of the scheme in an FHD platform. The investigation into linearly chirped devices occurred prior to the development of any of the models presented in chapter 4. As such the aberrations arising from linear period chirp were not known about beforehand. This device prompted modelling work to understand the aberrations present in blazed Bragg grating spectrometers.

5.1.1 Device design and fabrication

Blazed Bragg gratings can be fabricated in the ssDUW scheme by rotating the substrate prior to waveguide writing. A waveguide is then written by moving a combination of the x and y axes of the stage as shown in figure 5.1; in the reference frame of the chip this is equivalent to rotating the writing spot and moving it across the surface of the chip. The grating period of interest, δ, is set by the fringe period from the interferometer, Λ, and the blaze angle, θ_B (as shown in figure 4.2). Blazed Bragg gratings require a different interferometer period than that of unblazed Bragg gratings, which can be calculated using equation 4.2, resulting in:

$$\Lambda(\theta_B, \theta_o) = \frac{\lambda \cos\theta_B}{n_e(\cos\theta_o - 1)}. \tag{5.1}$$

Design Wavelength	1550 nm
Central grating period (δ)	1070.4 nm
Chirp rate ($\mathrm{d}\Lambda/\,\mathrm{d}z$)	69.2 nm/mm
Blaze angle	45°
Central diffraction angle	90°
Grating Length	1 mm
Waveguide refractive index	1.4481
Waveguide distance from side facet	2 mm
Apodisation	Uniform

TABLE 5.1: Parameters for linearly chirped device

As such an interferometer board with a period of 758 nm is required to fabricate 45° blazed devices that diffract light at 1550 nm at 90° to the waveguide, compared to a period of 536 nm for unblazed gratings at 1550 nm.

Gratings which create a focus require a change in δ across the grating. This can be achieved by varying Λ by the detuning method described in chapter 2 but also by changing θ_B along the device. In this chapter we will limit investigations to fixed θ_B, though work in chapter 6 considers devices varying both Λ and θ_B. The discussion of period detuning in chapter 2 was presented in the context of fixed period gratings with different Bragg wavelengths, however it is equally applicable to gratings with period chirp. The design of such a grating is controlled using software and as such allows significant design space for devices. The limit of chirp rate is not something which has been experimentally tested, it is expected that AC refractive index modulation of chirped gratings will not be significantly lower than corresponding gratings of the same period unless the change in period over a single writing spot width is comparable to the grating period itself

$$w\frac{\mathrm{d}\Lambda}{\mathrm{d}x} << \Lambda(x), \tag{5.2}$$

where w is the width of the writing spot measured perpendicular to the grating fringes. The other important limit when considering chirped gratings is the detuning bandwidth; the 3 dB detuning bandwidth is approximately 10 % of the grating period due to waveguide geometry (as described by equation 2.7). To verify the assumptions of chirp rate it was decided to fabricate a 1 mm grating with a high chirp rate ($\mathrm{d}\Lambda\,/\,\mathrm{d}x$) of 69.2 nm/mm, a higher chirp rate than was expected to be required for 'optimal' spectrometer devices. The fabrication parameters are given in table 5.1. The chip was designed such that focus would be formed $\approx$ 1 mm outside the planar layer of the chip in free space. This simplified characterisation using the camera system, and was more likely to yield useful information if the device did not function as intended.

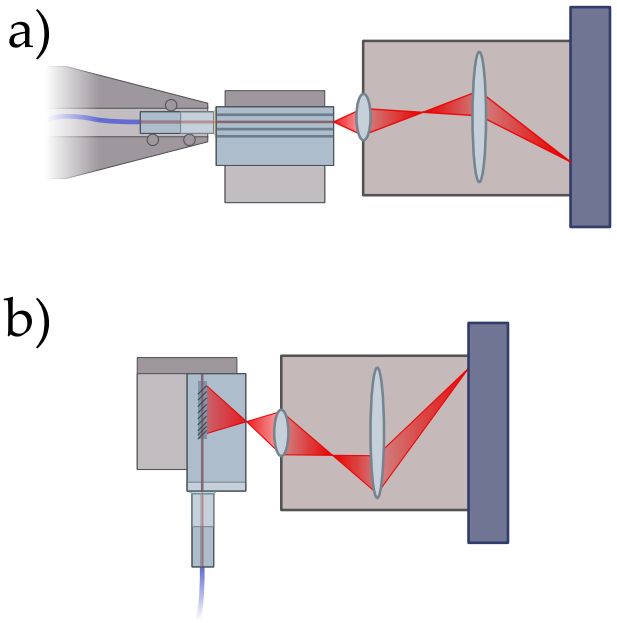

FIGURE 5.2: Sample mounting geometry of the NA characterisation system. a) Typical sample mounting geometry for NA characterisation. b) Side mounted sample with glued fibre v-groove for blazed grating focus characterisation.

5.1.2 Characterisation

Characterisation of devices was performed by coupling light into devices and imaging the light coupled out of the side facet (as shown in figure 5.2b). The numerical aperture (NA) characterisation system was used as an imaging system; the camera in the system (Raptor Photonics OW1.7-VS-CL-640) was sensitive to light between 400 nm and 1700 nm so could be used to characterise the spectral properties of the device. The imaging system also contained a pair of lenses providing 57× magnification, which allowed the intensity pattern of the device to be sampled at a much higher spatial resolution (the pixel pitch of the camera is 15 µm, which is comparable to the FWHM of the intensity pattern in the detector plane). The NA characterisation system was originally designed to characterise the channel waveguides and modes of 20 mm × 10 mm chips. Translation stages are typically used to optimise the coupling into the chip while imaging the mode, as shown in figure 5.2a. Blazed chirped Bragg grating devices operate in a different geometry to typical waveguide devices characterised with the NA measurement system (as shown in figure 5.2), with light output from the chip at 90° to the input waveguide. It was not possible to alter the input coupling stages of the NA system, as it is used regularly by many other researchers, instead a V-groove was glued to the device using UV-cured glue before characterisation.

A 0.5 pm linewidth tunable PM laser (Agilent 81600B) was fibre coupled into the V-groove and the output intensity pattern through the device was imaged as the input

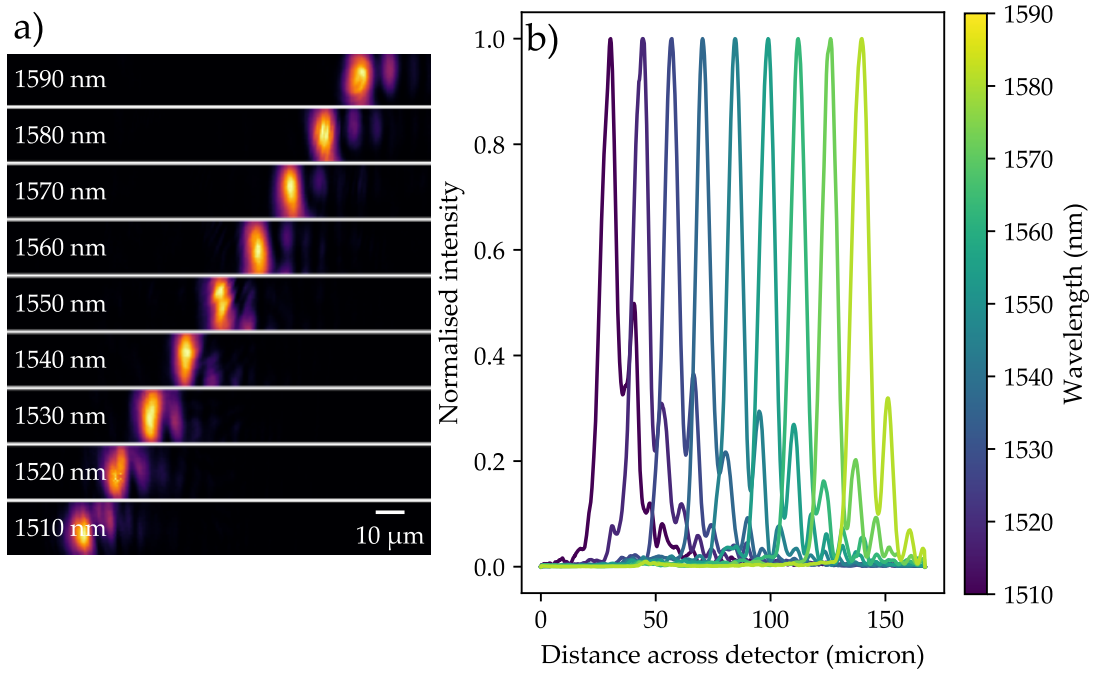

FIGURE 5.3: a) Composite of normalised camera images with different input wavelengths. As the wavelength changes the focal spot moves sideways across the camera. b) Plot of vertical sum of intensity patterns at different wavelengths.

wavelength was changed. The linewidth of the laser is much less than the expected spectrometer resolution ($\sim 1\,\text{nm}$), as such the tunable laser approximates a single wavelength source for the purposes of characterisation. The detected intensity pattern was converted into an image by the camera, with automatic control of gain and exposure; the gain and exposure have not been calibrated. The spectral resolution can be calculated from image data. The device was characterised between 1510 nm and 1590 nm, which corresponded to the focal spot moving from one side of the image sensor of the camera to the other.

5.1.3 Results and analysis

The tunable laser was used to perform a wavelength sweep of the device, the results of which are shown in figure 5.3. The output intensity pattern of the device moves across the camera (left to right) as the input wavelength is increased. The intensity pattern is well localised, however does possess sidelobes (on the high wavelength side). The spot is much taller than it is wide; the device was designed to focus outside the planar waveguide so it has diffracted in the vertical direction, while focusing in the horizontal direction.

A first order polynomial was fitted to the centre position of each focal spot and regression was used to calculate the spatial dispersion, which was found to be $1.400 \pm 0.006\,\mu\text{m/nm}$. The small standard deviation suggests a linear model is a good fit within this wavelength

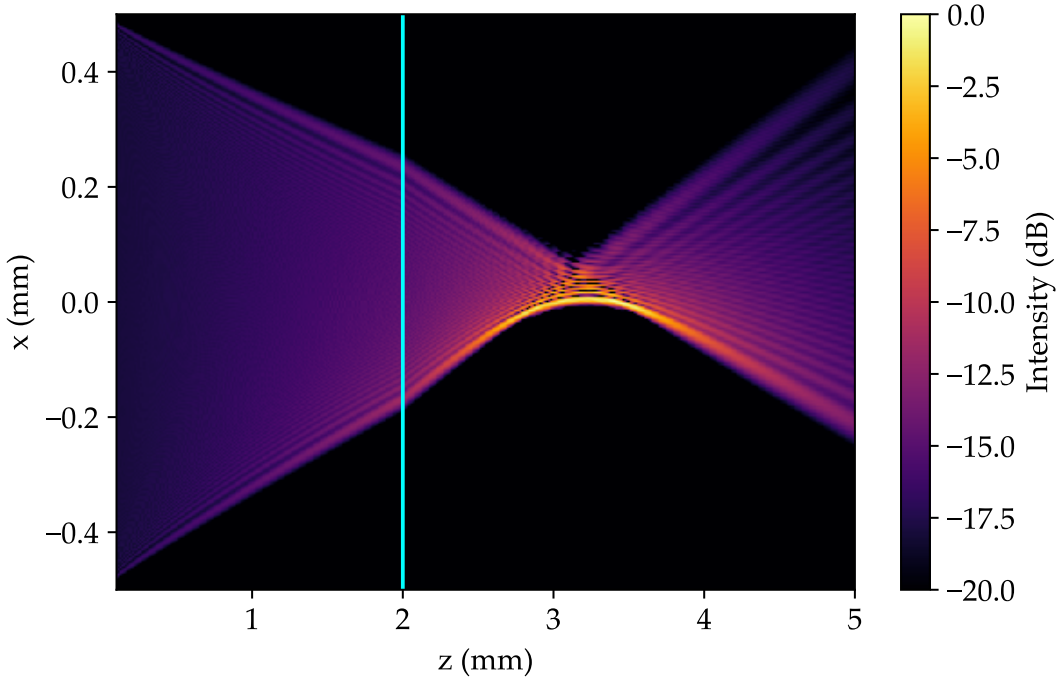

FIGURE 5.4: Modelled intensity pattern of first device showing coma aberration (with an input wavelength of 1550 nm. Glass air interface marked by cyan line.

range. This confirms results from 4, linear dispersion is expected over a wavelength range $\Delta\lambda$, provided $\Delta\lambda \ll \lambda_0$, where λ_0 is the design wavelength.

The Houston resolution was calculated by fitting a Gaussian distribution to the primary peaks (and subsequent sidelobes) shown in figure 5.3. The average peak width was $7.8\,\mu\text{m} \pm 0.4\,\mu\text{m}$, resulting in a resolution of $5.6\,\text{nm} \pm 0.3\,\text{nm}$.

Both the ray model and the beam propagation model were used to investigate the output of the device. The focus at 1550 nm can be seen in figure 5.4. Although the ratio of chip length to focal length is large (and therefore modelling errors due to paraxial approximations are expected) the position and shape of the intensity pattern modelled using the beam propagation method agree with results from ray tracing. The scalar diffraction model could not be used because of the refractive index interface from the edge of the chip. The shape of the intensity pattern matches coma aberrations seen in experimental results: a strong central peak with lobes on the high wavelength side, however the focal length and dispersion do not agree with observed values. This is attributed to undocumented changes to parameters in fabrication code after device fabrication.

Both the ray model and beam propagation model with the parameters listed in table 5.1 predict a focus approximately 1.2 mm from the side facet of the chip, as shown in figure 5.4. Such a device would exhibit a spatial dispersion of 2.7 µm/nm, significantly higher than the value measured. In addition the distance from the edge of the chip to the focus disagrees with the vertical extent of the focal spot. Outside the chip the

vertical component of the mode is free to diffract. Starting with a mode of approximately 5.6 µm (measured mode size for a PX14 waveguide with a fluence of 14 kJ/cm^2), 1.5 mm of propagation outside the chip would be required before the mode reached the correct vertical width of 139.8 µm.

To prevent further errors in grating fabrication parameters, firing positions were generated in modelling code and passed to fabrication code using a data file. This meant that firing positions of future devices were all modelled before fabrication and stored in multiple locations. In addition automated logging was implemented into grating writing code, keeping a record of device parameters and waveguide coordinates. This was successful in later devices, devices fabricated in section 5.2 were modelled approximately 12 months after fabrication when models had been developed.

This device confirmed that spectrometer operation was possible over a much wider band than was shown in the small angle scheme, at the cost of lower peak resolution. The next section investigates the achievable resolution after correction of aberrations, as well as fabrication limits of devices.

5.2 Coma-corrected devices

A nonlinear period chirp function (discussed in section 4.2.1) was designed to produce foci without aberrations, which should result in a marked improvement from the resolution shown by the linearly chirped device. Again the device was designed to focus into free space to simplify characterisation; the nonlinear period function had to be modified to account for the refraction from the facet and subsequent free space propagation. This new nonlinear period does not have a closed-form solution, however it can be calculated numerically and is shown in figure 5.5a. As previously shown in section 4.2.1 an unaberrated focus requires a higher rate of chirp at the edges of the grating than the linear chirp approximation. In a grating which focuses outside the planar layer refraction at the facet causes rays to propagate at a steeper angle, reducing the focal length. As such a device focusing outside the planar waveguideing layer requires less chirp than one with a similar focal length in glass. Figure 5.5b shows the layout of a device implementing coma correction, with a grating 0.65 mm from the side facet. The device is designed to bring light to a focus 5.5 mm from the waveguide using a 1 mm uniform apodised grating. A longer focal length was used to reduce the effects of focal plane angle and curvature, as the imaging system made use of an angled detector plane difficult and it was not possible to integrate detectors at 1550 nm.

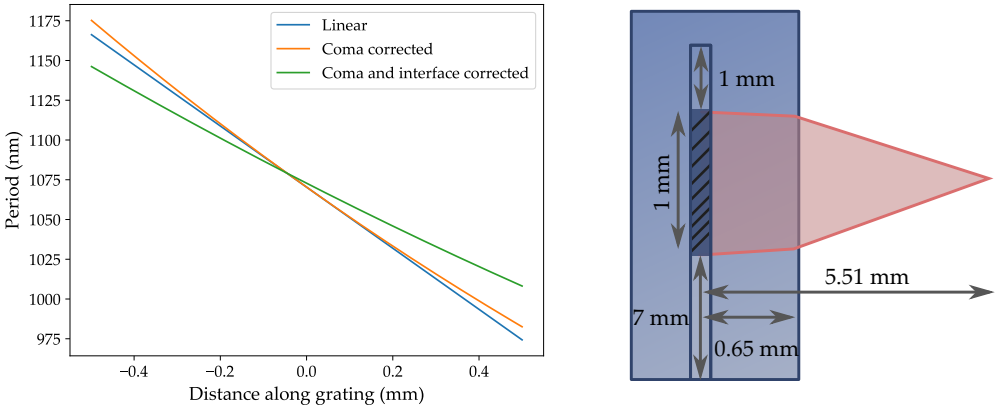

FIGURE 5.5: a) Plot of period function used to fabricate device, compared against linear chirp and period ignoring interface diffraction for the same focal length. b) Diagram of layout of coma corrected chip

5.2.1 Characterisation

The device did not possess significant aberrations at the detector plane and device wavelength, implying successful correction of coma aberrations. The position of the focal plane was between 5.4 mm and 5.7 mm from the grating, a precise distance was hard to identify as the intensity pattern at the focus was relatively constant across the beam waist. The detector plane was set 5.5 mm from the waveguide and grating. The device was characterised over a much wider bandwidth (1468 nm to 1630 nm, sampled at 1 nm increments) than the linearly chirped device. To allow this the camera (and associated imaging system) were translated sideways at various points throughout the experiment. The camera position was recorded using a micrometer translation stage, in addition it was ensured that significant overlap existed in the wavelength ranges at each camera position to confirm the lack of positional errors.

Figure 5.6 shows a number of images of device output taken at different wavelengths; the foci was significantly outside the planar layer of the device resulting in significant divergence in the vertical direction. The stripe overfilled the lens in the vertical axis, resulting in a lens-flare which changed angle as the intensity pattern moved across the camera, this is highlighted with a green ellipse in the data in figure 5.6. Aside from aberrations due to the imaging system, the output possessed small sidelobes on the left side of the primary intensity peak when the input wavelength was below the design wavelength of 1550 nm, and on the right side when the input wavelength was above 1550 nm. Such sidelobes are due to coma; though it is possible to remove aberrations at a single wavelength, it is not possible to correct aberrations at all wavelengths. The sidelobes due to coma outside the design wavelength has also been exacerbated by the

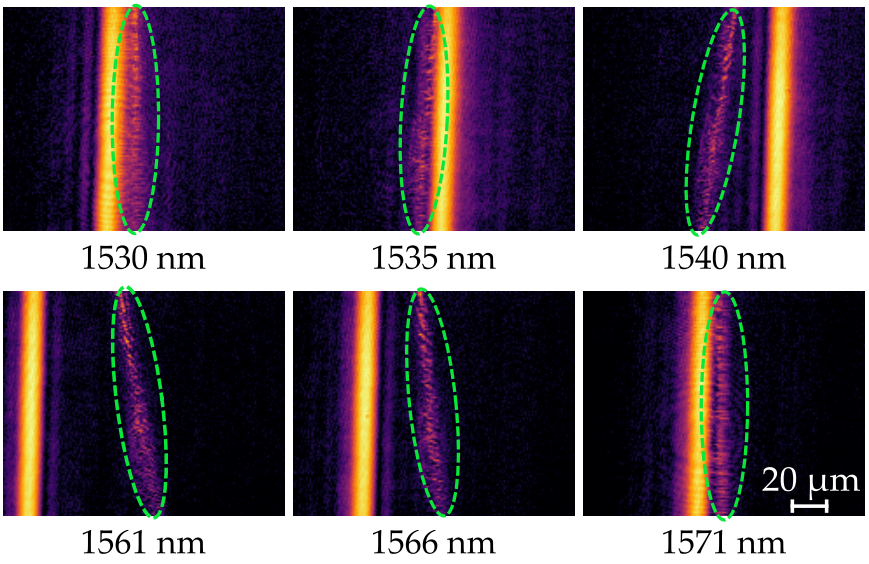

FIGURE 5.6: Images of the spectrometer output showing wavelength dependent sidelobes and lens-flare. Images on the same row were taken with the same camera position. Lens-flare highlighted with a green ellipse.

choice of focal plane: when a 45° detector plane is used to analyse the device the effects of coma are relatively minor (as shown in section 4.2.3).

The 2D image data was condensed to a 1D intensity array by summing columns of pixel values. The shape of the intensity pattern did not change over the vertical axis of the image, so this did not change the measured resolution, however it did act to average out noise artefacts. A narrow section in the middle of the camera was removed from every data set to avoid the effects of the lens flare; any images with their principle intensity peak in this central region were discounted from the data set. Overlaps in wavelength data, to prevent issues when moving the camera, filled the majority of gaps left by removing data due to lens flare.

The centre position and FWHM of the intensity profiles were extracted using a fitting algorithm. A sum of up 4 Gaussian peaks were fitted to the intensity distribution such that the first Gaussian fits to the primary intensity peak and subsequent Gaussians fit to the lobes. This fitting routine fitted well to the data (as shown in figure 5.7) both with and without sidelobes. The width of the primary lobe was approximated by the width of the central peak; the overlap between the primary peak and the first sidelobe was typically small.

5.2.2 Results and analysis

Figure 5.8 shows device operation over a large wavelength band. This device shows none of the fringing characteristic of coma aberrations at the design wavelength, and displays relatively linear spatial dispersion. The change in the intensity profile with wavelength

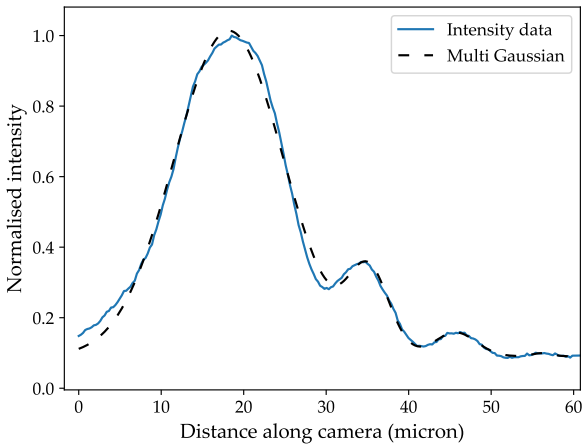

FIGURE 5.7: Summed image data, fitted with the sum of 4 Gaussian peaks.

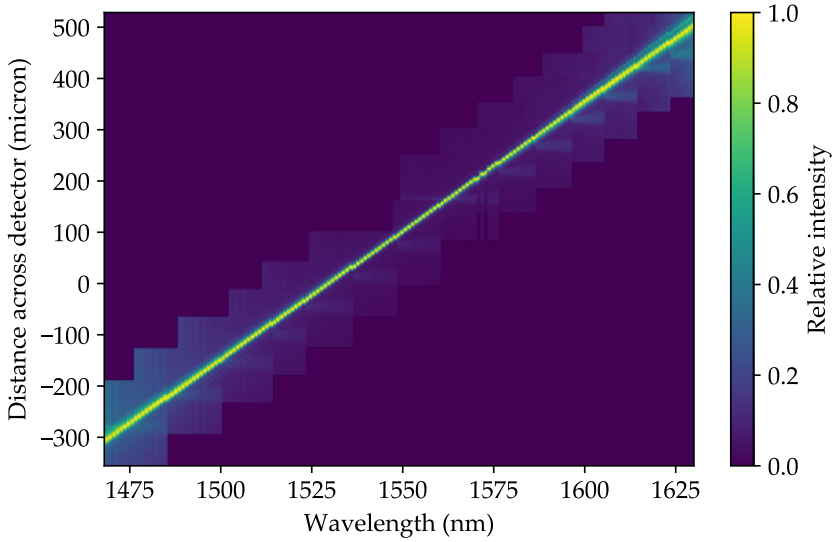

FIGURE 5.8: Composite of detector plane intensities (constructed from vertically summed images and stitched together using measured camera position) for the coma-corrected device. Lens flare has not been removed from this data set. Data points at extreme edges had a lower signal to noise ratio, amplification of background noise can be seen as a set of overlapping squares across the diagonal.

appears relatively minor, with widening and sidelobes at the extreme wavelength edges of the data set, however replotting the data against the distance from the peak intensity at each wavelength (as shown in figure 5.9) makes the aberrations easier to see. There is a broad central intensity peak, which becomes wider and asymmetric at wavelengths above 1580 nm or below 1510 nm. Sidelobes can clearly be seen above and below the primary peak for above and below the design wavelength respectively. We would expect no sidelobes for the design wavelength of 1550 nm, instead 1560 nm seems to be free of sidelobes and there are minor sidelobes below the primary peak at 1550 nm. Ray modelling suggests that this could be caused by a discrepancy in the waveguide effective

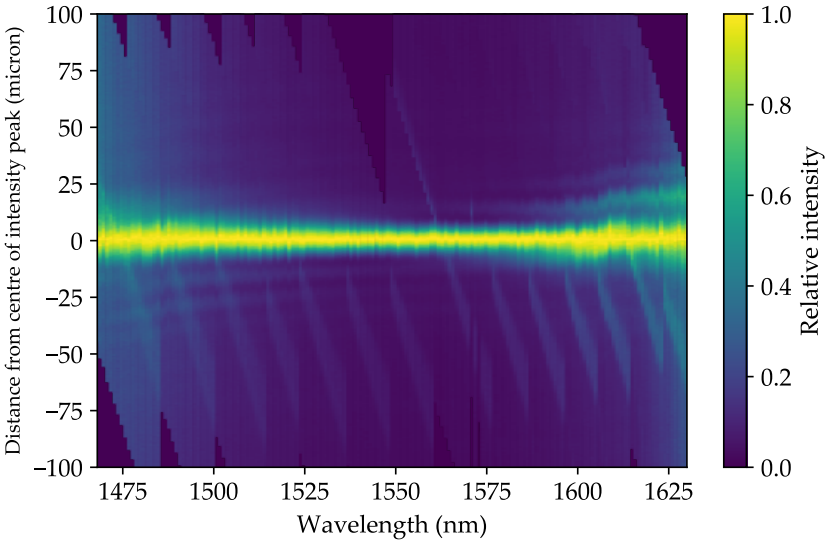

FIGURE 5.9: Composite of detector plane intensities for coma-corrected devices centred at the peak intensity. Lens flare has not been removed from this data set.

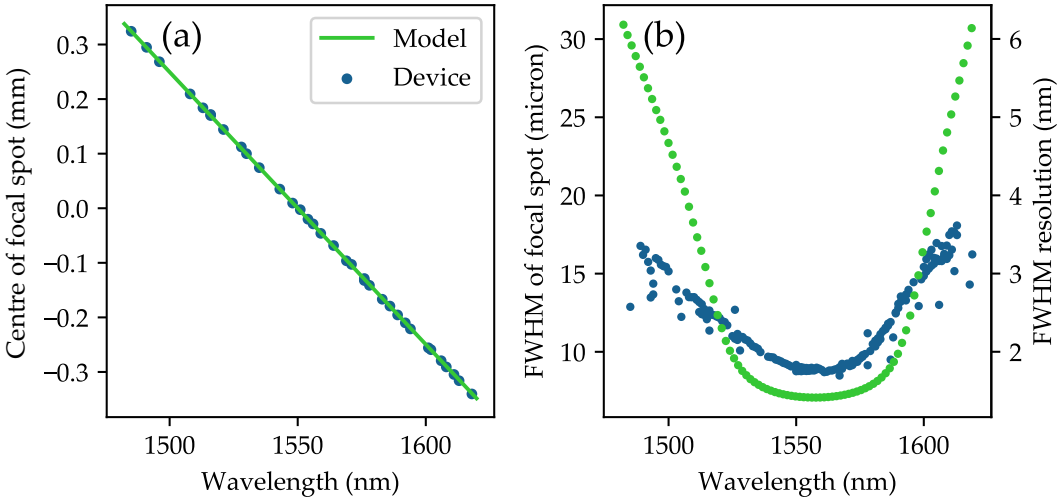

FIGURE 5.10: a) Centre position of intensity pattern for device and modelling. b) FWHM and resolution of intensity pattern for device and modelling.

index. Shifting the modelled effective index to 1.454 causes 1560 nm to have a focus free of coma, while 1550 nm exhibits small amounts of coma.

The resolution characteristics of the device were calculated using the dispersion and spot widths and compared to modelling. Figure 5.10a shows that the measured focal position of the fabricated device agrees almost exactly with that of the modelled device, and the dispersion is approximately linear across the device with a value of 5.00 µm/nm. The constant dispersion across the wavelength band means that the resolution is directly proportional to the width of the intensity pattern at the detector plane, figure 5.10b shows the width and resulting resolution. Though the dispersion of the modelled and

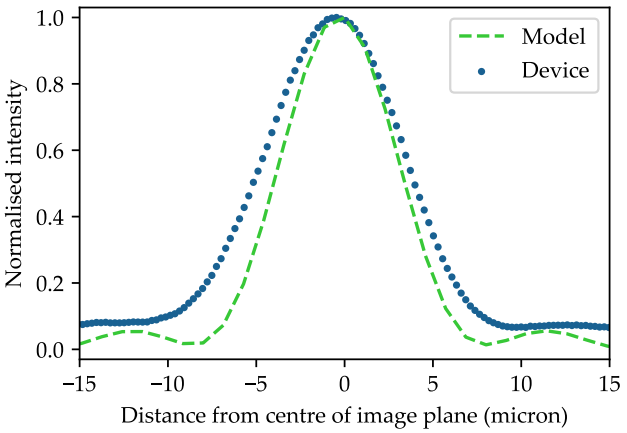

FIGURE 5.11: Spot profile in detector plane for fabricated device and modelling (for a uniform apodised grating). Fabricated device shows no sidelobes and wider focal width.

fabricated devices match very well, the width of the focal spot is a very poor match. The modelled resolution is much higher at the design wavelength, and away from the design wavelength the modelled resolution reduces at a much faster rate than the fabricated device.

The intensity profile of the device had a Gaussian-like response with a FWHM of 8.8 µm at 1560 nm, resulting in a peak resolution of 1.8 nm. Away from this wavelength the resolution worsened, with value of 3 nm within a 100 nm bandwidth of the design wavelength. The peak resolution was expected at 1550 nm, however, if the detector deviates between the design and the measured position the wavelength with optimum resolution will change (due to the angled focal plane effect). Modelling using the beam propagation model shows a central wavelength shift with focal plane position of 0.19 nm/µm.

The poor match between modelling and reality can be explained by the intensity profile of the focal spot. Figure 5.11 shows the summed intensity distribution at the focal spot (at a single wavelength), and is compared to the intensity distribution expected for a uniform grating. A uniform grating should produce a narrower, sinc^2 intensity profile at the focal plane, which corresponds with the output of the modelled device. Instead the device output shown in figure 5.11 has little or no sidelobes and looks considerably Gaussian-like. Again, from a Fourier transform relationship this implies that the refractive index modulation envelope of the device is Gaussian-like and is considerably stronger at the centre of the device than the edges. This is also supported by the resolution behaviour away from the design wavelength. As found in section 4.2.4 the resolution of a Gaussian grating is stable over a much wider wavelength band than a uniform grating (due to beating between component Gaussian modes in a uniform focusing device).

The duty cycle of the fabricated blazed Bragg grating was constant, which should result in a uniform apodised grating. However detuning the period of a grating from the design wavelength of the interferometer used to fabricate the grating (to produce period chirp)

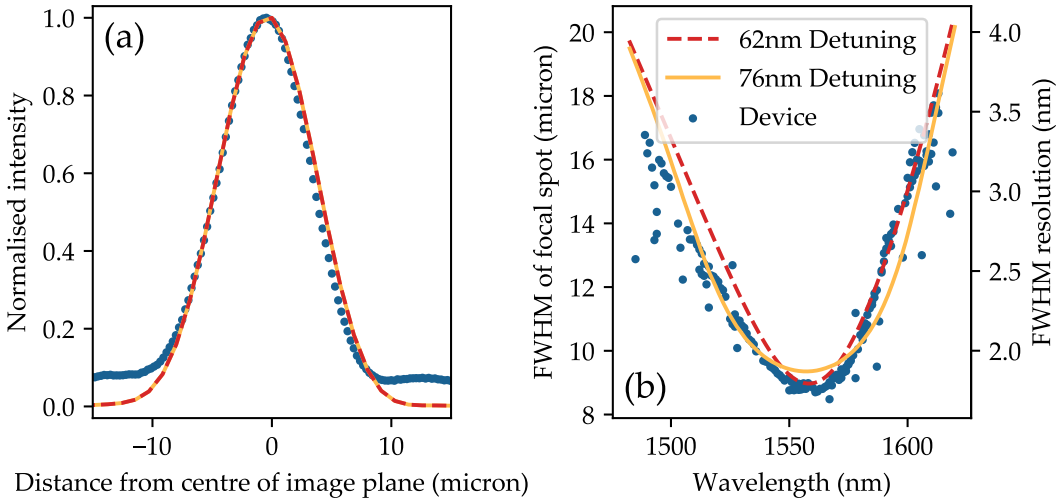

FIGURE 5.12: a) Spot profile in detector plane for fabricated device and uniform grating with detuning correction. b) resolution curves for fabricated device and grating detuning curves of various widths

will result in a reduction in refractive index modulation, as described in section 2.3.2. The detuning of the 758 nm period interferometer board has not been directly measured, but can be estimated using the detuning bandwidth of the 532 nm interferometer board used to fabricate unblazed Bragg gratings at 1550 nm, giving $\Lambda_{3dB} = 76$ nm.

Using this value we can account for the induced apodisation, the results of this model are given in figure 5.12. The detuning curve corrected detector plane intensity (shown in figure 5.12a) matches the device almost perfectly, and the modelled resolution (shown in figure 5.12b) matches the device very well over a 100 nm bandwidth. It was found that a far closer match occurred with a 62 nm detuning curve width than with a 76 nm detuning curve. A number of explanations have been suggested for this discrepancy. Poor alignment of the ssDUW system can change the overlap between the UV writing spots, which can artificially widen the detuning curve. The detuning curve width could be correct and there could be another effect reducing the diffraction efficiency at the edge of the grating (poor vector phasematching at the edge of the grating for example).

The modelled data and device resolution shown in figure 5.12b match well above the design wavelength, however there is a small discrepancy below the design wavelength. As earlier stated, changing the modelled position of the detector plane shifts the resolution curve in wavelength at a rate of approximately 0.19 nm/µm. The discrepancy in the resolution curve could be caused an angular misalignment of the camera for the measured results. The maximum wavelength discrepancy between fitted and measured results of the same resolution is 10.4 nm, which would be resolved with a focal plane shift of 55 µm. Over the whole measured detector plane this require an angular misalignment of 5.7°. The imaging system and chip were aligned before measurements by bringing the facet of the chip into focus, and adjusting the angle of the chip so the facet stayed in focus while

the camera was translated laterally. Such a large angular misalignment would have been corrected for by this alignment procedure, therefore the cause of such an effect (though small) is as of yet unknown. It is possible that a parameter optimisation over detector plane position, detuning width and n_{eff} would account for this discrepancy.

5.3 Conclusions and further work

This chapter showed the first results of the 45° blazed chirped Bragg grating platform at 1550 nm. A linearly chirped spectrometer was shown with a period chirp rate of 69.2 nm/µm, far in excess of any other reported blazed chirped Bragg grating spectrometers shown in literature. The linear chirp resulted in linear coma, which resulted in a relatively low resolution of 5.6 ± 0.3 nm. Modelling confirmed the presence of linear coma, but was unable to replicate the exact characteristics of the device, suggesting a shorter focal length, and possibly an even higher rate of chirp was actually fabricated.

Devices with a nonlinear period function to correct for linear coma were designed and fabricated. Devices achieved a peak resolution of 1.8 nm at 1560 nm, a typical resolution of 2.6 nm over a 100 nm bandwidth and operation across the whole wavelength of the tunable laser used for characterisation (1440 nm to 1640 nm). The output at the edges of the grating were weaker than designed, modelling suggests that the rate of chirp resulted in a near Gaussian apodisation due to the limited grating detuning bandwidth.

These results show that the spectrometer scheme is fabricable, produces measurable output and achieves the goal discussed in chapter 1 of combining the wide operation bandwidth shown by Bock et al. [5] as well as the higher spectral resolution shown by Madsen et al. [6]. To achieve the full requirements specified in section 1.3 the design wavelength of the device must be changed to 780 nm, as well as further increasing the resolution.

Though resolution was investigated in detail in this chapter, the 3 dB bandwidth was very difficult to measure. In addition the resolution was far from optimal due to the choice of parallel detector planes. Future work will aim to address these issues by attempting to integrate detectors with devices. Chapter 6 makes initial steps towards this by moving devices to 780 nm to utilise low-cost silicon detectors, ripe for integration. In addition it investigates methods to avoid the detuning based apodisation seen in this chapter by varying the blaze angle across the blazed chirped Bragg gratings. Such methods will enable devices with increased length, which will result in higher resolution and increased power coupling out of devices.

5.4 References

[1] J. W. Field, M. T. Posner, S. A. Berry, R. H. S. Bannerman, J. C. Gates, and P. G. Smith, "Fabricating a prototype spectrometer using a large-angle direct UV-written chirped tilted grating," in *Advanced Photonics 2018 (BGPP, IPR, NP, NOMA, Sensors, Networks, SPPCom, SOF)*, Optical Society of America, 2018, BW2A.4.

[2] J. W. Field, S. A. Berry, R. H. S. Bannerman, D. H. Smith, J. C. Gates, C. B. E. Gawith, and P. G. R. Smith, "Miniaturised, planar, integrated Bragg grating spectrometer," in *2019 Conference on Lasers and Electro-Optics Europe European Quantum Electronics Conference (CLEO/Europe-EQEC)*, 2019.

[3] J. W. Field, S. A. Berry, R. H. S. Bannerman, D. H. Smith, C. B. E. Gawith, P. G. R. Smith, and J. C. Gates, "Highly-chirped Bragg gratings for integrated silica spectrometers," *Optics Express*, vol. 28, no. 14, pp. 21 247–21 259, 2020.

[4] J. L. Wagener, T. A. Strasser, J. R. Pedrazzani, J. DeMarco, and D. DiGiovanni, "Fiber grating optical spectrum analyzer tap," in *11th International Conference on Integrated Optics and Optical Fibre Communications and 23rd European Conference on Optical Communications*, vol. 5, 1997, pp. 65–68.

[5] P. J. Bock, P. Cheben, J. H. Schmid, A. V. Velasco, A. Delâge, S. Janz, D. Xu, J. Lapointe, T. J. Hall, and M. L. Calvo, "Demonstration of a curved sidewall grating demultiplexer on silicon," *Optics Express*, vol. 20, no. 18, pp. 19 882–19 892, 2012.

[6] C. K. Madsen, J. Wagener, T. A. Strasser, M. A. Muehlner, E. J. Laskowski, and J. DeMarco, "Planar waveguide optical spectrum analyzer using a UV-induced grating," *IEEE Journal of Quantum Electrononics*, vol. 4, no. 6, pp. 925–929, 1998.

Chapter 6

780 nm high resolution spectrometer fabricated using rotation transformations

Demonstration of a compact integrated spectrometer scheme suitable for both Raman spectroscopy and OCT requires high bandwidth (150 nm) and high-resolution (0.35 nm) operation at 780 nm wavelengths. Highly chirped blazed Bragg gratings have been shown as a viable solution to this problem, however the operation wavelength of devices needs to be shifted from 1550 nm (as demonstrated in chapter 5) to 780 nm while increasing the resolution.

The shift in design wavelength required development of a new planar wafer recipe, the development of which is shown in chapter 3. To increase the spectral resolution (compared to devices shown in chapter 5) a solution to the unintended apodisation due to grating detuning bandwidth must be found. Equation 4.29 shows that longer gratings result in higher resolution, however equation 4.28 shows that longer gratings also require more detuning bandwidth to achieve the same focal length, as the focal length is set by the rate of chirp. It is possible to increase the device focal length to reduce the required chirp, however this will also increase the footprint of the device. Instead this chapter presents an alternative method by which the blaze angle of a grating is varied along its length, reducing the requirement for period chirp without compromising footprint. At the same time the fabrication wavelength of devices is changed from 1550 nm to 780 nm to accommodate low-cost detectors and work towards a fully-integrated prototype. The work shown in this chapter was presented at the SPIE Photonics West conference in 2020 [1] and to our knowledge provides the first demonstration of Bragg gratings with variable blaze angle.

To implement a variation in the blaze angle along the length of the device a C++ software library was designed to streamline the creation of complex ssDUW structures,

as well as implementation of rotation transformations. An investigation into fabrication and alignment tolerances on rotation transformations was performed, and a number of devices were fabricated and characterised to test the variable blaze angle scheme and to show viability of spectrometer devices at 780 nm.

6.1 Variable blaze angle

The focal length of a blazed chirped Bragg grating is often discussed in terms of $\mathrm{d}\Lambda/\,\mathrm{d}x$, as Λ tends to be the parameter controlled during fabrication processes. The diffraction angle (and therefore focal length) is actually controlled by both Λ and θ_B, as shown in equation 4.2:

$$n_e\delta(1+\cos\theta_o)=\lambda, \tag{6.1}$$

$$\delta=\frac{\Lambda}{\cos\theta_B}. \tag{6.2}$$

Using a fixed θ_B simplifies fabrication, however even with an infinite detuning bandwidth it is not the optimum choice. As shown in chapter 4, θ_B and the diffraction angle θ_o should be related by $\theta_B=\theta_o/2$, otherwise the edges of the grating will suffer reduced diffraction efficiency due to the vector phasematching condition.

For a grating designed to focus light with a wavelength λ at perpendicular distance f from the centre of the grating, the optimum blaze angle is given by:

$$\theta_B(z)=\pi/4-\frac{1}{2}\arctan\left(\frac{z}{f}\right). \tag{6.3}$$

The interference period Λ required to fabricate such a grating can the be calculated using equation 4.28. As can be seen from figure 6.1, using this variable blaze angle requires less interference period detuning to achieve the same focal length; not only will it increase the effectiveness of the grating by meeting the requirements of the vector phasematching condition at the design wavelength, it will also reduce the effects of a limited detuning bandwidth.

Though a variable blaze angle should produce better devices, such devices are more complex to fabricate. Varying the blaze angle requires rotating the interference pattern inside the laser spot during fabrication, which presents major problems with preserving alignment. Instead one can consider rotating the sample around the laser spot. A rotation around any centre of rotation can be represented by a combination of rotations around a fixed centre of rotation and translations; any arbitrary variation in the blaze angle along a device can be fabricated by calculating the correct motion commands to pass to the stage system.

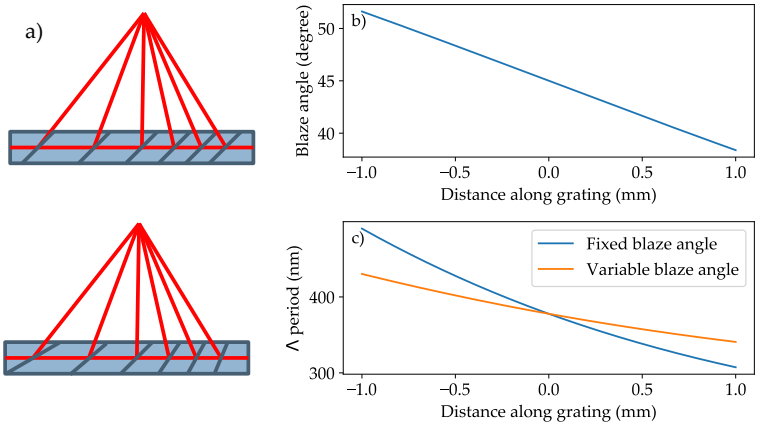

FIGURE 6.1: a) Schematic comparing fixed blaze angle gratings to variable blaze angle gratings. b) Variable blaze angle required for a 2 mm grating at 780 nm with $f = 4.25$ mm following equation 6.3. c) Interference periods required for a 2 mm grating at 780 nm with $f = 4.25$ mm for 45° fixed blaze angle and variable blaze angle (shown in blue and orange respectively).

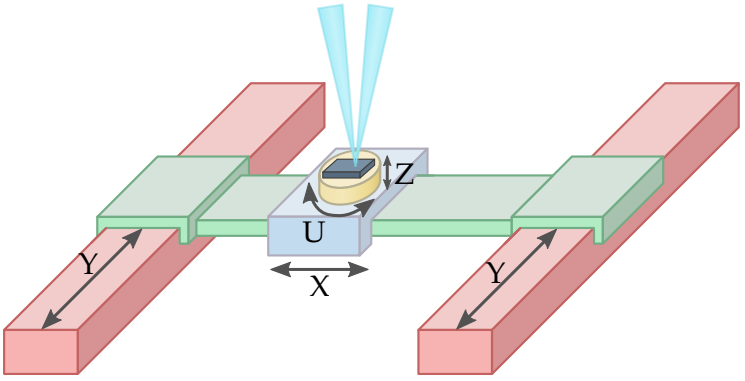

FIGURE 6.2: Geometry of UV writing stage system

6.2 Rotation transformations

The standard UV writing geometry uses straight waveguides with grating planes normal to the waveguide propagation axis. Using the rotation stage it is possible to write grating planes at arbitrary angles to the x axis of the chip (the axes conventions and configuration of the chip and stages are shown in figure 6.2). However this requires a transformation acting on both the waveguide coordinates and the PSO firing positions, which define the grating. Such a rotation in shown in figure 6.3. As was mentioned in the previous section it is very difficult to rotate the writing spot itself, instead the chip is rotated and translated to achieve the same effect. The required transformations can be expressed in matrix form. 3D translations and rotations can be represented by 4×4 matrix transformations, a framework often used in computer graphics. Translation by a vector $\mathbf{v}$ and anticlockwise rotations in the xy plane about the coordinate origin by θ

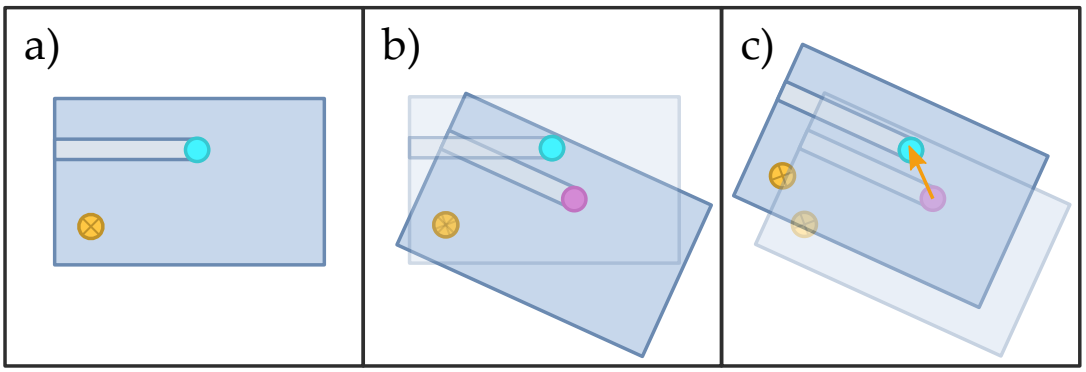

FIGURE 6.3: a) Waveguide writing process without rotation, with the writing spot shown in cyan. b) After rotation about the orange cross the laser spot is no longer at the end of the waveguide from a). c) To correct for an off-centre rotation a rotation transformation (shown by the orange arrow) must be applied.

are represented by $\mathbf{T}(\mathbf{v})$ and $\mathbf{R}(\theta)$ respectively, where

$$\mathbf{T}(\mathbf{v}) = \begin{bmatrix} 1 & 0 & 0 & v_x \\ 0 & 1 & 0 & v_y \\ 0 & 0 & 1 & v_z \\ 0 & 0 & 0 & 1 \end{bmatrix}, \mathbf{R}(\theta) = \begin{bmatrix} \cos\theta & -\sin\theta & 0 & 0 \\ \sin\theta & \cos\theta & 0 & 0 \\ 0 & 0 & 1 & 0 \\ 0 & 0 & 0 & 1 \end{bmatrix}, \tag{6.4}$$

and v_i is the projection of $\mathbf{v}$ along the $\hat{\mathbf{i}}$ axis. A rotation, $\mathbf{R}(\mathbf{c}, \theta)$ about a centre other than the coordinate origin, $\mathbf{c}$, can be performed by translating the desired rotation centre to the origin, rotating, and the performing the inverse of the original translation

$$\mathbf{R}(\mathbf{c}, \theta) = \mathbf{T}(\mathbf{c})\mathbf{R}(\theta)\mathbf{T}(-\mathbf{c}). \tag{6.5}$$

We can generate the required coordinates for the stage to move through by considering the coordinates of the waveguide in the reference frame of the chip. If the waveguide follows a parametric curve $\mathbf{p}(t)$ while rotating through an angle $\theta(t)$ then the coordinate for the stage are given by

$$\mathbf{p}'(t) = \mathbf{R}(\mathbf{c}, \theta)\mathbf{p}(t). \tag{6.6}$$

These rotation transformations were verified using a graphical visualiser designed by Sam Berry. A fixed point was used as a laser spot while a chip was rotated and translated through it, producing a video of the path written by the laser. A still frame from the end of the video output can be seen in figure 6.4 showing the path which would be written under rotation. A file containing a set of pre-transformed coordinates and rotation angles were generated by fabrication code and supplied to the visualiser.

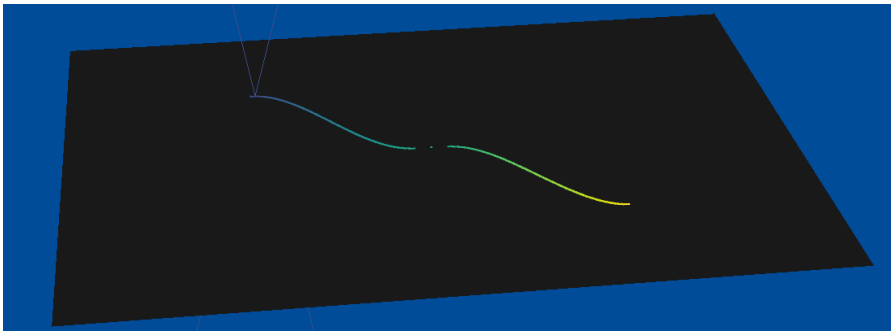

FIGURE 6.4: Image generated by visualiser after a testing a successfully transformed cosine coupler structure. The centre section of the coupler is a straight waveguide, so shows as a single dot in the visualiser, rather than a line.

6.2.1 Centre of rotation and errors

To implement any rotation transformation on writing coordinates the centre of rotation of the stage system relative to the laser spot must be known. The argon ion laser used for ssDUW is realigned every time the system is turned on, as such the centre of rotation relative to the laser spot must also be realigned. A routine for reasonably fast alignment, as well as an understanding of the errors involved in rotation transformations is required.

The centre of rotation can be estimated by tracking features on a rotating sample. This is currently performed manually by the user by rotating the stage in increments, while using joystick control to align a feature on a sample to the laser spot using a microscope focused on the sample. The coordinates after every rotation and alignment are recorded; these form a circle, with the centre of rotation being the centre of this circle. The centre coordinate can be extracted using least squares fitting. It was found that a piece of card marked with a cross by the writing spot made a good target. The standard error of the fitted radius is used as an error estimator to optimise over. This parameter is easy to calculate and is correlated with the true centre of rotation error. Figure 6.5 shows the centre error variation in the centre error estimator as the number of points increases. With a small number of points the error estimator is inaccurate, the fitting routine forces the user to fit at least 8 points to acquire an accurate estimate of the error. After the required minimum 8 points the fitting routine compares the error estimator calculated over all alignment points and compares it to a threshold level (typically set at 1 µm, this threshold is discussed in more detail in section 6.2.2). An error of 1 µm is typically achieved with 30 to 35 points and in less than 5 minutes.

Use of the rotation stage will result in a number of new potential sources of error in the fabrication process: noise due to the limited resolution of the rotation stage, and errors due to an inaccurate centre of rotation. The precision of the rotation encoder is $1 \times 10^{-3\circ}$. Writing 10 mm from the centre of rotation can produce a positional error of 0.17 µm. Though this error is close to the size of the grating period (0.38 µm) it should be relatively random, and is therefore expected to average out across the grating. Error

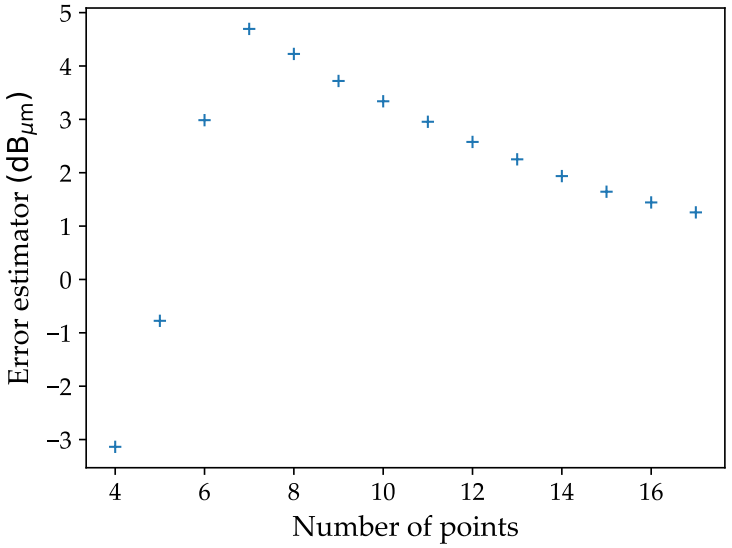

FIGURE 6.5: Variation in error estimator with number of fitted points shown on a log scale. Fits with small numbers of points result in untrustworthy error estimates. Typically 30 to 35 points are required to achieve an error of 1 µm.

in the centre of rotation will result in an error in the rotation transformation, perturbing the shape of waveguides and shifting grating planes. Across a grating with variable blaze angle a small error in the centre of rotation may result in a variable phase error, inducing aberrations in the focus. With no rotation error, the device after fabrication is exactly the device specified before rotation transformation; the act of the fabrication system is to invert the rotation transform with no error. Therefore the effect of centre of rotation error can be modelled by transforming with a finite error, then applying the inverse transformation with no error.

The transformation $\mathbf{R}(\mathbf{c}, \theta)$ required to undergo a rotation θ about a centre of rotation $\mathbf{c}$ is

$$\mathbf{R}(\mathbf{c}, \theta) = \mathbf{T}(\mathbf{c})\mathbf{R}(\theta)\mathbf{T}(-\mathbf{c}). \tag{6.7}$$

If we define an incorrect centre of rotation $\mathbf{c}'$ such that

$$\mathbf{c}' = \mathbf{c} + \epsilon, \tag{6.8}$$

where ϵ is the offset in the centre position, then the resulting transformation $\mathbf{M}$ after fabrication is given by

$$\mathbf{M} = \mathbf{T}(\mathbf{c})\mathbf{R}(-\theta)\mathbf{T}(\epsilon)\mathbf{R}(\theta)\mathbf{T}(\mathbf{c}'). \tag{6.9}$$

By considering properties of translations and rotations this can be simplified to

$$\mathbf{M} = \widetilde{\mathbf{T}}(\epsilon)\mathbf{T}(-\epsilon), \tag{6.10}$$

where $\widetilde{\mathbf{T}}(\epsilon) = \mathbf{R}^{-1}\mathbf{T}(\epsilon)\mathbf{R}$. For a constant angle, $\mathbf{M}$ results in a constant offset acting on

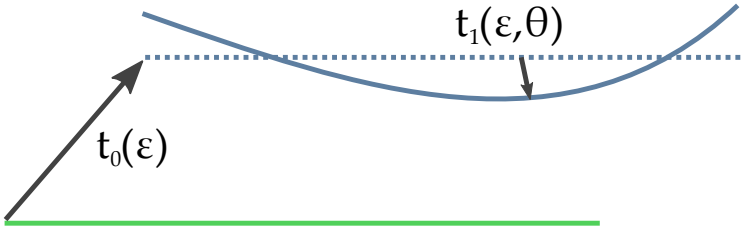

FIGURE 6.6: Graphical description of $\mathbf{t_0}$ and $\mathbf{t_1}$ errors. A waveguide with fixed blaze angle experiences a $\mathbf{t_0}$ error due to the error in the rotation centre which offsets the entire waveguide, shifting the solid green straight waveguide to the dashed blue straight waveguide. Varying the blaze angle along a waveguide results in a $\mathbf{t_0}$ and a $\mathbf{t_1}$ error, changing the solid green straight waveguide to the solid blue curved waveguide.

Design wavelength	780 nm
Refractive index	1.46
Grating length	2 mm
Focal length	4.25 mm

TABLE 6.1: Parameters of variable blaze angle grating for centre of rotation error modelling.

every point along waveguides and gratings. Counter-intuitively, the offset is insensitive to distance of the writing coordinate from the centre of rotation, depending solely on the offset between the actual centre of rotation and the measured centre of rotation. In devices with variable blaze angle the offset varies along the device and will act to modify the period along the device, likely resulting in aberrations.

For a grating with known period the offset due to the centre of rotation can be modelled, and using the scalar diffraction model derived in chapter 4 the effects on the output of a variable blaze angle grating can be investigated.

6.2.2 Effects of centre error on gratings

The offset caused by a grating with the variable blaze angle defined in equation 6.3 was investigated. Grating parameters were chosen to match that of devices intended for fabrication and are summarised in table 6.1. Firstly the effect of centre of rotation error on the coordinates of the grating were investigated. Centre error results in a shift in the waveguide coordinates $\mathbf{t}$. We will separate this shift into a constant offset $\mathbf{t_0}$ dependent on the mean blaze angle and a perturbation to the waveguide shape, $\mathbf{t_1}$, which varies across the grating as shown in figure 6.6. $\mathbf{t_0}(\epsilon)$ is a shift in the position of the grating and waveguide, whereas $\mathbf{t_1}(\epsilon, \theta)$ represents a phase error across the grating and will introduce aberrations into the focus.

The $\mathbf{t_0}$ offsets and $\mathbf{t_1}$ perturbations to the waveguide shape are shown in table 6.2 and figure 6.7 respectively, with all rotation errors displayed in microns. Both offset terms

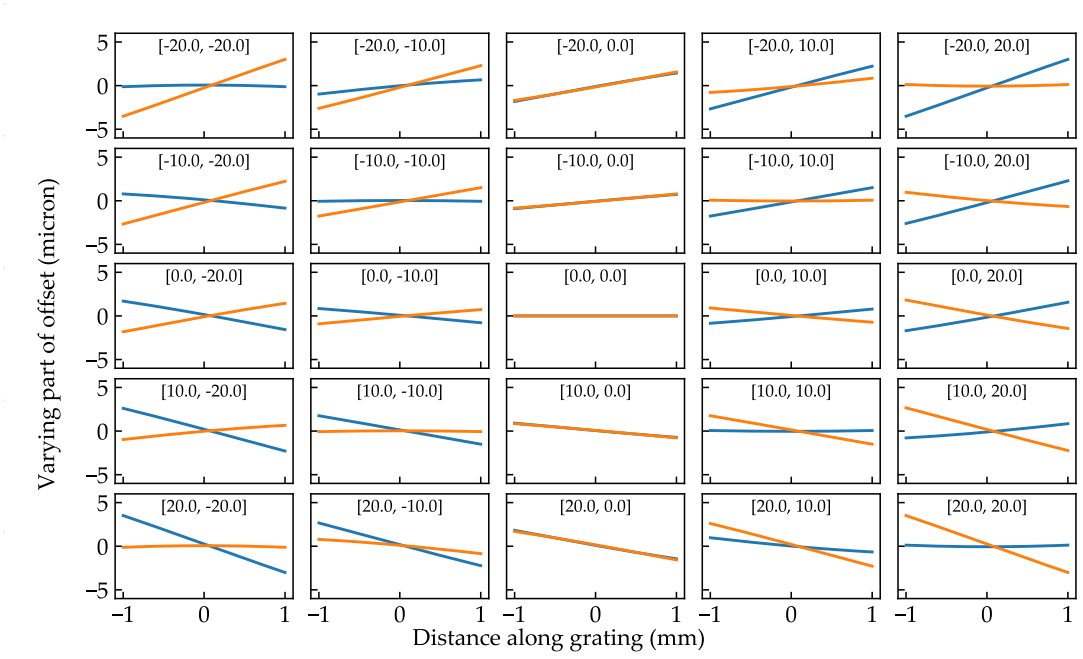

FIGURE 6.7: Angle dependent position offset ($\mathbf{t_1}$) after rotation transformation and fabrication with centre error $[\epsilon_x, \epsilon_y]$ in microns. X and Y components of the offset are shown in blue and orange respectively.

ϵ_y(µm) \ ϵ_x(µm)	−20	−10	0	10	20
−20	[8.2, −19.7]	[1.2, −16.9]	[−5.8, −14.0]	[−12.8, −11.1]	[−19.7, −8.2]
−10	[11.1, −12.8]	[4.1, −9.9]	[−2.9, −7.0]	[−9.9, −4.1]	[−16.8, −1.2]
0	[14.0, −5.8]	[7.0, −2.9]	[0, 0]	[−7.0, 2.9]	[−14.0, 5.8]
10	[16.8, 1.2]	[9.9, 4.1]	[2.9, 7.0]	[−4.1, 9.9]	[−11.1, 12.8]
20	[19.7, 8.2]	[12.8, 11.1]	[5.8, 14.0]	[−1.2, 16.9]	[−8.2, 19.7]

TABLE 6.2: Variation in $\mathbf{t_0}$, the position of the grating (x,y), as a function of centre of rotation error. All distances in µm.

are linearly proportional to ϵ. The $\mathbf{t_0}$ offset is of a similar scale to ϵ itself, with the $\mathbf{t_1}$ offset approximately an order of magnitude smaller. The $\mathbf{t_1}$ errors are all linear with the distance along the grating, which implies a small shift in the focal length and a small phase error across the grating. Analysing the types of aberrations resulting from such offsets is difficult, as the gratings are long enough that the paraxial approximation does not apply; the relationship between distance offset and phase error is nonlinear. For small distance offsets the dominant aberration will be linear coma as it is the lowest polynomial order Seidel aberration.

The scalar diffraction model was used to visually inspect foci with different centre of rotation errors, with results of four potential error scenarios shown in figure 6.8. As shown previously larger rotation centre or rotation errors produce a larger $\mathbf{t_0}$ error, as can be seen in the offset of the foci in figures 6.8d & 6.8e when compared to figure

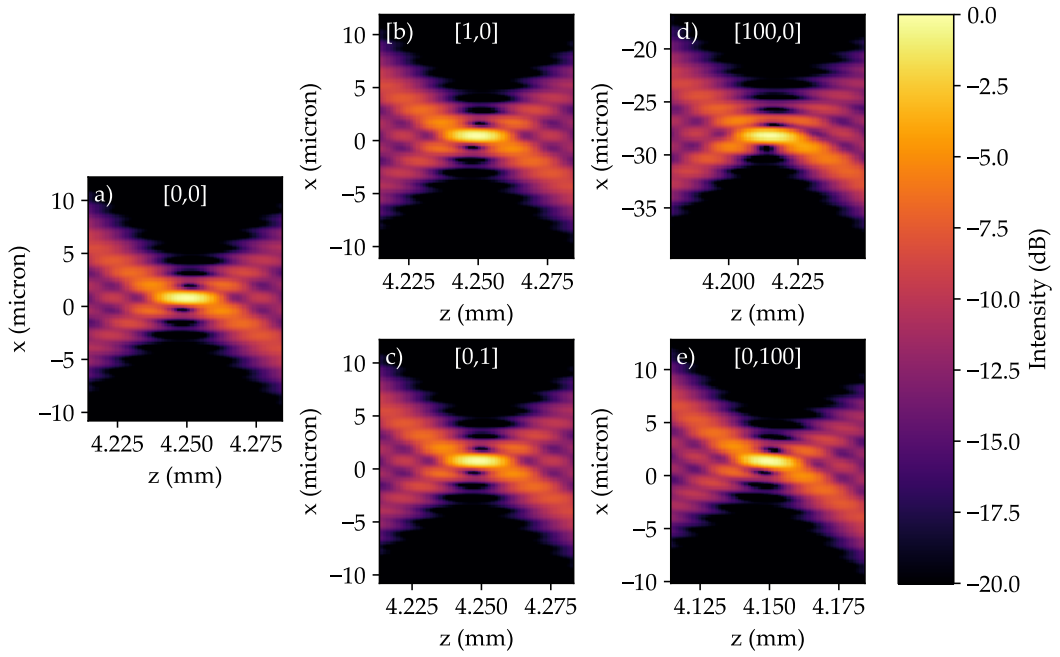

FIGURE 6.8: Scalar diffraction modelling of grating with different centre of rotation errors (centre errors shown in micron in square brackets). Intensity values are shown in log domain and clipped at −20 dB for visibility.

6.8a. The foci for rotation centre errors of 1 µm (shown in figures 6.8b & 6.8c) have no noticeable shift, or any visible aberrations.

The change in the shape of the focal waist is small, even with a relatively large centre of rotation error of 100 µm. Figure 6.8d shows more prominent sidelobes above the focus than below, however figure 6.8e shows no noticeable differences in the focal waist, when compared to the perfect output shown in 6.8a. These results suggest that 1 µm is a suitable threshold for centre of rotation errors, however devices are likely to function with centre of rotation errors far in excess of this threshold.

6.3 C++ design

The ssDUW system at Southampton is built using Aerotech air-bearing stages using a proprietary programming language, AeroBasic. Samples are defined in code following a procedure shown in figure 6.9. The language is rather basic with limited support for typical programming structures like functions, as well as limited mathematical functions. To implement rotation transformations or more complex waveguide paths we had to move to a new language. It was not possible to use typical CNC controllers or software, as our entire platform is based on the PSO system, which is highly non-standard and requires purpose written control software. Aerotech provides a framework for interfacing with the stages using C++, a library was built using this framework to implement writing

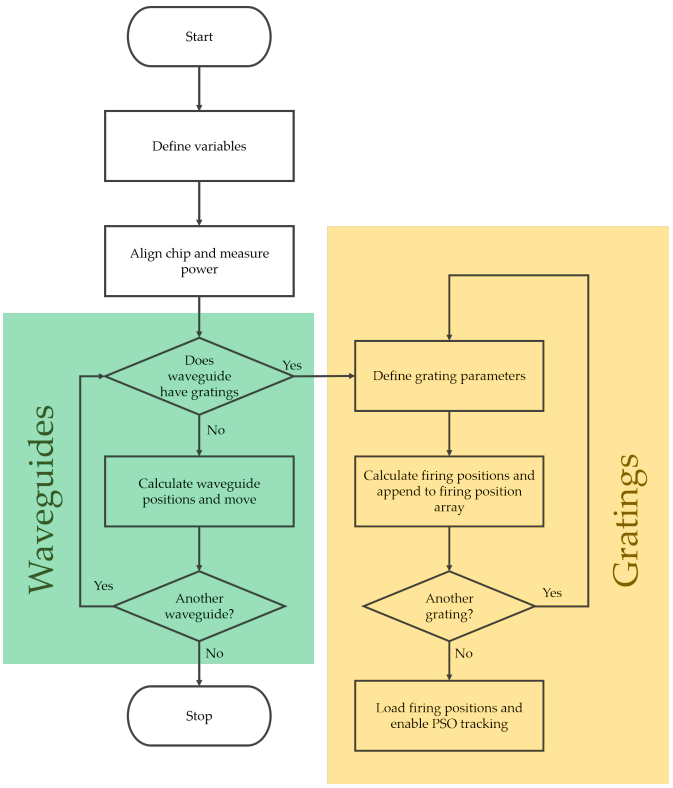

FIGURE 6.9: Flowchart of basic AeroBasic UV writing code with gratings. Waveguide and grating subroutines have been highlighted

in more complex geometries. The structure of the library was designed so new users could build devices from a few extensible building blocks, described in the following sections and add rotation transforms by calling a single function.

6.3.0.1 Waveguides and paths

In AeroBasic waveguides are written sequentially. Each waveguide consists of a set of commands to move the sample under the laser at a specified speed. Most waveguides are straight lines along the x-axis of the chip, however some waveguides have s-bend structures to create couplers. After writing a straight section these waveguides curve up following a prescribed set of curves. When moving to C++ it was decided to implement a number of different path classes to describe straight sections and different curved sections. Each of these classes defines a set of coordinates that describe the path the sample must move through to create such a section. A waveguide class then contains all the code to join together component paths into a smooth waveguide structure, rotating and translating each subsequent path to ensure there are no discontinuities in the coordinates or gradient of the waveguide structure.

Users can add new path classes to create new waveguide shapes by writing code to calculate the coordinates of the new shape. Importantly, no knowledge of the path joining

procedure is required to make devices. This is currently being tested in practice. For example, Delta Hung, a PhD student in our research group, has written code to implement clothoids, curves used to transition between arcs with different radii of curvature. It is expected that such shapes will allow couplers to be compressed while reducing the propagation and bending loss.

6.3.0.2 Gratings

Gratings are described with a set of coordinates known as 'firing positions' (see section 2.3.2), which are calculated from the apodisation, period, phase profile and angle along the grating. These 4 quantities are defined separately; a grating class is used to combine them into coordinates of firing position. Grating classes can be added to waveguides similar to paths, however the firing positions must be deformed to ensure they lie along the waveguide path. Again the user need not understand or interact with this deformation code when defining new elements of gratings.

6.3.0.3 Transformations and writing

Once a set of coordinates for writing waveguides and a set of firing positions can be calculated a waveguide can be written, in a similar manner to G-code. However if the grating or waveguide requires any rotations of the device the movement commands must be transformed using the rotation transformation procedure defined above. In addition the speed must be transformed to ensure the fluence of the transformed waveguide is the same as defined. From the perspective of the user this is performed using a single line command; transformations are handled by code defined in the library using knowledge of the centre of rotation from alignment information.

Though the initial development of this library required a large time investment, it has shown that very complex and varied devices can now be fabricated with simple fabrication code as will be seen in the following sections. A C++ script to fabricate a device with rotation correction, as well as more information about the C++ library can be found in appendix B.

6.4 Fabrication

Devices were fabricated in 20 mm × 10 mm chips of wafer PX194 (which was developed in chapter 3). Samples were hydrogen loaded before writing and written with a fluence of 14 kJ/cm^2. An initial test device was fabricated using a mixture of straight waveguides with unblazed gratings and blazed spectrometer gratings, all written with a fluence of 10 kJ/cm^2. The waveguides were inspected under a microscope, the refractive index

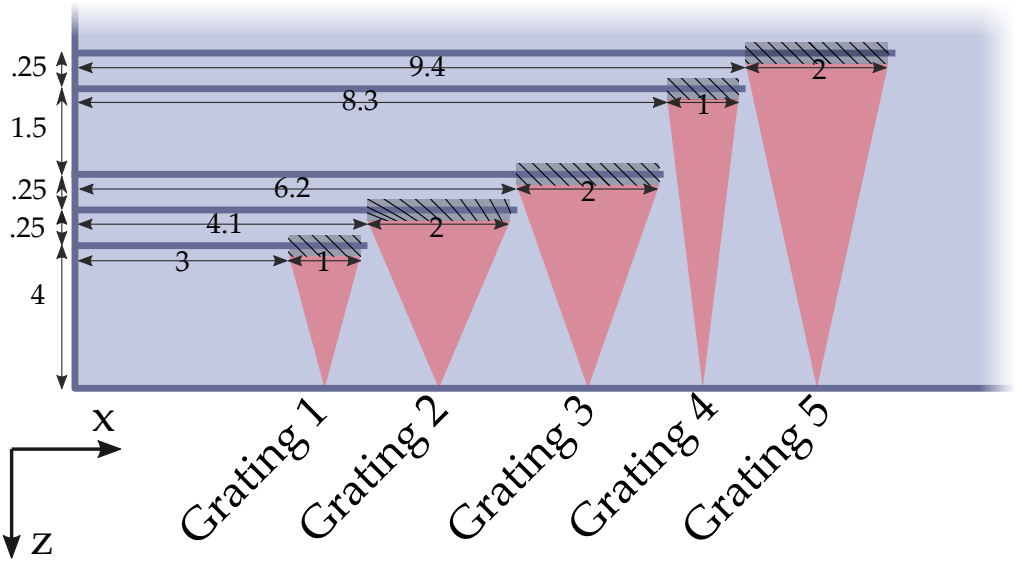

FIGURE 6.10: Layout of waveguides and gratings inside chip. Measurements given in mm.

change of the 45° angled waveguides appeared much weaker. The 45° angled waveguides were significantly harder to couple into than the unblazed waveguides and no output was observed from the spectrometer gratings. It is thought that the angled waveguides were weaker, as the backreflections of the UV light from the silicon substrate during the writing process did not overlap with the waveguide as it would in the core of an unblazed waveguide. This reduces the fluence achieved in the centre region of the waveguide. As such later 45° angles waveguides were written with a fluence of 14 kJ/cm^2.

Prior to writing, the centre of rotation was found using the circle fitting method described in section 6.2.1, with a threshold error of 1 µm. A total of 5 waveguides with blazed Bragg gratings with a combination of variable and fixed blaze angle were fabricated. The layout of gratings is shown in figure 6.10. This initial device was not designed to use the angled detector plane described in section 4.2.3, as a full investigation into attaching detectors onto devices would be required for the 45° detector scheme to be effective. This is addressed as further work later in this chapter.

Initial tests of devices were performed using a broadband 780 nm super-luminescent diode (SLED) source. Output from the gratings could be observed with the naked eye (as shown in figure 6.11). A camera was used to interrogate the output in more detail. A wide horizontal stripe could be seen, this is the expected output from a device with a wide-band source. From previous characterisation it has been observed that outside the focal plane of the device the output on the camera is typically very dim. Observing a bright stripe with a wideband source at the facet is indicative that the device focuses on the facet as intended.

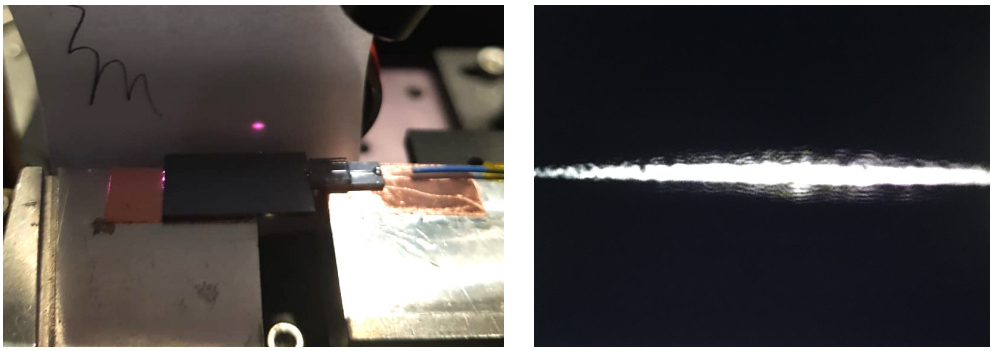

FIGURE 6.11: a) 780 nm light diffracted out of the side of the chip onto a piece of paper, imaged using a smartphone camera sensitive to NIR. b) Camera output with telescope focused on device facet while using SLED source. Output is heavily saturated

Devices were characterised using a tunable external-cavity diode laser (ECDL) laser. The laser was fibre coupled and connected to the device via a 3 dB coupler. The other channel of the coupler was connected to an OSA which was used to record the wavelength of the ECDL. The output of the spectrometer was observed using a Raspberry Pi camera module V2, connected to a relay imaging system using a 3D printed mount. The modehop-free tuning range of the ECDL was much smaller than the tuning range of the Agilent system used in chapter 5 (8 nm, rather than 200 nm), so it was only able to interrogate the resolution close to the design wavelength, however additional information can be inferred from the distribution of the focal spot.

Device facets were not optical quality cuts as the hydrogen loading process and subsequent transport in liquid nitrogen requires too much handling to preserve such facets. In the previous optical characterisation discussed in chapter 5, a cover slip was used as an 'artificial facet' to image through. Due to a change in the mounting geometry, it was no longer possible to align the side of the chip to a cover slip, instead the cover slip was glued to the side of the chip using UV-cured glue, as shown in figure 6.12.

Output from the grating was characterised using a Raspberry Pi NoIR Camera Module V2 and a magnification system as shown in figure 6.12. The magnification system was not calibrated prior to the experiment as the magnification does not factor in resolution measurements. The spatial dispersion of the 4 mm focal length grating was used to approximate the magnification, in comparison with modelling, such that the width of the focal intensity pattern could be established. The image plane (z axis) of the camera was aligned by minimising the width of the primary lobe. This was designed to coincide with the side facet. The camera was then translated horizontally such that the entire modehop free tuning range of the laser could be captured without moving the camera. After tuning the laser wavelength, the laser was attenuated to ensure the image on the camera was not saturated. The wavelength spectrum from the laser was recorded using

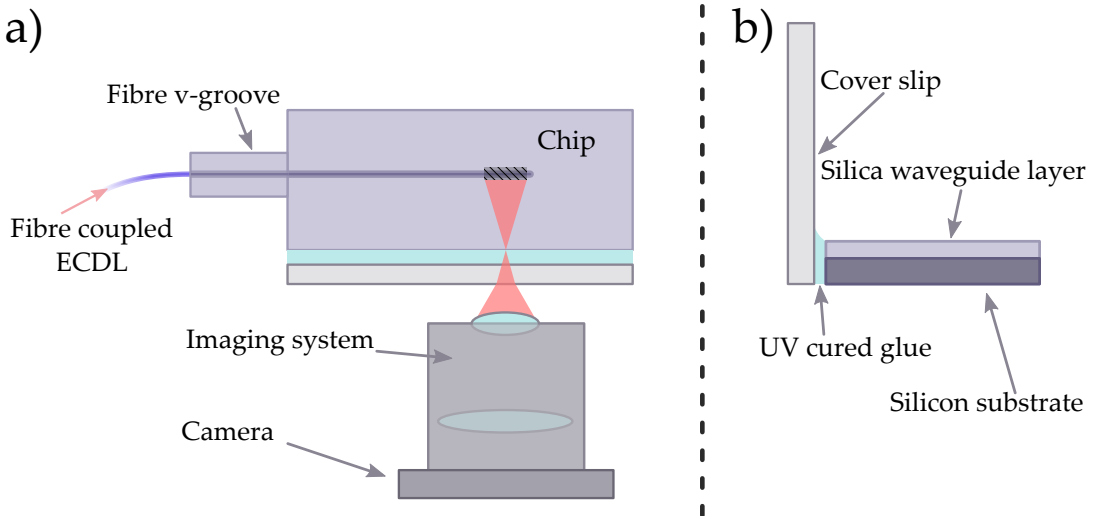

FIGURE 6.12: 780 nm characterisation setup. A fibre coupled ECDL is coupled into a grating via a fibre v-groove. Output from grating is interrogated using a camera and imaging system. A glass cover slip is attached to the side of the chip using UV-cured glue to provide an 'artificial facet'. a) Top-down view. b) End-on view

an OSA and an image was captured from the camera. Analysis of the laser power using the signal from the OSA showed that the device operated with input powers between 74 µW and 4.8 mW. Note that this represents a small range of the input powers the device was sensitive to (close to saturation). This is a promising initial result and is expected become more sensitive with optimisation of refractive index modulation. Modelling of 45° blazed Bragg grating polarisers by Posner et al. [2] can be used to approximate the light coupled out of devices after such optimisations. Using waveguide mode parameters the expected coupling out of the Bragg grating toward the detector is approximately 0.0014 dB/mm, however by optimising the refractive index contrast to 3×10^{-3} (previously seen in UV written hydrogen loaded FHD samples [3]) the coupling increases to 0.31 dB/mm. With a 2 mm long uniform apodised grating such a device could couple 10 % of the power out of an input waveguide, which when combined with the high dynamic range of CCD will allow spectral measurements of free space spectral sources, even with poor mode matching to SM fibre.

6.5 Results and Analysis

The majority of the following analyses consider grating 1 and grating 3. Grating 1 was a 1 mm long device with a fixed blaze angle of 45° and a focal length of 4 mm. Grating 3 was a 2 mm long device with a variable blaze angle following equation 6.3 and a focal length of 4.25 mm (see figure 6.10 for more information). Both devices were positioned such that their focal planes coincided with the side facet of the chip. Initial measurements from the device showed that the addition of the artificial facet was not wholly successful. Aside from gratings 1 and 3, all other devices showed distortions in

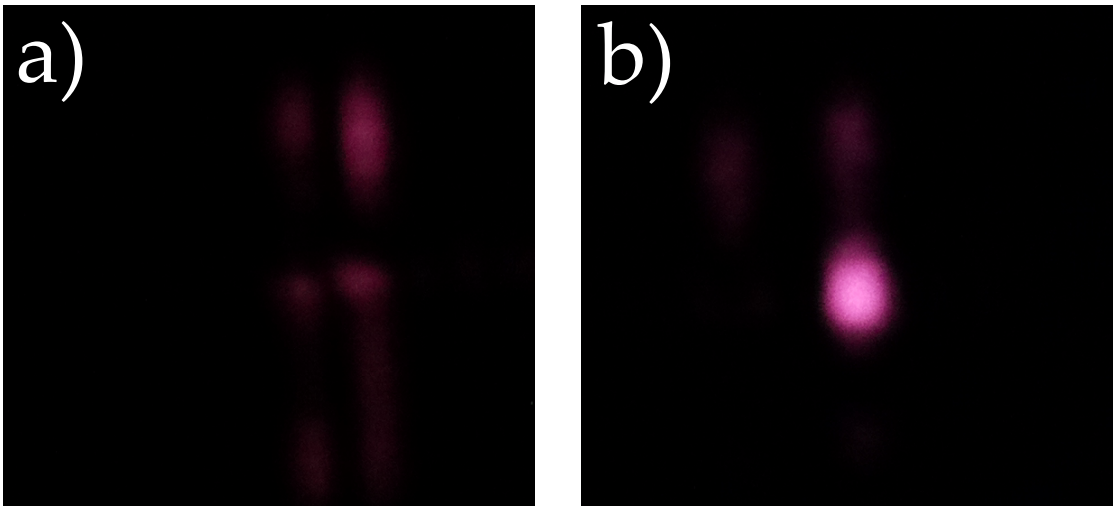

.

FIGURE 6.13: a) Focal spot of grating 4, with distortions caused by artificial facet. b) Focal spot of grating 1 for comparison)

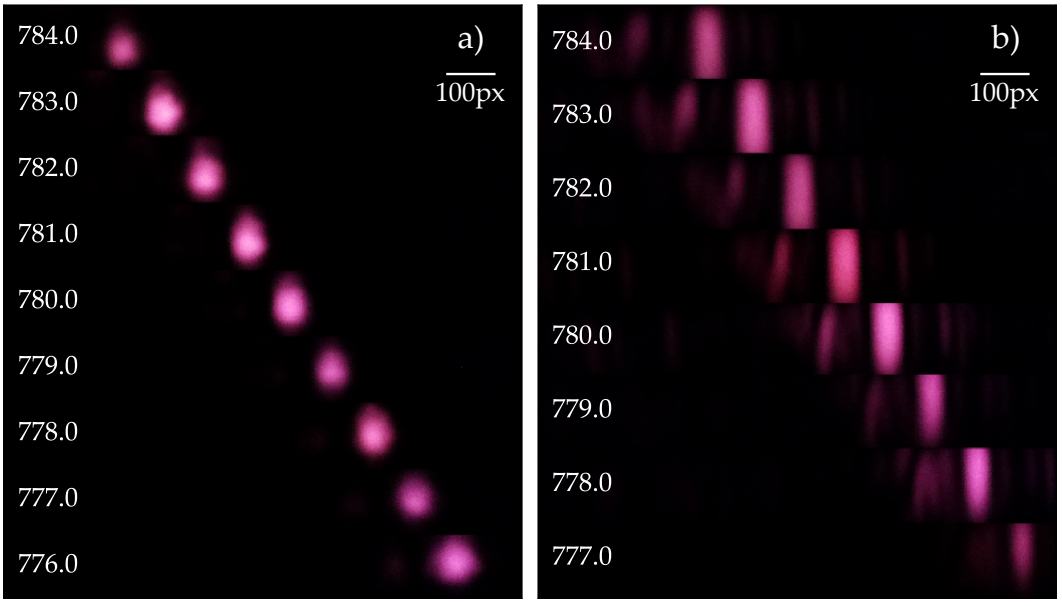

FIGURE 6.14: Composite of images of the spectrometer output with laser wavelengths between 776 nm and 784 nm for a) grating 1 and b) grating 3. Output of grating 1 was a well focused Gaussian spot, grating 3 focused slightly outside the edge of the chip, the intensity pattern is taller due to diffraction of planar mode. Grating 3 also exhibited sidebands.

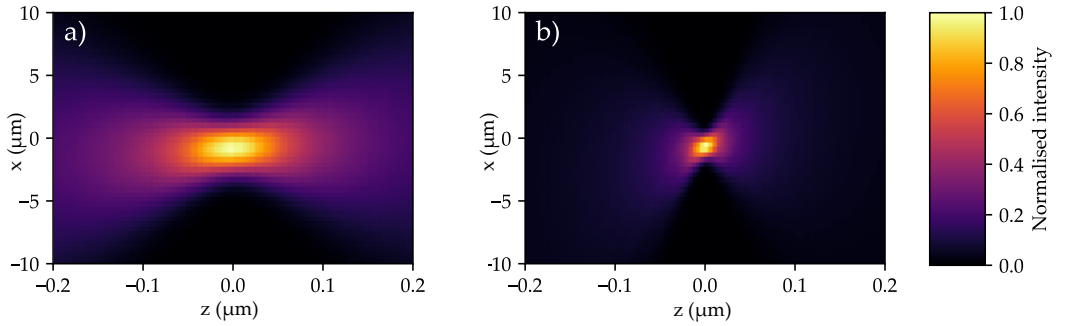

FIGURE 6.15: Scalar diffraction modelling for a) grating 1, b) grating 3, including grating detuning effects. Both foci are at the desired position, with grating 3 possessing a smaller focal waist, as expected from the increased grating length.

their output involving additional vertical lobes, these can be seen in figure 6.13. It is thought these lobes are caused by the meniscus of the glue at the interface between the chip facet and the cover slip. The lobes were not seen in the initial observations shown in figure 6.11b prior to the addition of the coverslip. Gratings 1 and 3 were relatively unaffected, it is likely that there was enough glue around these gratings to uniformly fill the gap between the facet and the cover slip.

Grating 1 showed a very clean focal spot at the facet of the chip and linear wavelength dispersion, as can be seen in figure 6.14a. The output of grating 3 can be seen in figure 6.14b. The intensity pattern contained sidelobes and the width of the central peak was at its narrowest a small distance away from the facet (later calculated as 5.1 µm using the waist size of the diffracted vertical cross section). In addition, the size of the diffracted waist was much larger than had been expected. Despite the grating being twice as long, the waist of the focus from grating 3 was approximately the same size as the waist from grating 1. The firing positions and angles used the fabrication process were logged by fabrication code, these were used with the scalar diffraction model to analyse the expected width and position of the focus, with results shown in figure 6.15. Both gratings focus at the correct position, notably neither of them show visible aberrations or sidebands. In addition the focal waist of grating 3 is considerably narrower than the waist of grating 1. Earlier analysis on the centre of rotation error has shown that aberrations arising from centre of rotation error would be negligible for grating 3 with the tolerance on the centre of rotation achieved during fabrication (i.e. 1 µm).

The distance of the focal plane of grating 3 from the chip facet was analysed using Gaussian beam diffraction. The vertical cross section of the output of grating 1 represents the guided mode of the planar waveguide. It was calculated that such a mode would have to travel 5.1 µm through the cover slip before it would achieve the vertical cross section seen in the output of grating 3. A small focal shift, as well as horizontal sidebands could be introduced by small amounts of positive spherical aberration. Such small spherical aberrations could be introduced by the cover slip itself and the imaging system.

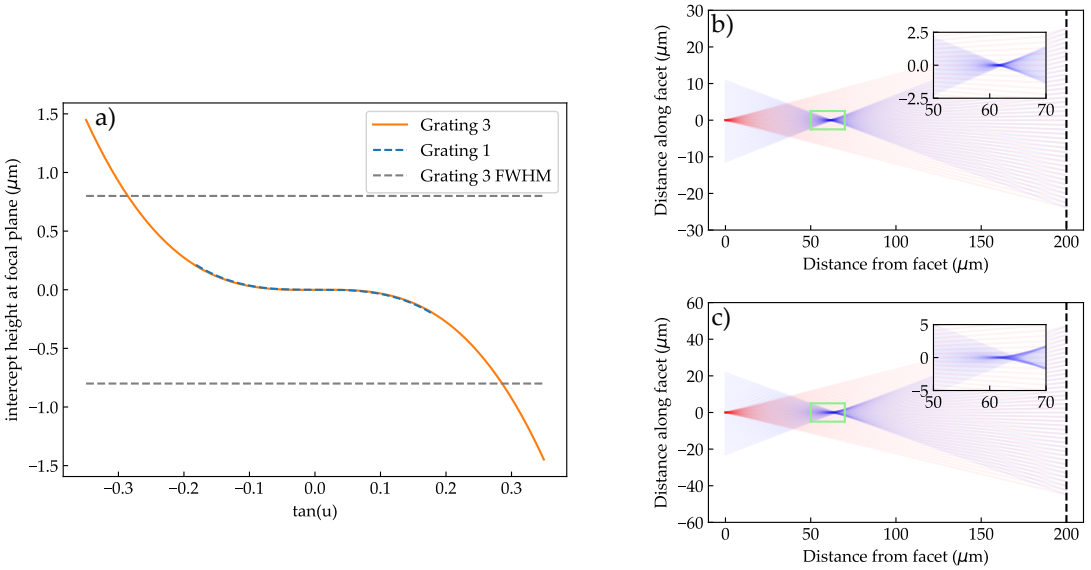

FIGURE 6.16: a) ray intercept diagram of aberrations resulting in imaging though a 200 µm thick glass slide. The deviations in ray height exceed the FWHM for grating 3. The FWHM of grating 3 is ≈ 7× larger than the deviations for grating 1. b) and c) Ray tracing of the reconstructed foci for gratings 1 and 3 respectively. Red rays are traced from a perfect focus at the facet to the interface of the glass slide shown by the grey dashed line on the right. Reconstructions of foci after diffraction are shown in blue. Insets show enlarged image of the reconstructed focus highlighted by the green box.

In the paraxial ray approximation a thin layer with a different refractive index does not produce aberrations. For long gratings with short focal lengths this approximation is not valid and adding such a layer will indeed induce aberrations. The simplest way to analyse such aberrations without considering second order effects introduced by the imaging system is to calculate the angles at which that refracted rays would leave the cover slip, and trace them back toward a reconstructed focus. Such constructions are shown in figures 6.16b & 6.16c for grating 1 and grating 3 respectively. Both foci exhibit spherical aberration, with greater aberrations seen in the focus of grating 3 (shown in the inset of 6.16c). These aberrations can be quantitatively analysed using ray intercept diagrams (previously discussed in section 4.2.2), with results shown in figure 6.16a.

At the focal plane the deviations in ray height for grating 3 are greater than the FWHM of the focal spot. For grating 1, the deviations are ≈ 7× smaller. The ray intercept diagram can also be used to predict the focal plane shift due to spherical aberration, it was found that the focal plane of grating 3 shifts by approximately 4.1 µm due to spherical aberrations. This provides an estimate of the focal plane shift that is in good agreement with the measured value of 5.1 µm.

Similar to previous analysis in chapter 5, the images at different wavelengths were reduced to a 1D array of intensity values by summing pixel values, these 1D cross sections were then used to calculate the wavelength dispersion, spot width and Houston resolution. The dispersion, width and resolution are shown in figure 6.17, with modelled

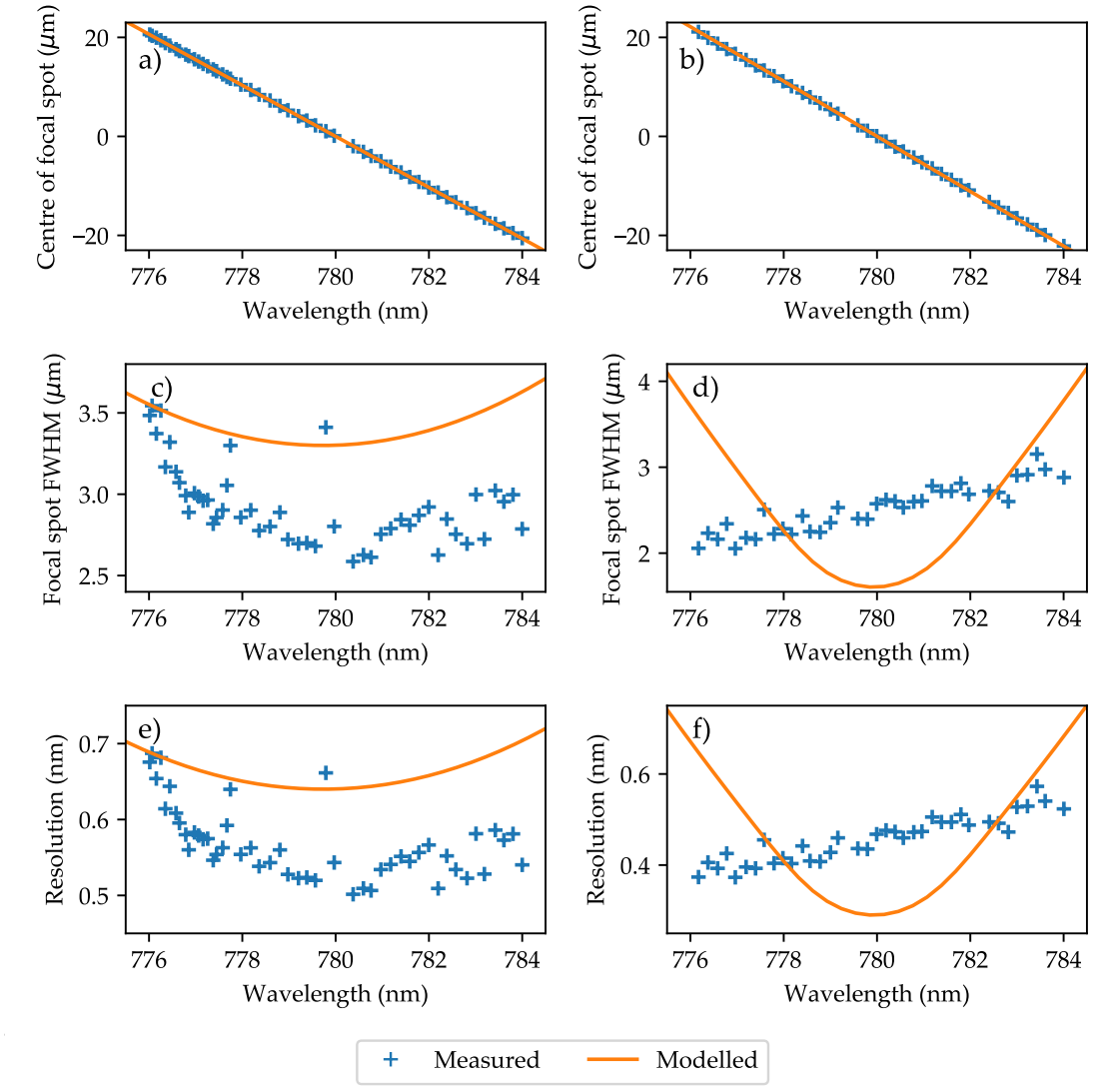

FIGURE 6.17: a) Wavelength dispersion for grating 1. b) Wavelength dispersion for grating 3. c) Spot width for grating 1. d) Spot width for grating 3. e) Resolution for grating 1. f) resolution for grating 3.

results for a detuning bandwidth of 37.7 nm and the detector plane situated along the device facet. The dispersion measurements and modelling in figure 6.17a were used to calculate the magnification of the imaging system and rescale all other measured values from pixel values into real distances. The rescaled dispersion was 5.1600 ± 0.0004 µm/nm for grating 1 and 5.5000 ± 0.0006 µm/nm for grating 3, with the longer focal length of grating 3 leading to an increase in the dispersion. The focal plane offset in the measurements for grating 3 has minimal effect on the measured dispersion as it is very small compared to the focal length (4.25 mm). Modelled dispersion is in close agreement with measured dispersion for grating 3 despite aberrations, similar to results seen in chapter 5.

The measured spot widths for grating 1 shown in figure 6.17c are smaller than expected.

This is thought the be due to an underestimate of the grating detuning bandwidth. The same method was used to calculate the detuning bandwidth of the writing board as was used in chapter 5. As a result the near field of the fabricated device is wider than that predicted by modelling, and the measured focal distribution is narrower. Width data for wavelengths further from the design wavelength would be useful to estimate the actual detuning bandwidth. The distribution of the measured widths is curved, as expected from a non-angled detector plane due to wavelength dependent focal plane shift interacting with the near Gaussian beam waist. The curvature of the modelled data is shallower than that of the measured data, which again supports a wider detuning bandwidth. Aberrations have a large effect on the spot width of the output from grating 3. Curvature in the measured spot width is not observed, as the narrow beam waist is obscured by aberrations, however the minimum spot width is slightly narrower than that observed from grating.

Due to the highly linear dispersion the resolutions for both grating 1 and 3 are proportional to their spot widths. The achieved resolutions for both grating 1 and grating 3 were improvements on previous devices, with peak resolutions of 0.5 nm and 0.4 nm respectively. Such devices meet the resolution requirements for Raman spectroscopy specified in section 1.3. The bandwidth of the devices is more difficult to analyse. The modehop-free tuning range of the source was very limited (776 nm to 784 nm), as such a full investigation of the bandwidth could not be performed. Earlier modelling results showing the potential bandwidth of devices using an angled focal plane (see section 4.2.5) suggests that devices should be able to meet bandwidth requirements, however further experiments are required to confirm this.

6.6 Conclusions and further work

A scheme was presented to increase the length of blazed chirped Bragg gratings past the previous fabrication limit set by the grating detuning bandwidth by varying the blaze angle along the grating. Devices were fabricated using a custom built C++ library which enables other users to use the rotated geometry with simple device code. A full investigation into the coordinate transformations required to implement variable blaze angle, along with alignment tolerances from the centre of rotation and possible fabrication errors introduced by the new geometry was undertaken. The error in the coordinates of fabricated devices associated with centre of rotation is largely a constant offset, errors below 1 µm lead to negligible changes in devices.

Devices were characterised using a tunable ECDL laser and an imaging system. A glass cover slip was glued to the side of the device to provide a smooth surface to image; nonuniformity in the glue distorted the output of a number of devices rendering them unusable. A device with variable blaze angle and long grating length was compared to

a device with fixed blaze angle and shorter grating length. The device with fixed blaze angle performed as expected, achieving a peak resolution of 0.5 nm and worst resolution of 0.7 nm over a 776 nm to 784 nm. The longer device experienced spherical aberrations due to imaging through the glass cover slip. As such the device achieved a resolution of 0.4 nm to 0.5 nm, rather than the 0.3 nm resolution expected from modelling.

Resolutions of integrated spectrometers operating at 600 nm to 800 nm wavelengths discussed in chapter 1 vary between 0.015 nm to 1 nm, with most around 0.2 nm. The devices presented in this chapter, even without imaging aberrations, have worse resolution, but are close to those presented. Note that the resolution shown here is not a hard limit, but an initial result. Without increasing the footprint of the device, a 17 mm focal length is possible while implementing the 45° detector mounting scheme, which should enable resolutions in excess of 0.15 nm by increasing the grating length. Contrary to those higher resolution devices, the device presented here has a clear route to achieve operation over a wide bandwidth using the 45° degree detector mounting scheme. The results shown in this chapter are an important step towards that goal, integration is very costly at 1550 nm. Not only has this chapter shown spectrometers at a new wavelength, using a new wafer design, and a new purpose-built ssDUW interferometer writing board, but it has shown the first demonstration of variable blaze angle gratings using a custom built C++ software library.

Future work will build on the result shown in this chapter focusing on integration and packaging. Integrating detectors with devices requires an investigation into methods of creating an optical quality facet after the UV writing process and methods of robustly attaching a detector array or CCD to that facet without perturbing the optical output. Once such a device has been made, spectrometer prototypes will be ready for investigations into calibration and portable field testing.

6.7 References

[1] J. W. Field, S. A. Berry, R. H. S. Bannerman, C. B. E. Gawith, P. G. R. Smith, and J. C. Gates, "Optimizing resolution in an integrated blazed chirped Bragg grating spectrometer," in *Integrated Optics: Devices, Materials, and Technologies XXIV*, vol. 11283, 2020, pp. 145–150.

[2] M. T. Posner, N. Podoliak, D. H. Smith, P. L. Mennea, P. Horak, C. B. E. Gawith, P. G. R. Smith, and J. C. Gates, "Integrated polarizer based on 45° tilted gratings," *Optics Express*, vol. 27, no. 8, pp. 11 174–11 181, 2019.

[3] M. T. Posner, "Optical integrated circuits for large scale quantum networks," Ph.D. dissertation, 2017.

Chapter 7

Conclusions

This thesis has provided an initial investigation into blazed chirped Bragg grating spectrometers. The devices developed in this thesis have a much larger theoretical bandwidth than those discussed in chapter 1, beyond that of the fibre speckle spectrometer presented by Redding et al. [1] (which was impractical for portable operation due to temperature instability). The devices have spectral resolution suitable for interrogation of Raman shifts in the spectral fingerprint region. Though the bandwidth has not been experimentally verified I believe that when models are adjusted, to take waveguide modes into account, the bandwidth will be suitable for OCT. Similarly experimental results and modelling suggest that blazed chirped Bragg gratings will have suitable resolution and bandwidth for Raman spectroscopy.

At the start of this theses, a number of questions were posed about the potential spectrometer platform and how it operates (see section 1.4).

- Do 45° low-index contrast blazed Bragg gratings diffract enough light to make useful spectrometers?
- Can we model the output of the device for a given wavelength to predict performance?
- What factors control the spectral resolution of the device?
- What factors control the response bandwidth of the device?
- Are the proposed devices fabricable?

These questions are addressed in the following sections.In addition I will try and give perspective on how a potential device using this spectrometer scheme (shown in figure 7.1) would perform in comparison with other current commercially available devices.

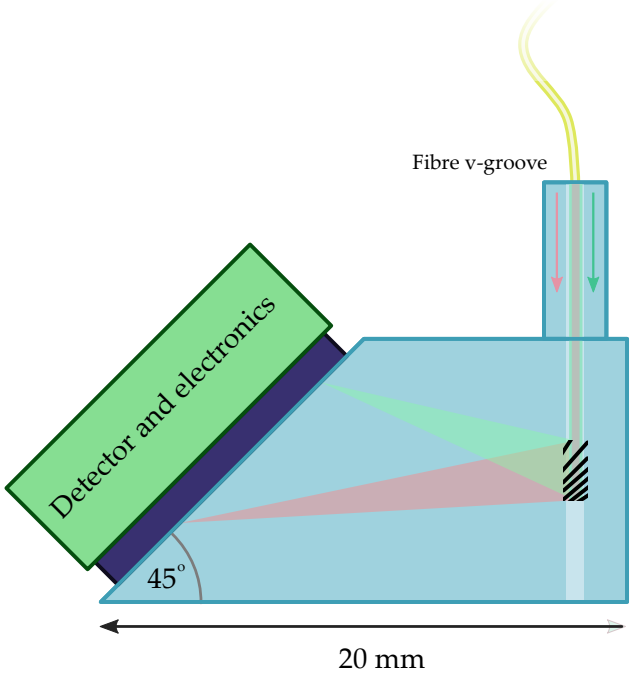

FIGURE 7.1: Proposed prototype device with an attached detector, a 2 mm long variable blaze angle grating and a focal length of approximately 16 mm.

7.0.1 Grating diffraction strength

In chapter 6 it was shown that a spectrometer operating at 780 nm using a Raspberry Pi camera module V2 was able to measure signals from a laser varying between 4.8 mW and 74 µW. Note that these do not represent the absolute detection limits of the system, these were just the maximum and minimum laser powers used during resolution measurement. The 4.8 mW signal was just below saturation on the camera, it is likely given typical dynamic ranges for similar sized image sensors that the spectrometer will be capable of measuring signals well below the 1 µW level. With optimisation of refractive index contrast this detection limit will increase even further (potentially sub 1 nW). Detection of weak signals is particularly useful feature for integrated spectrometers. Not only is it essential for Raman spectroscopy, but it is incredibly helpful when working with free space light sources. Coupling a few nanowatts of light from a free space source (a low-pressure atomic gas lamp for example) can be easily achieved using a fibre collimator package, without the requirements that the light source be well mode matched to the fibre. This allows the blazed Bragg spectrometer to be used in more potential applications where its small footprint and potential low cost is attractive.

7.0.2 Device modelling

A number of models have been developed to predict the behaviour of devices and are discussed in chapter 4. A ray model which traced the trajectory of rays from sub-sections

of the grating has been shown. This did not model the diffracted field or intensity pattern diffracted from the device, however it could model spectral dispersion as well as analyse the presence of aberrations. This model is very fast and is valid outside the paraxial approximation. A beam propagation model was used to show the intensity pattern of devices as they focus. This model was used to calculate the resolution by varying the input wavelength and monitoring the position and width of the intensity profile at the focal plane. This model is fast, however it suffers from phase errors outside the paraxial approximation and as such it is poorly suited to analysing devices where the ratio of grating length to focal length exceeds 0.2. Finally a model was proposed and implemented using scalar diffraction theory which accounts for blaze angle and the finite extent of grating planes. This model was used to analyse the effects of mounting the detector in different geometries, as well as changing the blaze angle and waveguide width to investigate device bandwidth.

7.0.3 Resolution

The device resolution was first investigated using the Gaussian optics approach proposed by Madsen et al [2]. Outside the diffraction limit, spectral resolution was inversely proportional to grating length (as shown in equation 4.29) and spectrometers which focused at a small angle had larger resolutions (up to a factor of 2 improvement). Intensity modelling later confirmed that resolution was inversely proportional to grating length. It also showed that the distance from the grating to the focus changed with wavelength. As such, devices did not focus at a plane parallel to the waveguide as expected, but along a plane at 45° to the grating. Far from the design wavelength focal plane curvature was visible, with the degree of curvature determined by the ratio of grating length to focal length. It was shown that Gaussian apodised gratings are more tolerant to focal plane curvature, though have lower peak resolution than uniform gratings of a similar length.

Resolution was measured in fabricated devices. Chapter 5 showed improvements in the resolution due to correction of linear coma in a device, with a peak resolution of 1.8 nm at 1560 nm, a typical resolution of 2.6 nm over a 100 nm bandwidth and operation across the whole wavelength of the tunable laser (1440 nm to 1640 nm). Grating detuning bandwidth limited the peak resolution, the high rate of chirp used to fabricate the device resulted in the edges of the devices having lower grating refractive index modulation than the centre, effectively reducing the length of the grating. The characterisation system used to measure the device did not use the 45° detector mounting scheme as it was difficult to achieve without physically attaching an InGaAs detector to the device, which was deemed prohibitively expensive.

Chapter 6 suggested a more complex scheme with varying blaze angle along the grating to increase the grating length and reduce the effects of grating detuning based apodisation. To our knowledge this is the first demonstration of a blazed Bragg grating with

Application	Resolution (nm)	Bandwidth (nm)	Central wavelength (nm)
Raman spectroscopy (780 nm pump)	0.35	80	870
OCT (800 nm pump)	2	150	800
Hyperspectral imaging (visible)	1 - 10	250	575
Hyperspectral imaging (visible and NIR)	1 - 10	550	725

TABLE 7.1: Summary of the required device characteristics for applications set out in section 1.3.

variable blaze angle. Devices were moved to 780 nm to attempt to utilise low-cost silicon detectors, as such a new set of waveguiding layers was optimised, with the results shown in chapter 3. A C++ library was created to process transformations from normal writing coordinates to rotated writing coordinates. Devices were characterised using a tunable ECDL laser and a low-cost Raspberry Pi Camera Module V2. A device with a 1 mm 45° blazed grating achieved a resolution of 0.5 nm to 0.7 nm over a 776 nm to 784 nm wavelength range. A device with a 2 mm grating, with blaze angle varying between 37° and 50° was expected to achieve 0.3 nm resolution from modelling, however achieved 0.4 nm to 0.5 nm over a 776 nm to 784 nm wavelength range, a marginal improvement over the 1 mm grating. Further analysis showed the variable blaze angle grating was outside the paraxial approximation, and therefore suffered from spherical aberrations due to the characterisation system. The aberrations were in the range expected given the nature of the device and the characterisation system, as such there is strong evidence that the variable blaze angle grating was successful.

The modelled resolution of the blazed Bragg grating spectrometer proposed in figure 7.1 with a grating length of 2 mm is $\approx$ 0.3 nm for 780 nm wavelength light. This is suitable for both Raman spectroscopy and OCT, however is worse than the resolutions offered by commercial devices. Spectrometers made by Ocean Insight and Wasatch Photonics achieve resolutions of 0.06 nm and 0.25 nm respectively, as shown in table 7.2. This is characteristic of the dispersive spectrometers; the spectral resolution depends on the maximum phase delay achievable across the dispersive element. Miniaturised bulk spectrometers with larger gratings can achieve higher resolutions than miniature devices. The blazed Bragg grating scheme meets the resolution requirements for all the applications discussed in section 1.3 (summarised in table 7.1), however the current scheme is extremely unlikely to exceed the resolution of commercial devices due to its small footprint.

Device	Resolution (nm)	Wavelength range (nm)
Ocean Insight HR4000 (5 µm slit and 1800 grating)[3]	0.06	747 to 837
Wasatch Photonics WP 785 (10 µm slit)[4]	0.25	796 to 924
Blazed chirped Bragg grating	0.3	730 to 830

TABLE 7.2: Comparison of proposed spectrometer scheme to existing commercial miniaturised bulk devices.

7.0.4 Bandwidth

Device bandwidth was modelled using the scalar diffraction model and was found to be determined by the width of grating planes, typically dictated by the width of waveguides. For a 7 µm rectangular waveguide operating at 1550 nm the 3 dB bandwidth was 210 nm when using the 45° detector mounting scheme. This value should be viewed as a conservative lower bound, as the model currently assumes plane waves propagating inside waveguides rather than waveguide modes. Preliminary experimental measurements of the bandwidth using a device at 1550 nm showed that a device operated over 200 nm, with measurements limited by the bandwidth of the tunable laser source.

The spectrometer shown in figure 7.1 is expected to achieve a bandwidth of at least 100 nm given the results of modelling in chapter 4. This would be comparable to commercial devices shown in table 7.2. Commercial bulk devices have a larger footprint, and can use a longer focal length to achieve higher spectral dispersion, which makes resolving small wavelength changes easier and reduces the effects of focal plane curvature. Conversely this reduces bandwidth, as the same distance across the detector corresponds to a smaller wavelength change with high spatial dispersion.

The blazed Bragg grating scheme device shown in figure 7.1 is expected to meet the requirements of Raman spectroscopy (allowing for a small modification in the waveguide/substrate to account for a different central wavelength) shown in table 7.1. It is also possible given the conservative nature of bandwidth estimates that such a device also meets the bandwidth requirements for a useful OCT system. Though it has lower spatial dispersion and therefore potentially higher resolution than the commercial devices, the bandwidth suffers from other limitations (focal plane curvature, higher order waveguide modes). As such, it is unlikely that the bandwidth of a blazed Bragg gratings spectrometer will greatly exceed that of commercial miniaturised bulk devices.

7.0.5 Fabricability

This thesis has shown fabrication of a range of devices and has demonstrated that blazed chirped Bragg gratings are sufficient to control aberrations in the output of devices. The devices have satisfied the requirements for footprint specified in section 1.3, even

when considering the planned next generation of devices with longer grating length and focal length. Devices have yet to be shown with an optimised refractive index contrast (required for increasing output efficiency), however this has not yet been investigated. Previous work within our research group has shown higher refractive indices of 3×10^{-3} within UV written FHD germanosilicate Bragg gratings. Further work on optimisation of writing fluence is required to ascertain whether this is achievable in this sample or whether a further iteration of wafer recipes is required.

Currently, devices are fabricated using the ssDUW method. This fabricates a single device at a time and requires an expert laser user to align and operate the system. Although the material cost per device is relatively low, devices are expensive to fabricate via this method. Given the comparable performance of the device to commercial competitors and minimal reduction in size (when control electronics and packaging are considered) the scheme is unlikely to be of current commercial interest. A potential solution to this would be to investigate an alternative fabrication route.

The ssDUW platform is attractive as a rapid-prototyping technique, however once a design is finalised, it is possible to define waveguides using photolithography and gratings using a phase mask. This would potentially allow multiple devices to be fabricated at the same time using standard cleanroom processing techniques, reducing the cost.

7.1 Future work

7.1.1 Detector mounting and packaging

Current work has been aimed at producing a device with a CCD detector attached to the chip facet. Detectors at 1550 nm were prohibitively expensive, however the development of a 780 nm wafer and subsequent spectrometer results show that 780 nm is a promising wavelength range for integration. In addition to increased stability and a smaller footprint, integrating detectors with devices would allow a full investigation of the 45° detector mounting scheme, as well as removing imaging aberrations from non-paraxial devices.

A new generation of devices with facets at 45° to waveguides would need to be fabricated. Facets would need to be polished after the ssDUW process and detectors glued onto the facet. As has been observed in chapter 6 introducing a glue layer can cause significant problems in device output, so a reliable technique to glue detectors to devices without damaging devices or detectors would need to be identified. The Raspberry Pi camera module used in chapter 6 is a good candidate for initial detectors, the small pixel pitch of the detector (1.12 µm) means small wavelength differences can be observed even with minimal spatial dispersion. In addition a Raspberry Pi computer could be used to

process image data, providing a fibre input prototype spectrometer in a smartphone sized package.

7.1.2 Calibration

Currently no real spectral data has been measured using the spectrometers in this thesis. The imaging system used to record intensity data was mechanically unstable, as such it was difficult to collect and process a calibration data set before such data were rendered invalid. Moving to an attached detector will significantly increase the long term stability of the device, such that calibration can be explored. It is also proposed that the system used to characterise spectrometers move from a tunable laser source to a set of fibre Bragg gratings and an SLED source. Work at Southampton has recently shown a method of creating many high-quality Bragg gratings overlaid in the same stretch of optical fibre[5], such a device could be used to provide a set of reference peaks to calibrate the spectrometer. Strain and temperature can both be used to tune the peaks of Bragg grating signals, as such a small number of images with many spectral peaks could be used to characterise the whole spectral bandwidth of the device quickly and in an automated manner.

With calibration information a wavelength spectra could be reconstructed from pixel intensity values in an image. This should enable investigations into use in Raman spectroscopy and OCT. Practical demonstrations of a portable integrated platform for these technologies are likely to generate high impact publications.

7.2 References

[1] B. Redding, M. Alam, M. Seifert, and H. Cao, "High-resolution and broadband all-fiber spectrometers," *Optica*, vol. 1, no. 3, pp. 175–180, 2014.

[2] C. K. Madsen, J. Wagener, T. A. Strasser, M. A. Muehlner, E. J. Laskowski, and J. DeMarco, "Planar waveguide optical spectrum analyzer using a UV-induced grating," *IEEE Journal of Quantum Electrononics*, vol. 4, no. 6, pp. 925–929, 1998.

[3] Ocean Insight, *Spectrometer Range and Resolution Calculator*, 2021. [Online]. Available: `%5Curl%7Bhttps://www.oceaninsight.com/support/knowledge-hub/spectrometer-range--resolution-calculator%7D`.

[4] Wasatch Photonics, *Wp-ps_wp785-raman-series_19nov20*, WP 785 Raman Spectrometer Series, 2020.

[5] S. L. Jantzen, D. H. Smith, R. H. S. Bannerman, P. L. Mennea, L. J. Boyd, P. G. R. Smith, and C. Holmes, "Superstructure and superimposed fiber Bragg gratings fabricated through small spot direct UV writing," in *2020 Conference on Lasers and Electro-Optics Pacific Rim (CLEO-PR)*, 2020.

Appendices

Appendix A

Modelling of fluence in small-spot direct UV writing

In section 2.3.2 a number of plots of UV fluence for different phase control schemes are shown. The python code used to model these fluence distributions is shown below.

```
import matplotlib.pyplot as plt
import numpy as np
from matplotlib import cm
from matplotlib.colorbar import ColorbarBase
from matplotlib.colors import Normalize

'''
Script to model intensity map (and resulting fluence distribution) of laser
 spot in distance and time under phase control.
'''


def spotProfile(x, *coeff):
    '''
    Intensity profile of UV laser spot (in stationary frame of sample).
    Current profile is Gaussian, but the form of this function can be modified.
    x - Distance across sample in metres
    coeff = [amp, centre, width]
        amp - Peak intensity of laser spot (relative)
        centre - Position of centre of laser spot in metres
        width - width of laser spot in metres
    '''
    amp, centre, width = coeff
    return amp*np.exp(-2*(x-centre)**2/width**2)

def fringes(x, *coeff):
    '''
```

```
28      Intensity fringes inside the writing spot due to the interferometer
29      (relative to the writing spot)
30      x - Distance across sample in metres
31      coeff = [phase, period]
32          phase - phase control signal due to EOM in radians
33          period - period of interferometer in metres
34      '''
35      phase, period = coeff
36      return 0.5*np.sin((x*np.pi*2/period - phase))+0.5
37
38  spotRadius = 2E-6 #Writing spot radius in metres
39  period =1000E-9 #Interferometer period in metres
40
41  distMin = 0E-6 #Minimum distance extent of sample
42  distMax =10E-6 #Maximum distance extent of sample
43  noDist = 2**8 #Number of distance points to sample
44
45  #Array of distance values
46  distArr = np.linspace(distMin-spotRadius, distMax+spotRadius, noDist)
47
48  timeMin = 0 #Minimum time period to model in seconds
49  timeMax = 20 #Maximum time period to model in seconds
50  noTime = 2**11 #Number of time points to sample
51
52  #Array of time values
53  timeArr = np.linspace(timeMin, timeMax, noTime)
54
55  #Writing speed in metre/second
56  speed = (distMax-distMin)/(timeMax-timeMin)
57
58  #Converts 1D distance and time array to 2D data array
59  distMesh, timeMesh = np.meshgrid(distArr, timeArr)
60
61  #Generates a distance/time 2D array of spot movement across sample
62  spotMesh = np.flip(spotProfile(distMesh,*[1,distMin+timeMesh*speed,
63                                            spotRadius]), axis=1)
64
65  #Parameters for 'ideal phase control signal'
66  detuningReset = 1 #Relative period detuning. 1 = no detuning.
67  #Fraction of signal taken up by voltage reset. 0 = perfect reset signal
68  resetFrac = 0
69
70  #2D distance distance/time array of fringes due to movement of spot and
71  # phase signal
72  resetFringesPhase = timeMesh*speed*2*np.pi/period*detuningReset%(np.pi*2)
73  resetFringesPhase[resetFringesPhase>(1-resetFrac)*2*np.pi] = (
74          (1-resetFrac)*2*np.pi +((1-resetFrac)*2*np.pi-
75           resetFringesPhase[resetFringesPhase>(1-resetFrac)*2*np.pi])
76          *(1-resetFrac)/resetFrac)
77
78  #Resulting distance/time 2D array of intensity due to both spot profile
```

```
79 # and fringes
80 intenArr = spotMesh*np.flip(fringes(distMesh,*[timeMesh*speed*2*np.pi/
       period
81                                             - resetFringesPhase, period]),
       axis=1)
82
83 #Parameters for 'non-ideal phase control signal'
84 detuningReset2 = 0.8 #Relative period detuning. 1 = no detuning.
85 #Fraction of signal taken up by voltage reset. 0 = perfect reset signal
86 resetFrac2 = 0.1
87
88 #2D distance distance/time array of fringes due to movement of spot and
89 # phase signal
90 resetFringesPhase2 = timeMesh*speed*2*np.pi/period*detuningReset2%(np.pi
       *2)
91 resetFringesPhase2[resetFringesPhase2>(1-resetFrac2)*2*np.pi] = (
92         (1-resetFrac2)*2*np.pi +((1-resetFrac2)*2*np.pi-
93          resetFringesPhase2[resetFringesPhase2>(1-resetFrac2)*2*np.pi])
94         *(1-resetFrac2)/resetFrac2)
95
96 #Resulting distance/time 2D array of intensity due to both spot profile
97 # and fringes
98 intenArr2 = spotMesh*np.flip(fringes(distMesh,*[timeMesh*speed*2*np.pi/
       period
99                                             - resetFringesPhase2, period]),
       axis=1)
100
101 #Normalises intensity arrays to ideal signal
102 intenArr = intenArr/intenArr.max()
103 intenArr2 = intenArr2/intenArr2.max()
104
105 #Calculates fluence across distance by summing distance/time intensity
       array
106 # over time axis.
107 fluence = np.sum(intenArr, axis=0)
108 fluence2 = np.sum(intenArr2, axis=0)
109
110
111 #Plotting
112 fig = plt.figure('phaseControl (Reset+Detuning)')
113 fig.clear()
114 gs = plt.GridSpec(3,2,left = 0.1, right = 0.8, top=0.95, bottom=0.15,
       hspace=0)
115 ax0 = fig.add_subplot(gs[0:2, 0])
116 ax1 = fig.add_subplot(gs[2, 0])
117 ax2 = fig.add_subplot(gs[0:2, 1])
118 ax3 = fig.add_subplot(gs[2, 1])
119 ax0.text(0.05, 0.95, '(a)',transform=ax0.transAxes, va='top', c='white')
120 ax1.text(0.05, 0.95, '(c)',transform=ax1.transAxes, va='top')
121 ax2.text(0.05, 0.95, '(b)',transform=ax2.transAxes, va='top', c='white')
122 ax3.text(0.05, 0.95, '(d)',transform=ax3.transAxes, va='top')
```

```
123
124 ax0.axes.get_xaxis().set_visible(False)
125 ax2.axis('off')
126 ax3.axes.get_yaxis().set_visible(False)
127 ax0.set_ylabel('Time (s)')
128 ax1.set_ylabel('Total fluence (Rel.)')
129
130 BFCBax3 = plt.axes([0.85, 0.15, 0.05, 0.8])
131
132 cmap = cm.viridis
133 BFnorm3 = Normalize(vmin=intenArr.min(), vmax =intenArr.max())
134 BFcb3 = ColorbarBase(BFCBax3, cmap=cmap, norm=BFnorm3, orientation='
    vertical')
135 BFcb3.set_label('Normalised intensity')
136 ax1.set_ylim([0,1.2])
137 ax3.set_ylim([0,1.2])
138
139 ax0.imshow(intenArr, aspect='auto',extent=[distArr.min()*1E6,
140                             distArr.max()*1E6, timeArr.min(), timeArr.max
    ()])
141 ax2.imshow(intenArr2, aspect='auto', extent=[distArr.min()*1E6,
142                             distArr.max()*1E6, timeArr.min(), timeArr.max
    ()])
143
144 ax1.plot(distArr*1E6, fluence/fluence.max())
145 ax3.plot(distArr*1E6, fluence2/fluence.max())
146
147 plt.subplots_adjust(0,0.05, 1,1)
148 fig.text(0.5, 0.04, 'Distance (micron)', ha='center')
149
150 fig2 = plt.figure('Phase control signal')
151 fig2.clear()
152 phaseAx = fig2.add_subplot()
153 phaseAx.plot(timeArr, resetFringesPhase[:,0],
154              label='Perfect reset signal with no detuning')
155 phaseAx.plot(timeArr, resetFringesPhase2[:,0],
156              label='Imperfect reset signal with no detuning')
157 phaseAx.set_xlabel('Time (s)')
158 phaseAx.set_ylabel('Phase (rad)')
159 phaseAx.legend()
```

Appendix B

C++ library and code for writing devices

The C++ library for use in UV writing is included as a supplementary CD in the printed copy of this thesis. It is also available (on request) from the author. An example of code for writing Bragg gratings with variable blaze angle is included. Previous code for writing fixed angle blazed chirped Bragg gratings in AeroBasic was approximately the same length, and was much more difficult to read and edit.

```
#define _USE_MATH_DEFINES
#include <iostream>
#include <fstream>
#include <cmath>
#include "Stages.hpp" //Headers for UV writing library

using namespace uv;
/*Class definitions for code. Tar, VarBlaze and TarVarBlaze were still in
  development at time of writing so are not part of the library.

  These classes represent custom Period and Angle classes defined by the
    user
*/

//Custom class defining period to focus at a set position without
    aberrations.
class Tar : public Period {
protected:
  double f; //Focal length in mm
  double designWavelength; //Grating deisgn wavelength in nm
  double length; //Grating length in mm
  double blaze; //Fixed blaze angle for grating in radians
  std::string info;
public:
  //Class constructor
  Tar(double designWavelength, double f, double length, double blaze) {
```

```
25      this->designWavelength = designWavelength;
26      this->f = f;
27      this->length = length;
28      this->blaze = blaze; //blaze in radians
29      std::stringstream info;
30      info << "Tar" << designWavelength << "_" << f << "_" << blaze << "_"
31       << length;
32      this->info = info.str();
33    }
34    //Returns the grating period (at a distance z) in mm
35    double getPeriod(double z) {
36      return designWavelength * cos(blaze) / (Config::n*(1 - cos(M_PI / 2 -
37        atan((z - length * 0.5) / -f))));
38    }
39    //Copies the period class
40    Period* clone() {
41      Tar* t = new Tar(this->designWavelength, this->f, this->length,
42       this->blaze);
43      return t;
44    }
45    //Returns a config string containing the parameters for this period
       class
46    std::string getInfo() {
47      return this->info;
48    }
49  };
50
51  //Custom class defining a variable blaze angle matched to ray diffraction
       angle.
52  class VarBlaze : public Angle {
53    double designWavelength; //Grating deisgn wavelength in nm
54    double f; //Focal length in mm
55    double length; //Grating length in mm
56    std::string info;
57  public:
58    //Class constructor
59    VarBlaze(double designWavelength, double f, double length) {
60      this->designWavelength = designWavelength;
61      this->f = f;
62      this->length = length;
63      std::stringstream info;
64      info << "VarBlaze" << designWavelength << "_" << f << "_" << length;
65      this->info = info.str();
66    }
67    //Returns the blaze angle (in radians) as a function of distance along
68    // the grating
69    double getAngle(double z) {
70
71      return M_PI / 4 - 0.5*atan((z - length / 2) / f);
72    }
73    //Copies the angle class
```

```
74   Angle* clone() {
75     VarBlaze* v = new VarBlaze(this->designWavelength,this->f,this->
     length);
76     return v;
77   }
78   //Returns a config string containing the parameters for this angle
       class
79   std::string getInfo() {
80     return this->info;
81   }
82 };
83
84 //Custom class defining a period to focus without aberrations, using a
       blaze
85 // angle matched to ray diffraction angle.
86 class TarVarBlaze : public Period {
87   double designWavelength; //Grating deisgn wavelength in nm
88   double f; //Focal length in mm
89   double length; //Grating length in mm
90   VarBlaze* bla; //Blaze angle class for variable blaze angle
91   Tar* Delta; //Period class for constant blaze angle
92   std::string info;
93 public:
94   //Class constructor
95   TarVarBlaze(double designWavelength, double f, double length) {
96     this->designWavelength = designWavelength;
97     this->f = f;
98     this->length = length;
99     std::stringstream info;
100    info << "TarVarBlaze" << designWavelength << "_" << f << "_" <<
     length;
101    this->info = info.str();
102    Delta = new Tar(designWavelength, f, length, 0);
103  }
104  //Class destructor
105  ~TarVarBlaze() {
106    delete Delta;
107  }
108  //Returns the grating period (at a distance z) in mm
109  double getPeriod(double z) {
110    double delta = Delta->getPeriod(z);
111    double blaze = M_PI / 4 - 0.5*atan((z - length / 2) / f);
112    return delta * cos(blaze);
113  }
114  //Copies the period class
115  Period* clone() {
116    TarVarBlaze* t = new TarVarBlaze(designWavelength, f, length);
117    return t;
118  }
119  //Returns a config string containing the parameters for this period
       class
```

```
120   std::string getInfo() {
121     return this->info;
122   }
123 };
124
125 int main() {
126   //Loads config file
127   ConfigLoader::configFilePath =
128     "C:/users/smithgrp/Documents/uv-writing-library/config.json";
129   //Initialises library using config file and setup parameters
130   ConfigLoader::init(LABNAME_2042, BOARDNAME_1064Planar, true);
131
132   //Sets distance limits for edges of writing stage
133   Config::xMax = 42.6;
134   Config::xMin = -254;
135   Config::yMin = -185;
136   Config::yMax = 72;
137
138   Config::n = 1.46; //Sample refractive index
139   double fluence = 14; //Writing fluence (approximate due to blaze angle)
140
141   double pitch = 0.25; //Distance between waveguides
142   double gratingLengthShort = 1; //Short grating length in mm
143   double gratingLengthLong = 2; //Long grating length in mm
144   //Distance between waveguide facet and start of grating
145   double startBuffer = 6;
146
147   double designWavelength = 780; //Design wavelength in nm
148   double blazeAngle = M_PI / 4; //Blaze angle in radians
149   double duty = 0.9; //Maximum duty cycle
150
151   //Defines pointer to stage class
152   Stages* s = Stages::getInstance();
153
154   //Prompts user to measure laser power
155   s->powerMeasure();
156
157   /* Grating 1
        ================================================================
158   Height 4mm
159   Length 1mm
160   Start = 3mm
161   wgLength = 4.1mm
162   Aberration corrected 4mm focal length
163   Constant blaze angle
164   Uniform Apodisation
165   Design wavelength = 780nm
166   */
167   std::vector<Waveguide> wgs;
168   Waveguide wg1;
169
```

```
170  //Writes a small distance to make sure waveguide passes through facet
171  wg1.addPath(&overshoot, fluence);
172  //Defines period class for grating
173  Tar per1(designWavelength, 4, gratingLengthShort,
174    blazeAngle);
175  UniformApodisation uni(duty); //Defines apodisation for grating
176  ConstantAngle constAng(blazeAngle); //Defines blaze angle for grating
177  ConstantPhase pha; //Defines phase across grating (constant)
178
179  //Defines a grating class using period, apodisation, angle and phase
       classes
180  GratingFromFunctions grat1(&per1, &uni, &pha, &constAng,
181   gratingLengthShort);
182
183  //Sets position of start of grating in waveguide
184  grat1.setBuffer(startBuffer, Config::overshoot);
185  //Ensures waveguide is long enough to contain whole waveguide
186  wg1.addPath(&Line(startBuffer + gratingLengthShort + Config::overshoot)
       ,
187    fluence);
188  //Adds grating into waveguide class
189  wg1.addGrating(&grat1);
190  //Records firing positions to file
191  wg1.firingPosFile("Waveguide1.txt");
192
193  //Applies rotation correction to grating.
194  wg1.rotationCorrect();
195  //Adds built waveguide to vector of waveguides to be written
196  wgs.push_back(wg1);
197
198
199  /* Grating 3
       ================================================================
200  Height 4.25mm
201  Length 2mm
202  Start = 6.2mm
203  wgLength = 8.3mm
204  Aberration corrected 4.25mm focal length with variable blaze angle
205  Variable blaze angle for specular reflection
206  Uniform Apodisation
207  Design wavelength = 780nm
208  */
209  overshoot.translate(glm::dvec3(0, pitch, 0));
210  Waveguide wg3;
211  //Writes a small distance to make sure waveguide passes through facet
212  wg3.addPath(&overshoot, fluence);
213  VarBlaze blaze(designWavelength, 4.25,
214    gratingLengthLong); //Defines blaze angle for grating
215
216  TarVarBlaze per3(designWavelength, 4.25,
217    gratingLengthLong); //Defines period class for grating
```

```
218
219  //Defines a grating class using period, apodisation, angle and phase
       classes
220  GratingFromFunctions grat3(&per3, &uni, &pha, &blaze, gratingLengthLong
       );
221  //Sets position of start of grating in waveguide
222  grat3.setBuffer(startBuffer + gratingLengthShort + Config::overshoot);
223  //Ensures waveguide is long enough to contain whole waveguide
224  wg3.addPath(&Line(startBuffer + gratingLengthShort + gratingLengthLong
225   + Config::overshoot,   fluence);
226  //Adds grating into waveguide class
227  wg3.addGrating(&grat3);
228  //Records firing positions to file
229  wg3.firingPosFile("Waveguide2.txt");
230  std::vector<double> wg3Angles = wg3.getAngles();
231
232  //Applies rotation correction to grating.
233  wg3.rotationCorrect();
234  //Adds built waveguide to vector of waveguides to be written
235  wgs.push_back(wg3);
236
237  //Records rotation corrected coordinates (with variable blaze angle) to
       file
238  wg3.coordFile("wg3Coords.txt");
239  std::ofstream fout("wg3Angles.txt");
240
241  Grating newGrat(grat3);
242  double ang1 = newGrat.angle(0.1);
243  double ang2 = newGrat.angle(0.5);
244  if (!fout) {
245    std::cout << "Cannot open 'wg3Angles.txt'" << std::endl;
246  }
247  else {
248    for (int i = 1; i < wg3Angles.size() ; ++i) {
249      fout << i << " " << wg3Angles.at(i) << std::endl;
250    }
251    fout.close();
252  }
253
254  //Writes waveguides
255  try {
256    s->write(&wg1);
257    s->write(&wg3);
258  }
259  //Error handling
260  catch (std::exception &e) {
261    log(LEVEL_Error, e.what());
262    std::cout << "ERROR: " << e.what();
263    s->close();
264    exit(-1);
265
```

```
266     }
267 }
```

Appendix C

Publications

[1] J. W. Field, S. A. Berry, R. H. S. Bannerman, D. H. Smith, C. B. E. Gawith, P. G. R. Smith, and J. C. Gates, "Highly-chirped Bragg gratings for integrated silica spectrometers," *Optics Express*, vol. 28, no. 14, pp. 21 247–21 259, 2020.

[2] J. W. Field, S. A. Berry, R. H. S. Bannerman, C. B. E. Gawith, P. G. R. Smith, and J. C. Gates, "Optimizing resolution in an integrated blazed chirped Bragg grating spectrometer," in *Integrated Optics: Devices, Materials, and Technologies XXIV*, vol. 11283, 2020, pp. 145–150.

[3] J. W. Field, S. A. Berry, R. H. S. Bannerman, D. H. Smith, J. C. Gates, C. B. E. Gawith, and P. G. R. Smith, "Miniaturised, planar, integrated Bragg grating spectrometer," in *2019 Conference on Lasers and Electro-Optics Europe European Quantum Electronics Conference (CLEO/Europe-EQEC)*, 2019.

[4] J. W. Field, S. A. Berry, D. H. S. Smith, J. C. Gates, and P. G. R. Smith, "Improving the functionality of a laser writing system using software," in *Third Conference of Research Software Engineers*, 2018.

[5] J. W. Field, M. T. Posner, S. A. Berry, R. H. S. Bannerman, J. C. Gates, and P. G. Smith, "Fabricating a prototype spectrometer using a large-angle direct UV-written chirped tilted grating," in *Advanced Photonics 2018 (BGPP, IPR, NP, NOMA, Sensors, Networks, SPPCom, SOF)*, Optical Society of America, 2018, BW2A.4.

[6] S. Scholl, A. Jantzen, R. Bannerman, J. Field, J. Gates, L. Boyd, P. Smith, and C. Holmes, "Classification of small-spot direct UV written fiber Bragg gratings through extreme thermal treatment," in *Advanced Photonics 2018 (BGPP, IPR, NP, NOMA, Sensors, Networks, SPPCom, SOF)*, 2018, BM3A.7.

[7] L. G. Carpenter, S. A. Berry, R. H. Bannerman, A. C. Gray, J. W. Field, C. Holmes, J. C. Gates, P. G. Smith, and C. B. Gawith, "Developing PPLN waveguides for quantum rubidium atom traps in space," in *Advanced Photonics 2018 (BGPP, IPR, NP, NOMA, Sensors, Networks, SPPCom, SOF)*, 2018, NpTh1C.6.

[8] S. Berry, L. G. Carpenter, J. Field, J. Gates, and G. C., "Domain engineering in PPLN waveguides for tailored QPM spectral response," in *SPIE Photonics West 2018*, 2018.

[9] S. Berry, L. G. Carpenter, J. Field, J. Gates, P. Smith, and G. C., "Design and manufacture of single mode PPLN diced waveguides for quantum applications," in *SPIE Photonics West 2018*, 2018.

[10] L. G. Carpenter, S. Berry, J. W. Field, and C. B. Gawith, "Zinc indiffused PPLN ridge waveguides," in *SPIE Photonics West 2018*, 2018.